UNIVERSIDAD ADOLFO IBÁÑEZ

MASTER THESIS

Characterization of 3D-Bioplotting of polycaprolactone-bioactive glass composite scaffolds for Tissue Engineering Applications

---

Author:

José Ignacio Contreras Raggio

Guide Professors:

Dr. Juan F. Vivanco Morales

Dr. Ameet Aiyangar

Thesis carried out according to the requirements for the Master´s degree in Engineering Sciences, mention Bioengineering of the

Faculty of Engineering and Sciences

14/03/2022

UAI | FACULTAD DE INGENIERÍA Y CIENCIAS

UNIVERSIDAD ADOLFO IBÁÑEZ

Abstract

Faculty of Engineering and Sciences

Master in Engineering Sciences, mention Bioengineering

Characterization of 3D-Bioplotting of polycaprolactone-bioactive glass composite scaffolds for Tissue Engineering Applications

by José Ignacio Contreras Raggio

Tissue engineering is an emerging field which combines engineering and life science in order to develop biological substitutes to regenerate, restore and repair defective tissues. One approach is the generation of three-dimensional matrices or scaffolds to create a temporary matrix with a similar host environment for cells to eventually proliferate to eventually form an organized tissue system. Additive Manufacturing (AM) processes provides a tool to manufacture these scaffolds in a patient-specific way. Scaffolds requirements are strict and are widely studies for a better performance. Extrusion based AM processes such as 3D-Bioplotting offers flexibility in terms of the input material as the scaffolds are constructed by an ink ejected with pneumatical pressure following an input STL file.

This Thesis investigate the relation between the 3D-Bioplotting, fabrication parameters and scaffolds characterization in order to improve and understand the behavior of these geometries. First, the scaffold fabrication is detailed. Scaffolds of Bioglass and Polycaprolactone were printed in different geometries. Wells, cylinders and cubes with controlled pore size and porosity were used for the different experiments. A prior parameters screening and selection showed the best printing parameters for the different combination of materials. A preliminary study suggests the need for an external system in order to improve the quality of the samples. The lack of control over temperature of the 3D-Bioplotter was restore with the introduction of a new fan setup. Scaffolds fabrication was improved with a custom-made python script which analyze the captures

images of the bioplotter while printing to allow for small tune of the parameters while printing. The code allows to measure strut diameter and drastically improves the final scaffolds resolution.

Furthermore, the code was use for scaffold characterization, providing a new tool to measure the inner structure. Samples had a homogeneous inner structure measure with the code and verify with a micro-CT. Porosity measurement was also check and a trend was found with the captured images. Mechanical characterization showed different results with the literature, were the addition of BG decrease the mechanical properties of the sample. Biological behavior showed a similar trend with positive results at first week but negative at the second one.

Rheological characterization of the inks allows a better understanding of them and generate additional information for the printing process. A combination of formulas describes the shear at the tip of the bioplotter nozzle. The behavior of the material at these shears were analyzed reporting viscosity, storage, and loss modulus. Furthermore, this information also suggests the need of an additional cooling system in order to keep the shape of the printed struts, the fan set up. Additionally, the rheological characterization was annexed with the printing speed with a series of formulas, finding a relation between the viscosity and the needed printing speed of the machine. This relation was correlate with experimental data and a small deviation was found, allowing to effectively predict the feasibility of printing for new materials and reducing the set-up time and costs.

The thesis gives a guide for scaffold fabrication and a new tool for inner characterization.

Keywords: PCL, Bioglass, Composite bio-scaffolds, Direct ink writing, Additive manufacturing, Composite ink characterization

DEDICATION

To my family and Aline, who have always been my source of encouragement, support, and strength.

BIOGRAPHY

José Ignacio Contreras Raggio completed his Bachelor´s degree in Engineering Science and his Professional's degree in Bioengineering from Universidad Adolfo Ibáñez, Santiago, Chile in December 2020, and July 2021 respectively. He started working with Professor Dr. Juan Francisco Vivanco Morales in Tissue Engineering at his third year of university. From 2017 until 2019 he develops and mastered the ability of 3D printing. On 2019 he was invited to realize his 10-months internship at the Swiss Federal Laboratories for Material Science and Engineering (EMPA) under the supervision of Professor Dr. Ameet Aiyangar. In 2020 José Ignacio joined the Master´s curriculum Bioengineering of his university. He began working of his master´s thesis on a second internship at EMPA in 2021.

ACKNOWLEDMENTS

I would like to thank my co-advisors Dr. Juan F. Vivanco Morales and Dr. Ameet Aiyangar for their continuous support and guidance. Learning and working with them over the past five and three years, respectively, has been inspiring and rewarding.

I would like to thank Dr. Gilberto Siqueira for his guidance and assistance in 3D printing. I would also like to thank Dr. Raul Vallejos for his willingness and performing the biological characterization.

I would like to thank to my colleague Miguel Pardo for his insightful comments and assist in the rheology characterization. I would also like to thank Iurii Burda, Bernhard Weisser, Pablo Nuñez and Thomas Vielma for their help.

TABLE OF CONTENTS

LIST OF TABLES

LIST OF FIGURES

LIST OF ACRONMYS

Acronym	Nomenclature
3D	Three dimensional
AM	Additive manufacturing
ANOVA	Analysis of variance
ASTM	American Society of Testing and Materials
CAD	Computer aided drawing
CI	Confidence interval
ECM	Extracellular matrix
FDA	Food and drug administration
FDM	Fused deposition modeling
FEA	Finite element analysis
HA	Hydroxyapatite
ID	Inner diameter
microCT	Micro-Computed Tomography
MSC	Mesenchymal stem cells
OD	Outer diameter
PCL	Polycaprolactone
PGA	Poly-glycolic acid
PLA	Poly-lactic acid
PLLA	Poly-L-lactic acid
RPM	Rotations per minute
SD	Standard deviation
SEM	Scanning electron microscope
SFF	Solid freeform fabrication

SLA	Stereolithography
SLS	Selective laser sintering
STL	Stereolithographic file
TE	Tissue engineering
UV	Ultraviolet

CHAPTER 1: INTRODUCTION

This chapter gives a brief background of tissue engineering with an introduction to scaffold-based tissue engineering. It includes the problem or opportunity, which be the motivation along the thesis.

1.1 Background

Tissue Engineering (TE) is a rapidly evolving discipline requiring collaborative efforts in life sciences and engineering [1]. An interdisciplinary field that has the potential to revolutionize treatment of various diseases and disorders by creating biological substitutes to restore, repair, maintain and improve tissue/organ function [2]. The formal definition proposed during the first TE symposium in 1998 is as follows [3].

"The application of the principles and methods of engineering and life sciences toward the fundamental understanding of structure-function relationships in normal and pathological mammalian tissue and the development of biological substitutes to restore, maintain, or improve tissue function"

The need of such hybrid and innovative approach can be attributed to a series of factors, such as the annual organ shortage which expenses go up to $400 US billion [2]. Moreover, the increasing trend in the waiting list for organ transplant patients generate a considerable discrepancy with the number of donors (**Error! Reference source not found.**) [4].

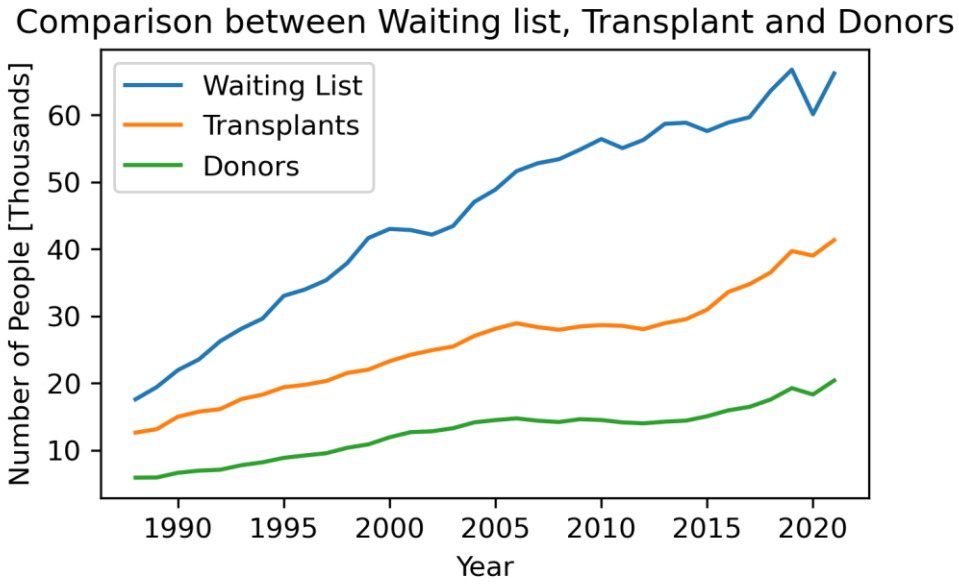

Figure 1-1 Comparison between waiting list, transplant, and donors over the years [4].

On the other hand, not all organs are effectively transplanted as some can be rejected by the host immune system and run the risk of infection [5]. Same complications face *in vivo* medical device when are used for treating such patients [6].

Products in TE suggest an alternate approach to fulfill with these requirements. Additionally, can also serve as a model to understand cell/tissue structure, cell signaling and may even replace animal models in few cases [7].

Currently, with advances in technology, the two-dimensional cell culture is being translated to more representative three-dimensional (3D) configuration by the TE constructs, culture media and bioreactors [8], [9]. A 3D configuration mimics the physiological context for the cells to organize into a regulated functional unit [10]. This configuration uses a porous biomaterial that promote tissue formation *in vitro*, in a controlled environment, then this is implanted at the desire site and expected to resume the normal tissue regeneration in a *in vivo* environment to restore function.

Even though TE offers a promising solution, there are significant challenges that are to be addressed [11]. Fabricating such scaffold of finite size (larger than a few millimeters) and complex architectures required a novel understanding of the used technology. Overall, being TE a complex interdisciplinary field, a better understanding of all areas of research is needed to produce a significant progress.

1.2 Scaffolds in Tissue Engineering

A scaffold is a structure that gives support and act as a matrix which facilitate the migration, binding and transport of cell or bioactive molecules used to replace, regenerate or repair tissues [12]. Scaffolds are designed to mimics the extra cellular matrix of the engineer tissue [13]. The structure is designed to give enough support for the tissue until the regeneration is complete, providing mechanical stability and an adequate biological environment.

The TE approach uses the scaffold as a drive vehicle for improving regeneration. The process presents a series of steps to effectively achieve the desire task. First, a sample of cells is acquired from the donor site of interested, these are expanded to later being seed into the desire scaffold. The scaffold is later introduced in the damage site for regeneration. The use of native cells helps

to decrease the level of rejection of the scaffold. Therefore, another approach is to use stem cells or xenogeneic cells (donor from different species), depending upon the application [14].

Currently studies have shown how 3D cell cultures resemble closer than 2D cultures to cellular morphology of native tissue [8]. To have an ideal cell adhesion, migration and signal the build scaffold needs to present an appropriate geometry, architecture, and surface features [10].

Scaffold can be fabricated with different types of biomaterials [15] using different processes. Among these processes two mayor lines are presented, conventional techniques such as fiber bonding, solvent casting and electrospinning, and additive manufacturing (AM) processes [16] such as fused filament fabrication (FFF), selective laser sintering (SLS) stereolithography (SLA), and 3D-Bioplotting. This last technique offers a more control environment as the design is defined by a computer model and the structure is then fabricate in layers.

Although the AM processes generally offer greater control and flexibility compared to conventional techniques, there are a few challenges. For example, generate relevant size structures for clinical application can be restricted by the high processing cost, time, and equipment, additionally, different disciplines must work collaboratively [17]. This limitation can be overpass by generating methodologies to optimize the process and thus reducing both time and cost [17].

1.3 Problem or Opportunity

The development of AM process such as 3D printing can, theoretically, allow precise control during the manufacturing process to fabricate scaffolds with high geometric fidelity [10]–[12], [14]. Scaffolds with reproducible architectures have been shown to be printable [9], however, to effectively scale up without jeopardize the reliability of the printed structures, a better understanding of the interactions between the material properties and the processing parameters is required. Some of the important flaws of these processes include:

- Dependency of the process to the viscosity of the material al the nozzle tip [8]
- Low mechanical strength of the fabricated structures [3], [9]
- High cost to calibrate a new material [3], [9]

These inherent disadvantages limit the material selection by the mechanical requirements and rheology properties. Calibration of the process parameter lack of an adequate, and fast,

methodology that reduce the times and cost to evaluate the viability of a new material. Thus, to have a more control process, a better understanding of the parameters is needed and a system to predict them in a cheaper and faster way.

One such promising 3D printing technique is Direct Ink Writing (DIW) or 3D-Bioplotting which is an extrusion base AM process that is compatible with the use of polymers, hydrogels, and cell suspension as raw materials. DIW involves extrusion of viscoelastic inks through a nozzle by a displacement-controlled driving mechanism in conjunction with pressure, speed, and temperature control.

Additionally, currently characterization methodologies lack of an objective in-situ evaluation. The printing processes is mostly a blind procedure where the dispensing head position avoid the view of the printing layer and most of the printed object. Therefore, is not possible to effectively evaluate the quality of the printing process while printing without pausing the procedure. The 3D Bioplotter offers an attach camera which, when the printing stops, capture a superior picture of the printed layer. This automatic procedure allows to have a fast update on the printing status. The qualitative information of the upper layers gives enough information to take radical actions such as stop the printing process due to big malformation known as printing errors, however, minor changes cannot be done in base of this information, the lack of a numerical report allows just mayor changes. A numerical characterization is needed that give enough information for small changes during printing, reducing the printing errors and thus the time and printing cost.

Furthermore, scaffolds characterization is usually done by destructive methods, inner structure cannot be access without cutting the sample or apply high doses of X-rays that affect the material properties. A less invasive methodology would allow to run several tests on a sample, reducing the number of samples needed and to improve the understanding of its behavior in a more complex way.

1.4 Chapter Summary

TE is an emerging field combining principles of engineering and life science which creates biological substitutes aiming to revolutionize treatments of various disease and disorders. One of the approached in this discipline is to create porous and biodegradable structures called 3D matrices or scaffolds for creating these substitutes. These will act as temporary housing for cells and will provide de ideal environment for proliferation and differentiation. The fabrication of these

scaffolds is critical for the success of this approach, having specific and strict requirements. The current limitation for 3D-Bioplotting includes the depend on the process to the viscosity of the material, the low mechanical strength of the fabricated structures and the high cost to calibrate a new material. These problems are inherent to the process and new methodologies needs to be defined to fulfill the present challenge.

CHAPTER 2: LITERATURE REVIEW

In this chapter, TE scaffold literature is review concerning to scaffold design and fabrication process. Extrusion-based AM fabrication process and the importance of material rheology is presented in greater detail due to their relevance to this thesis.

2.1 Requirements for Scaffolds

The Extracellular matrix is where most cells in human tissues resides in a fibrous, interconnected network of functional proteins and polysaccharides. The secreted macromolecules that constitute the ECM, being oriented and modifies by the cellular components of tissues, exert control over many cellular processes such as growth and wound healing [18]. The ECM provides a series of benefits for its environments like, structural support and the physical setting for cells to reside in, mechanical properties like rigidity and elasticity, bioactive cues for regulating cell activities, acts as a reservoir of growth factors and provides dynamic degradable environment to allow tissue healing and remodeling [13], [19].

The fundamental role of TE scaffolds is to simulate and mimic the ECM of cells temporarily, promoting tissue regeneration. Since the interaction between the ECM and cells is a dynamic process and is continually changing it generate an extremely challenge to mimic this environment [8].

2.2 Scaffold Material

The scaffold material plays a critical role in tissue regeneration since it in direct contact with the cells while acting as a substrate. Material selection for TE scaffolds is bases on a few important criteria, such as [20]:

- Biocompatibility: the scaffold should be able to be implanted without triggering a negative response from the host having a suitable surface chemistry for cell attachment, proliferation, and differentiation.

- Biodegradability: the material will provide support for the tissue to grow being biodegradable or bioresorbable with a controllable degradation and resorption rate to match the cell/tissue growth *in vitro* and/or *in vivo*.

- Mechanical properties: tunable mechanical properties to match those of the tissue at the site of implantation providing temporary mechanical support to withstand *in vivo* stresses and loading.

- Processibility: be easily processed to form a variety of shape and size, and so in a way that can be reproducible, economically viable and transform to a large scale.

2.2.1 Classifications

Four types of biomaterials have been experimentally and/or clinically studied as scaffold materials for TE applications [20]:

1. Synthetic organic materials (e.g., Aliphatic polyesters)
2. Synthetic inorganic materials (e.g., HA)
3. Organic materials of natural origin (e.g., collagen)
4. Inorganic material of natural origin (e.g., coralline HA)

Naturally derived materials that do not invoke a foreign body response when introduced *in vivo* such as fibrin, collagen, GAGs, alginates, starch, and chitosan can be directly extracted from plans, animal, or human tissues. These natural polymers have been used in conjunction with synthetic polymers such as PLLA, PGA and PCL to impart superior mechanical properties and also improve cell interactions [21]. Collagen with electrospun nanofibers have been used as scaffolds for bone and cartilage [21]. Collagen-GAG scaffolds that have been used clinically for skin regeneration and have shown potential in engineering different systems with the use of mesenchymal stem cells (MSCs) [22].

Bioceramics which include HA, bioglass, tri-calcium phosphate (TCP) closely mimic bone tissues and have therefore been used widely in bone TE. These materials provide an osteoconductive environment where bone ECM proteins are absorbed, resulting in osteoblasts adhering and proliferating [23]. Ceramics have great mechanical properties but has mostly been used in conjunction with polymers as composite scaffolds to compensate for their brittle properties.

Polymers are generally chosen over other materials because of their ease of processing and tailorable properties [15]. They also give predictable results compared to naturally derived materials [10].

The material used in this research is polycaprolactone (PCL), a US Food & Drug Administration-approved semi-crystalline polymer, which is biodegradable and has a melting temperature ranging between 59 - 64°C [24], [25]. This aliphatic polyester is composed of hexanoate repeating units [26] and has been shown to be suitable for scaffold fabrication, as well as for a wide variety of clinical applications [27], [28]. Currently, the biopolymer is being extensively investigated as a biomaterial and shows an increasing trend in TE applications (Figure 2-1) [29]. Another advantage of PCL is that it can be easily combined into blends with other materials and manipulated to fabricate scaffolds of desire specifications [21], possess stable rheological properties, low glass-transition temperature and high decomposition temperature [8], and can be processes using a multitude of techniques.

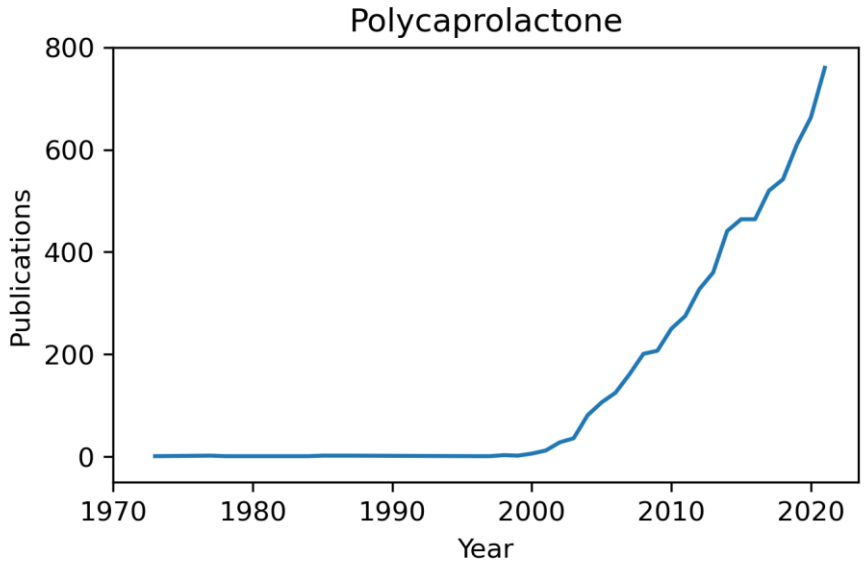

Figure 2-1 Publications using PCL in the field of TE from 1970 to 2020

Among the limitations of PCL, its hydrophobic nature and slow degradation rate makes it difficult for blood and biological fluids to penetrate it, and to match the rates of bone formation [28]. However, the addition of bioactive glasses and other degradable materials can help to overcome these limitations [30]. Bioactive glasses (BG) are biocompatible and biodegradable materials able to bond with natural bone instead of forming a fibrous capsule [31]. Additionally, bioglasses such as 45S5® (46.1 mol% SiO_2, 24.4 mol% Na_2O, 26.9 mol% CaO, and 2.6 mol% P_2O_5) possess osteogenic properties to promote bone formation when inserted into bone defects [31]. The combination of BG like 45S5® with PCL have been used to fabricate bone scaffolds with improved osteogenic properties [32].

2.3 Scaffold Architecture

Scaffold architecture is critical to cell proliferation since mass transport mechanism in TE scaffolds is primarily through diffusion [33]. Nutrient supply to cells *in vivo* is through 18 capillaries, which are usually situated within 100 µm from any given cell [34]. Static cell cultures in 3D scaffolds for TE have shown tissue formation only 100 to 200µm into the peripheral regions of the scaffolds due to diffusion limitations [33]. The diffusion of nutrients and waste in and out of cells is mainly influenced by scaffold architecture (pore size and porosity), material degradation characteristics and surface topography, which is covered in this section.

2.3.1 Pore size and porosity

The size of pores in 3D scaffolds is one of the main parameters that define the cell seeding, in-growth of tissue and cell attachment. Have been shown that a series of responses as angiogenesis, inflammation, foreign body capsule formation and tissue infiltration are dependent *in vivo* on average pore size and the pore size distribution [35], [36]. The ideal pore size for scaffolds takes into consideration the different cell type and its size, having distinct pore size requirements [15], [37].

Table 2-1 Pore size requirements of different cell types [9], [10], [38] **(recovered from** [19]**)**

Cell type		**Pore size**
Bone	Minimum size based on cell dimension	>100 µm
	To promote new bone formation	>300 µm
Fibroblast and endothelial cells		50 to 90 µm
Hepatocytes		20 µm
Vascular smooth muscle cells		63- 150 µm
Keratinocytes and Skin cells		20- 125 µm

On the other hand, scaffolds can be characterized and evaluated in terms of their overall porosity. Scaffold porosity is the space available for cells to migrate and proliferate, defined as the relation between the empty and solid space of a scaffold [10]. The porosity regulated the mass transport of oxygen, nutrients, and waste material. Micro-porosity defines how is going to be the interface,

defining the capillary ingrowth and cell attachment [10]. Ideally the designed scaffold should have a high porosity, high surface area to volume ratio and an interconnected geometry for the different shapes [34], nevertheless, a high porosity would mean a diminish in mechanical properties of the scaffold.

Porosity of a geometry can be measure with several different approach, this value is general expresses as a percentage. Usually in literature the relation between the dry weight and the overall volume is used to determinate the porosity following ASTM F2450-10. The estimate porosity is represented by Equation **2-1**.

$$\boldsymbol{V_P = V_T - (m_S/\rho)} \qquad \text{Equation 2-1}$$

where V_P is volume of the pores, V_T is the total volume of the scaffold, m_S is the mass of the scaffold measured using a weighing scale, and ρ is the density of the scaffold material. V_T is calculated by the overall dimensions of the scaffolds. Porosity is expresses as a percentage of volume of the pores with respect to the total volume of the geometry using Equation 2-2.

$$\boldsymbol{Porosity}\ [\%] = (\boldsymbol{V_P/V_T}) * \boldsymbol{100} \qquad \text{Equation 2-2}$$

These equations are used for general structures. Landers et al [39] developed a theoretical approach for calculating the porosity of regular structures generated by using AM processes. This is valid for structures with alternate layers arranged orthogonally.

$$\boldsymbol{Porosity}\ [\%] = \boldsymbol{1 - \left(\frac{\pi d_1^2}{4 d_2 d_3}\right) * 100} \qquad \text{Equation 2-3}$$

where d_1 is filament diameter, d_2 is the repeat length and d_3 is the layer thickness. However, this formula is valid for non-continuous strand and assumes a regular strut diameter.

Additionally, these values correspond to the fabrication parameters, once the structure is deposited *in vivo* a degradation will take place which will increase the pore size resulting in changes of the structure and the interconnectivity with time [38]. The TE of the scaffold should consider the rate of degradation for a better performance.

2.3.2 Overall dimensions

Scaffolds fidelity should also be measure by their overall dimensions, 3D geometries do not always full fill the desire geometry and thus, they present dimension errors. Scaffolds overall dimensions represent one of the fastest quality controls. An example of overall dimension for cylindrical scaffolds correspond to the diameter and heigh of the printed samples, which can be measure with cheap and easy tools like a caliper [40].

2.3.3 Rate of degradation

Scaffolds should be fabricated with biocompatible materials that do not elicit an immunological response and/or exhibit any cytotoxic behavior from the host system [41]. The rate of resorption or degradation should be designed such that the structure give support until the surrounded tissue is able to retain the *in vivo* loads and take over the role of the scaffold [8].

Two general strategies have been outlined for material selection based on degradation rate [20]. In the first strategy, the designed scaffold will bear the whole *in vivo* loads until the tissue is recovered and/or remodeled and ready to behave as a normal tissue. On the second approach, the scaffold is first treated *in vitro* to increase the mechanical properties prior an implantation. Once the composite reaches the desire properties is implanted into the host. These strategies are illustrated in with respect to a heart valve transplant [20].

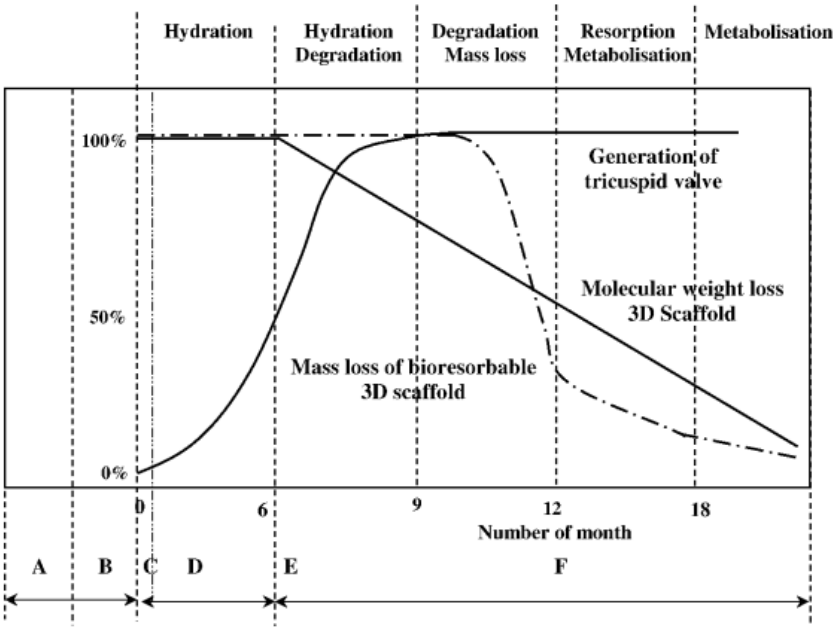

A - Fabrication of bioresorbable 3D scaffold.

B - Harvest cells from patient.

C - Cell seeding into a 3D scaffold in a static culture (petri dish).

D – Growth of mature tissue in a physiologic environment (bioreactor).

E - Surgical transplantation.

F - Implant adaptation and assimilation.

Figure 2-2: Graphical illustration of the complex interdependence of molecular weight loss and mass loss of the 3D scaffold matrix and time frame for cell/tissue generation recovery from [20]**.**

The graphs show the complex interaction for a 3D scaffold between the mass loss with respect to the time taken for tissue regeneration and remodeling. Moreover, the degradation rate is also a consequence of the geometry of the scaffold, the processing technique used, and the material properties.

2.3.4 Surface topography

Scaffolds fabricated with different techniques and materials present different surface topography. Irregular surfaces as with nodes, pores and pattern have been shown to exhibit pronounced cellular activities, morphological changes and have been associated with the production of regulatory

factors [34]. In general, surface roughness increases cell adhesion, migration, and extracellular matrix production.

Among the limitations of PCL, its hydrophobic nature reduces the cell adhesion and make it difficult for blood and biological fluids to penetrate it [42]. However, the addition of bioactive glasses and other biodegradable materials can help to overcome these limitations [43].

2.4 Mechanical Properties

The mechanical properties of tissue engineering scaffolds should be designed to resemble the native or host tissue. Most of the nature tissues present anisotropic and non-linear material properties which poses a challenging problem to replicate using artificial scaffolds [9]. For this, a series of study have determinate the mechanical properties of different organ/tissue systems [44]. Table 2-2 shows examples of the mechanical properties for different tissues [3].

Table 2-2 Mechanical properties of different tissues [3]

Material	Elastic Modulus (MPa)	Yield Stress (MPa)	Strain (%)
Collagen Fibers	500	50	10
Elastin	100	300	300
Cartilage	10	20	70 - 200
Skin	35	15	100
Muscle Fascia	350	15	270
Tendon	700	60	10
Trabecular Bone	10-1058	1.5-9.3	1.09-1.24
Cortical Bone	5620-19830	50.5-191.3	0.36-0.91

Tailored scaffolds should have sufficient mechanical strength to bare the *in vivo* loads without losing its shape to promote cellular ingrowth. Tissue engineering scaffolds used in bone regeneration require the ability to withstand these loas until the desire bone tissue is restores and take over the stresses [45]. The mechanical properties of the scaffold are determinate by the inherent material properties and its distribution along the scaffold geometry, for instance, more porous structures present lower bearing capacity and crystalline polymers show increases tensile strength [15], [33].

The selection of the scaffold material should be based on the desire mechanical properties for the tissue being engineered. The scaffold should closely match the host tissue, varying with age and gender among others [46]. A clear example is the different between different bone density of different individuals Figure 2-3 [46]. Moreover, the scaffold material will define the degradation rate which needs to be tailored to retain the mechanical properties until the host tissue is repaired or remodeled and have enough strength to bare the *in vivo* loads. This is also affected by the mass and architecture of the scaffold.

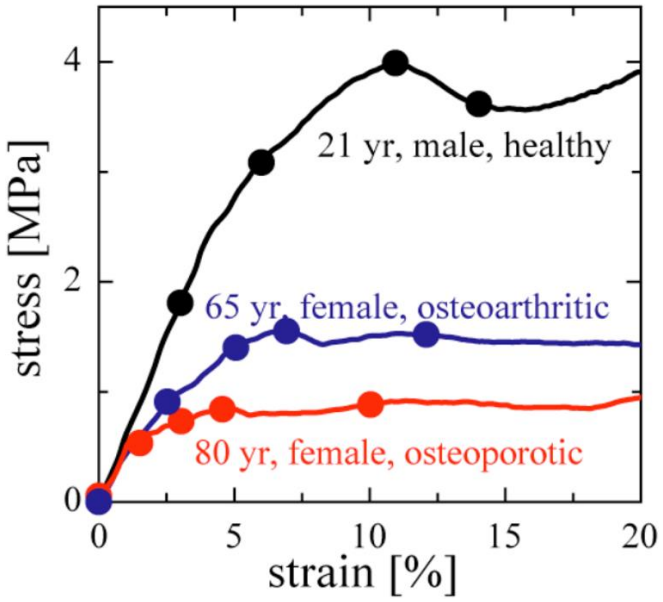

Figure 2-3 Variation in bone strength between gender and age [46]

Meeting these mechanical requirements with traditional, single class materials is infeasible, so modern scaffold design involve composites materials to optimize their varied properties stiffness, toughness and biocompatibility [5].

2.5 Scaffold Fabrication Techniques

The biomaterial and the fabrication technique chosen to build the scaffold are key parameters in controlling their performance [42], [47]. To effectively address the broad spectrum of design parameters described on the previous sections, an ideal scaffold fabrication technique should provide enough control of the process to the user to effectively tailor the desire scaffold.

The fabrication of scaffold can be broadly classified into two mayor categories, these are defined by the level of control that the user will have in the process. A low control process is defined as non-deterministic technique, on the other hand, a high controlled process will be classified as a stochastic technique.

2.5.1 Nondeterministic Techniques

1) Solvent casting and particle leaching

Solvent casting corresponds to the oldest technique used to generate porous structures. It used a solvent to cast a polymer into a desire shape with embedded water-soluble particles. The particle dimensions are chosen based on the desire pore size, the relation between the particles and the polymer will define the porosity. These particles are eventually removed by adding the solvent and thus leaving a porous structure. This technique is generally used to generate high porosities mostly used in scaffolds for engineering soft tissues [48]. However, one of the limitations is the low or null ability to control the distribution of the pores and thus having a random structure that might have non-interconnected pores and low mechanical properties.

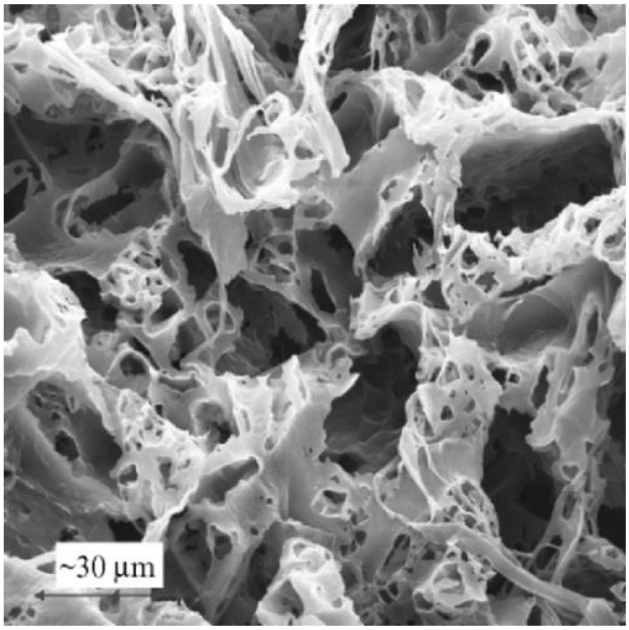

Figure 2-4 A highly porous, interconnected structure of a particulate leached PCL tissue Scaffold [49]

2) Electrospinning

Electrospinning (Figure 2-5) employs the principle of electrostatic repulsion to eject a polymer stream to produce continuous fibers [19]. This stream is directed towards a grounded target where fibers with diameters ranging from 3nm to 5μm are generated [50]. This method has been used to make scaffolds for guided regeneration of smooth muscle cells [34]. Figure 2-5 shows electrospun PCL scaffolds.

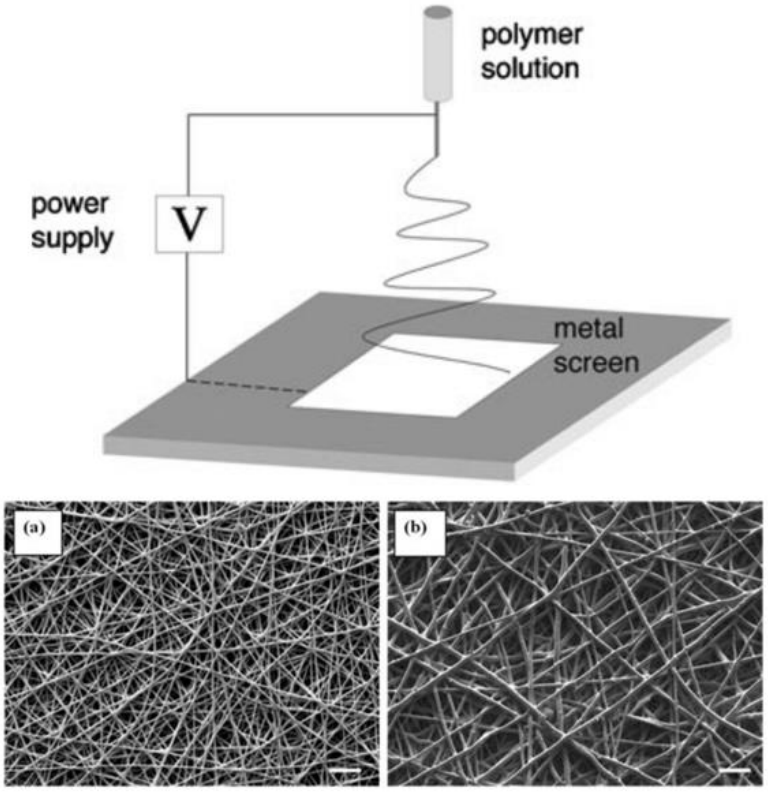

Figure 2-5 Electrospun illustration [51] **on top and (A,B) SEM micrographs of electrospun PLC scaffolds** [52]

3) Freeze drying

Freeze drying is another technique with uses a solvent to produce porous structures [8]. The solvent, usually water, is sublime under specific conditions of temperature and pressure leaving a porous structures with porosities up to 90% [1], [12].

With other non-deterministic techniques like fiber bonding, membrane lamination and melt molding, these lack a full control over the final geometry. These architectures produce with these conventional techniques are control by the process rather the design, being limited by their inability to control the internal geometry of the scaffolds [42]. AM process aims to overcome these limitations by adopting a more control approach.

2.5.2 Additive manufacturing process

Additive manufacturing (AM) consists in a process where a 3D structure is generated by assembling two-dimensional objects in layers. AM process follows a 3D computer aided drawing (CAD) allowing the generation of more complex structures which cannot be made using conventional methods [53]. Moreover, the technique offers a higher control over the fabrication process, increasing the control and quality over the generated structure. Currently, there are several AM processes employed by researches to fabricate scaffolds for tissue engineer [16].

AM process stand out clearly in comparison with traditional nondeterministic methods [19]. The machine-controller layer manufacturing ensures a more control and reproductible process. The inner architecture is no longer product of a random procedure and can be tunable, ensuring interconnected pores allowing the waste removal, cell migration and nutrient diffusion, resulting in improved cell proliferation. It can be adapted with hydrogels, growing factors, or living cells to generate a hybrid scaffold in a controlled way.

Some AM process used for tissue engineering scaffold are described in this section.

1) Stereolithography (SLA)

SLA uses selective polymerization of photosensitive materials to fabricate a desire part [54]. An ultraviolet (UV) laser beam is used following a path defined by the object (CAD model) over molten photosensitive material that will be cure layer by layer into the desired shape. The part is then cured in a UV oven and usually present a followed finishing process [42]. SLA can build complex geometries with a pore size from 250 um and has been used to fabricate heart valves between others. SLA is limited by the range of materials that can be used as the number of steps involved before a finished product is obtained [16], [19].

2) Selective Laser Sintering (SLS)

SLS uses a laser beam to sinter powdered raw material to generate 3D parts in a layer-by-layer pattern using a CAD model [62]. The laser melts the powder together in a locally way. Then, a roller adds more powder on top of it to continue with the layer-by-layer pattern. SLS has been

employed to manufacture ceramic bone implants and clinical implants using Ultra High Molecular Weight Polyethylene (UHMWPE) [55].

3) Extrusion based AM processes

Extrusion based AM process involve the melt extrusion of a chosen material though a nozzle in a layer-by-layer fashion, based in a computer model (CAD model). Each layer consists of the deposition on strand of the melt material in a desired pattern. This section describes extrusion-based technique in detail as is the used method on this research. In general, extrusion techniques can fall into one of the following systems [56] :

1) Screw-extrusion system
2) Compressed air extrusion system (e.g., 3D-Bioplotting)
3) Conventional Rolled feed system or Fused Filament Fabrication (FFF)

Screw-extrusion system consist of a heated barrel that is heated. This barrel is displaced in the X-Y axis and deposited the material in a controlled pattern. The material, generally in form of pellets, is introduce to the barrel by gravity (or in some times by a motor) and is melted and posterior push by a screw-feed system that generate pressure [56].

Compressed air extrusion systems such as 3D-Bioplotting is used to print a range of materials using the principle of melt extrusion (Figure 2-6). The material, in the form of pellets, is introduce in a syringe that is later placed in a hot cartridge. The cartridge is attached to a printing head that have the ability to move in all directions. Following a patter generated by the CAD model and being extrude by pneumatic pressure thought a nozzle, the material is posited in a control way. One of the limitations of this technique is that two materials with different viscosities will be extrude at different rates at the same pressure. Therefore, a relation between the viscosity and the pressure needs to be defined for a more control process.

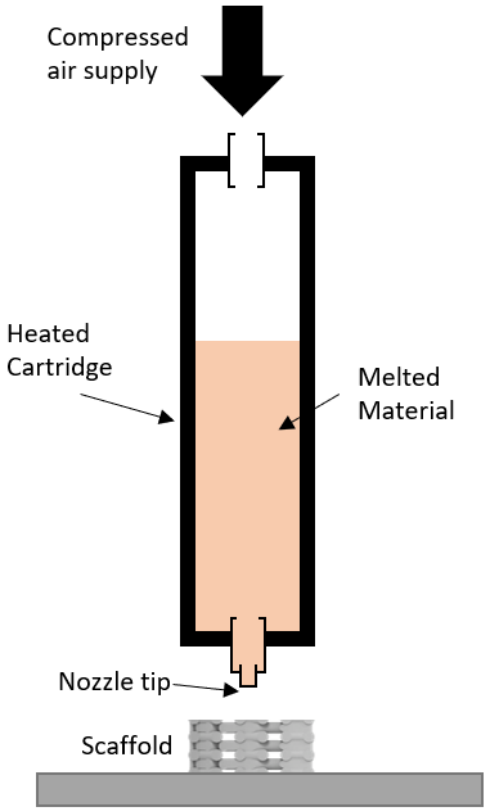

Figure 2-6 3D-Bioplotting setup

FFF based system used a heated chamber in which the material, in form of a strand, is pushed into for melting and a posterior controlled deposition though a nozzle (Figure 2-7). The material is deposited following a pattern generated by the CAD model and the slicing generated. The semi-molten strands are deposited in a movable platform (in the z-axis) [15]. This system is mostly driven by a mechanical motor that push the material throw the system.

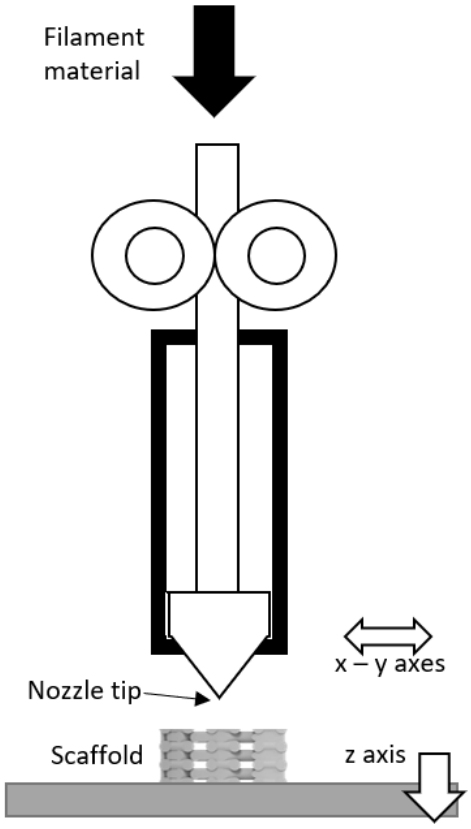

Figure 2-7 Fused Filament Fabrication model

2.5.3 Process characterization studies of extrusion-based AM processes

A review of the literature shows that FDM and 3D-Bioplotting are commonly used extrusion-based AM techniques [17]. Research efforts are shown in this section. Mechanical properties, porosity and surface roughness are some of the parameters that have been studied for AM techniques [56]–[60].

Mechanical properties of printed scaffolds have been given a considerable amount of attention. Lee *et al.* [59] printed scaffolds on a 3D-Bioplotter using PCL and measure compressive modulus and cellular response. The demonstrate that 3D printed scaffolds are 20 to 50 times stronger compared to a salt leached scaffold. They attempt to enhance the mechanical properties by using an oscillating nozzle system, being the oscillating amplitude the only factor that have significant effect. Other groups have studied the mechanical properties of structured fabricated using FDM. Sood *et al.* [57] considered layer thickness, orientation, raster angles and raster gap to parametrically model tensile, flexural and impact strength.

Scaffold porosity is widely studied, being porosity being a direct influent in elastic modulus of bone structures [61]. Honeycomb inner structure pattern have shown a direct correlation between porosity and mechanical properties under compression, with compressive stiffness ranged from 4 MPa to 77 MPa for scaffolds with porosity ranging from 48-77% [58]. Hutmacher and Shantz [62] used FFF to print PCL scaffolds with porosity of 61+-1% and tested biocompatibility with fibroblast and osteoblast. With a compressive stiffness of 41.9 and yield strength of 3.1 they found that the process was highly reproducible, and the cells were able to proliferate.

The review of the literature revealed a gap in studies with respect to process characterization using a 3D-Bioplotter, which this thesis aims to cover.

2.5.4 Rheology in extrusion

As in all extrusion base process, the material rheology has been found to be critical in defining the characteristics of the scaffold generated [63]. A strong problem is found at the nozzle tip where the viscosity plays an essential role in the flow behavior [64]. Since the techniques have shown to be reliable tools to produce repeatable results [64], a common topic under investigation is the model of the flow behavior to have better control over the extrusion. Having the rheological characterization as an essential step for modeling the system. Nevertheless, this also poses a challenge as most of the used material are non-Newtonian fluids [43]. Hence research efforts for generating a relationship between processing parameters and material viscosity during extrusion [43], [65].

Rheological properties of polymers have also been independently investigated to assess their processability. Ramkumar and Bhattacharya [66] characterized rheological properties of biodegradable aliphatic polyesters – PLA, PCL and polyhydroxybutyrate-co-hydromerate (PHBV). They showed that molecular weight of PCL greatly affects the viscosity of it, moreover, that PCL exhibits a shear thinning and shows reduce toughness at lower viscosities.

2.6 Chapter Summary

This chapters describe the basic design requirements of TE scaffolds, which are porous biodegradable structures with a similar mechanical strength to the host tissue. The inner architecture influences the cell seeding and cell proliferation within a scaffold. The material and the fabrication process also determine the clinical success of the scaffold. A series of materials or

composites can be selected for the desire requirement. These requirements are diverse and vary with cell, tissue, age, and gender of the host. Scaffolds fabrication technique can be classified into two big categories, the ones that do not offer fully control over the internal geometry (non-deterministic techniques) and the ones that are AM techniques that offer a complete control. These use CAD models to build the 3D geometry in a layer fashion. 3D-Bioplotting is one of these techniques which have been found to be very sensitive to material viscosity. A review of the literature shows a gap in with respect to process characterization using 3D-Bioplotting which this thesis aims to fill.

CHAPTER 3: THESIS OUTLINE

This chapter present the research objectives and the propose working thesis of this work.

3.1 Research Objectives

This thesis aims to evaluate the feasibility of fabricating 3D composites PCL-BG scaffolds of finite sizes (>1000 mm^3) with high precision and fidelity to designed architecture using the direct ink writing process. Additionally, include new methodologies to efficiently evaluate the architecture of the printed scaffold. The boarder goal is to develop a methodology that can be applicable to scaffolds in a wider range of biomaterials.

Furthermore, the thesis focuses on establishing a critical relationship between the polymer rheological properties (viscosity, loss and storage moduli), processing parameters (compounding method, extrusion temperature, extrusion pressure, printing speed and nozzle diameter) and resultant characteristics of the fabricated scaffold (geometry, mechanical and biological characterization). In order to meet the broader objective, the specific aims defined for this research are listed below:

Aim 1: Establish the effect of 3D-Bioplotting process parameters on the resultant scaffold characteristics

- Determine the effect of processing parameters on the resultant scaffold characteristics (geometry, mechanical strength, and biological response)

Aim 2: Investigate the effect of the addition of BG on the resultant scaffold characteristics

- Determine the effect of the added Bioactive glass (BG) particles on the resultant composite PCL-BG scaffold characteristics (geometry, mechanical strength, and biological response)

Aim 3: Determine relationship between the rheological properties of the material and the printing parameters

- Determine the rheological characteristic of the material at different shear rates and shear stresses over time.
- Determine the relation between the apparent viscosity and the process parameters

3.2 Thesis Outline

The thesis comprises the work done over two years. First, PCL/BG samples were analyzed, introducing the first methodologies. Second, a more systematic study was realized assessing the effect of compounding over the PCL. These two works are merged into a single work in this thesis.

Chapter 4 presents the materials, experimental setup, procedure, and results from the scaffold fabrication experiments. Chapter 5 describes the experimental approach and results obtained in the scaffold characterization. Chapter 6 defines the experimental method and results obtained in the rheological characterization of the material. The thesis concludes with a summary and directions for future research in Chapter 7.

CHAPTER 4: SCAFFOLD FABRICATION

This chapter details the scaffold fabrication and the process to generate a producible sample. Section 4.2 describe the material used in this thesis and Section 4.3 the methodologies applied to them. Finally, Section 4.4 show the results and the chapter inferences.

4.1 Introduction

This chapter addresses specific aims 1 and 3 defined in Section 3.1 of CHAPTER 3: by a prior parameters screening and selection to determine the feasibility of the printing parameters and the range in which the samples can be printed. Furthermore, the geometry is selected and an additional set up is generated to increase the print reproducibility and the similarity withing the design geometry and the printed scaffold.

4.2 Materials

Commercially obtained PCL with a molecular weight (Mn) of 45000 (Sigma Aldrich, USA) and quaternary BG (45 SiO2-24.5 Na2O-24.5 CaO-6 P2O5 wt.%) synthesized by the sol-gel process (as reported previously [67]) were used in this study. The physical properties of the PCL, as specified by the manufacturers, are summarized in Table 4-1.

Table 4-1 Properties of PCL

Name	PCL Mn 45000
Supplier	Sigma Aldrich
Molecular weight	45000
Melting point	~ 60 °C
Density	1.145 g/cc
Physical form	Pellets

To prepare the composite ink for Direct ink writing, PCL and BG were mixed with Dichloromethane (DCM) as a solvent to improve the mixing using a magnetic stirrer at 50 °C, adding enough solvent to enable homogeneous stirring while avoiding decantation of the BG in the solution. First, DCM was placed in a beaker in a pre-heating magnetic stirrer, then PCL pellets were added in small quantities until all pellets were dissolved and the solution was homogeneous. Next, BG was introduced in small batches following the same procedure as PCL. To ensure a homogeneous distribution of the BG, the mixing process continued for 30 minutes in the magnetic stirrer. Once the time is achieved, the material was spread onto metal plates and left inside a fume for 24h at room temperature, enhancing the interaction with the environment for solvent

evaporation. Three mixes (0-, 10-, 20 wt. % BG) were developed and cut in small pieces for this study.

To evaluate the effect of the solvent on the mixing process, scaffold fabrication, and scaffold properties, different compounding methods were applied to the commercially acquired PCL. Following the previous described method, PCL was mixed in a magnetic stirrer with 0% BG using Acetone as a solvent, additionally, PCL and DCM were also mixed. As a third method, the PCL was subject to high shear stress by putting it though screws in a mechanically compounding machine. The MiniLab has the ability to compound high viscosity materials by circulating it in a close cycle at a certain temperature without the aid of solvents. PCL was mechanically compound at 50 °C for 30 minutes, to later being cut in small pellets. Finally, the commercially obtained PCL was used as a control along the study. The different compounding methods are summarized in Table 4-2.

Table 4-2 Different compounding methods

Method n°	Solvent	Combination	BG combinations
1	DCM	Magnetic Stir	0%, 10% and 20%
2	ACE	Magnetic Stir	0%
3	none	Mechanically compounded	0%

4.3 Experimental methodology

4.3.1 3D-Bioplotting

A 3D-Bioplotter (EnvisionTEC, Germany) (Figure 4-1) was used to fabricate the composites scaffolds in this study. This technique involves the extrusion by pneumatic pressure of fluid material – an ink – to form 3D structures [68]. The printed structure is fabricated by the controlled deposition of strands in a layered fashion. A STL file is used to generate the outer form of these structures, later slices into layers and generate by a define inner structure. The working mechanism of the 3D-Bioplotter and its process parameters are discussed below.

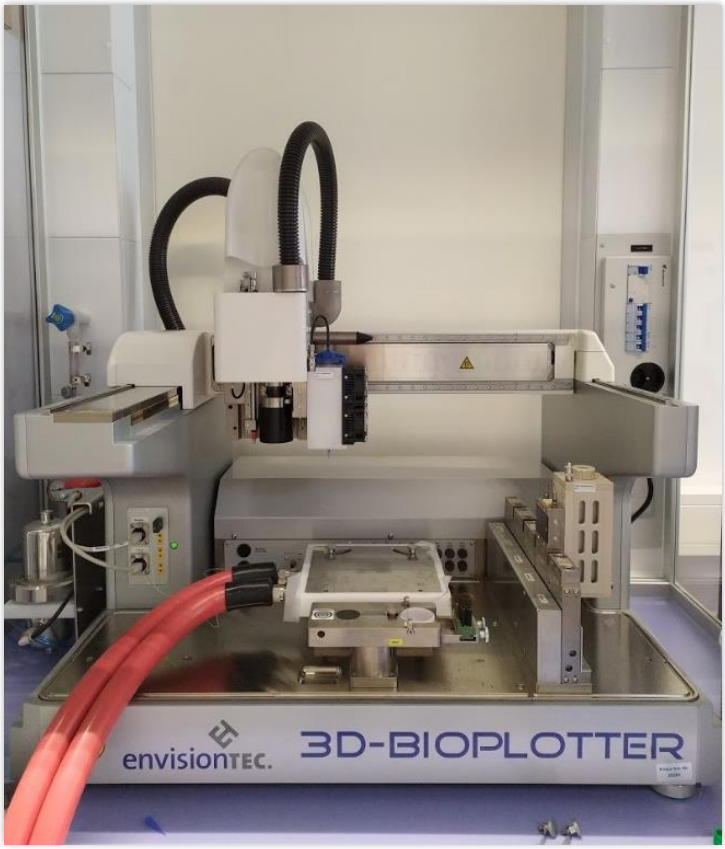

Figure 4-1 3D-Bioplotter by EnvisionTEC

The 3D-Bioplotter consists of a structure with a dispensing head with the ability to displace in the X, Y and Z-axis. Two dispensing head frames – low and high temperature – are available, with each one integrated with his own thermal control and cartridge and can be automatically attached with the dispensing head from the tool magazine to extrude material by pressure into a platform.

The different components of the 3D-Bioplotter and its limitations are described continuously using the technical information provided by the distributor [68].

- Overall size (D/W/H) 623 x 976 x 773 mm
- Weight: ~130 kg
- Build volume X/Y/Z: 150 x150 140 mm
- Linear motors on X, Y and Z axes with a resolution of 0.001 mm
- Speed: 0.1 to 150 mm/second
- Multi exchangeable base plate fixtures
- Platform heating and cooling between -10 °C and 80 °C
- Automatic tool changing system
- Tool magazine with 5 park positions for several dispensing heads.

- Use of multiple dispensing heads (2 out of 5 available)
- Camera for high accuracy positioning in X and Y, as well as strand diameter control with 9 µm resolution
- Needle z pressure sensor with 1 µm resolution
- Positioning sensor in Z for platform attachments with 1 µm resolution

Low-temperature dispensing-head can take up to 30cc in the polypropylene cartridges and extrude the material within a temperature range of 0 °C – 70 °C through a Luer-Lock needles. These cartridges can be safely used with up to 5 bar pressure and 38 °C.

High-temperature dispensing-head (HT Head) has a stainless-steel cartridge that allows to extrude up to 10 mL from room temperature until 250 °C, allowing to print high viscous materials up to the 3D-Bioplotter maximum pressure. The cartridge dives into five parts allowing easily cleaning and maintenance of the equipment.

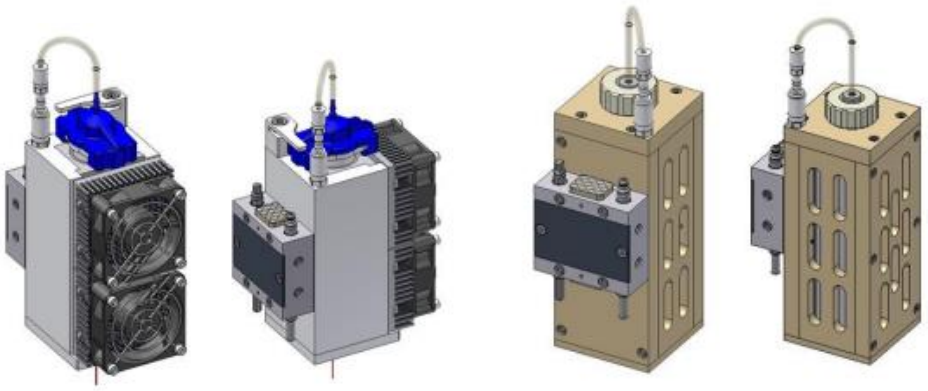

Figure 4-2: Low and High temperature cartridges from left to right respectively [68]

Figure 4-3 Stainless steel cartridge for HT Head [68]

Additionally, a Luer-lock stainless-steel nozzle is used for the HT Head, the nozzle fit in the Luer-lock adapter. The principal characteristic of a nozzle corresponds to the inner diameter of it, this value is determined as the nozzle diameter and define (for an optimal printing process) which is going to be the strut diameter. The nozzle diameter is selected based on the combination of the material flow properties and the aimed strut size. In this study, the head system used correspond to the HT Head.

For 3D printing on the 3D-Bioplotter, the structure must first be designed. A series of software programs are used to create the outer geometry, slice it, define the inner structure, and set up the printing parameters. This process will be explained and discussed below.

1. **Outer geometry generation:** An STL file of the global outer geometry of the structure needs to be generated using a software, i.e., for a cubical scaffold, a cubic STL needs to be generated in this step. For this study, *Magics*® from *Materialise* (Belgium) was used.

2. **Sliced model generation:** The previously STL generated is now imported to the sliced software, BioplotterRP (EnvisionTEC, Germany) was used to slice the desire geometries into a layer shape object. The software opens the STL file, allowing to place the geometry in the printing bed, scale the geometry in case is necessary and duplicate it for multiple geometries printing. Once the part is positioned the software can slice it for posterior printing. The slide height used correspond to the recommended by the distribution, an 80% of the nozzle diameter was used [68].

3. **Material specific parameter selection:** All the 3D-Bioplotter parameters and configuration are defined and controlled in the software *Visual Machines*®. The Material Editor tab is where the different materials parameters are defined. A material definition can be created to assess different material rheological behaviors, the principal specified parameters correspond to Temperature, Pressure and Speed.

4. **Inner structure pattern:** The inner architecture is defined in a layered pattern shape following the defined parameters. First a layer is defined and the properties of it are specified. For each layer, the angle, distance between struts, distance between the contour and off sets are defined. A second (or more) layer can be created.

5. **Model creation:** Finally, the Model tab brings together all the configuration for the printing process. A new Project is defined, and the sliced parts are uploaded. For each part (or just for one) the material and inner pattern is specified. Moreover, it is possible to program if a picture will be taken and how often after each layer, as well as the maximum number of pictures to be saved. In case this number is reached while printing, the new

pictures will replace the first ones. Additionally, a pre-visualization is generated that show the estimated printing time and how the inner structure will look within each layer.

Regarding the physical set up of the machine, the cartridge is filled with the material and the screws are tightened. The whole cartridge is mounted on the HT Head before an operation is run. The HT Head will increase the temperature to the defined material temperature for the station and then the dispensing head will grab the HT Head.

It is recommended before any change on the system to calibrate the HT Head before a run. The 3D-Bioplotter includes an integrated cleaning and calibration station. The calibration consists of a pressure sensor that is push by the HT Head. The nozzle pushes the button, and the Z position is recorded. To calibrate the HT Head on the X-Y plane, the machine extrudes material in a dot shape for a previously defined time (*in Material tab*), following which the camera takes a picture of the printed dot and calculates the center of it. Thus, the new X-Y coordinates correspond to this position. Finally, when running the model, the HT Head will verify the platform with a sensor to measure the height in case an attachment is displaced on the printing bed.

A 3D printing process is subject to a series of parameters, which will determine if the material flows easily, thus leading to a controlled process. The principal parameters are defined by the user and can be modified during printing. The material will be printed at a certain temperature defined as extrusion temperature; this temperature should generally be higher than the melting temperature of the material to have a viscous-elastic liquid properties. This pressure needed to extrude the material though the nozzle is referred as the extrusion pressure, which define how much force will be applied and thus how much material is extrude. This pressure corresponds to compressed air that comes from the in-house system. Then, the printing speed (or dispensing speed) correspond to the X-Y movement of the dispensing head, for an optimal printing process this value will be as close as possible to the flow rate of the material that is exiting the nozzle.

The flow of the material is mainly defined by its rheological properties, but the rate at which it is extruded can be tuned by varying the extrusion temperature, pressure, or needle size. For instance, a printing speed could not match the flow rate a be smaller than it, generating an over extrusion of the material and a reduce accuracy with respect to the desire model. For a smooth printing process, it is essential to have control over these parameters and understand the correlation between them. The degradation of the material plus external factors can lead to additional variations in the printing process and thus changes to the initial defined parameters may be required while printing.

Most of the printing parameters are defined at the beginning of the process and cannot be changed while printing, nevertheless, there are two parameters that can be changed while printing, these are extrusion pressure and printing speed, allowing to make small changes to the extrusion flow and the printing speed in order to ensure uninterrupted printing of the entire specimen.

Extrusion flows represent the rate in which the material leaves the nozzle, this can be tune by changing the material, nozzle size or pressure. On the other hand, printing speed correspond to the speed at which the head moves along the printing bed and is not correlated with the extrusion flow. If the printing speed is smaller than the extrusion rate will mean that a lot of material will be extrude in a small area and thus, the strut will be bigger than the nozzle size. On the other hand, if the extrusion rate is smaller a contrarily effect will happen, less material will be extruded over area having a thin strut and even in some time a non-continuous strut.

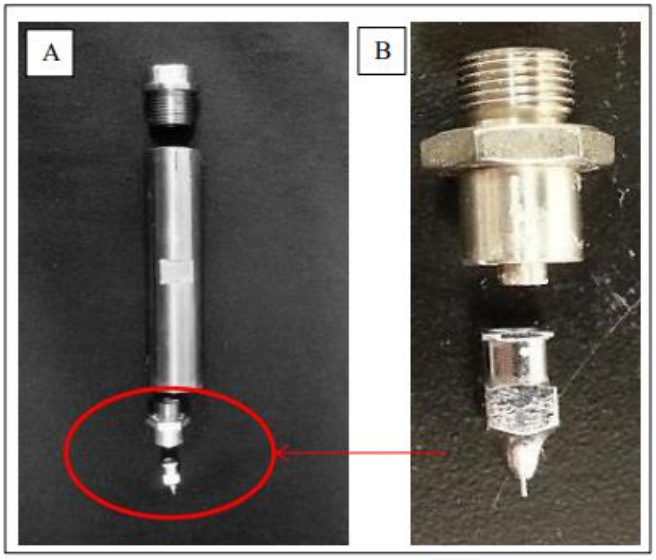

Figure 4-4 (A) Metal syringe that is heated and (B) the ROI with the metal needle and the adapter.

4.3.2 Parameters Screening and selection

A set of screening parameters were carried out to verify the feasibility of printing the different materials and to determine the ideal range for the 3D-Bioplotter configuration. The parameters that affect the 3D printing process are described in the fishbone diagram (Figure 4-5).

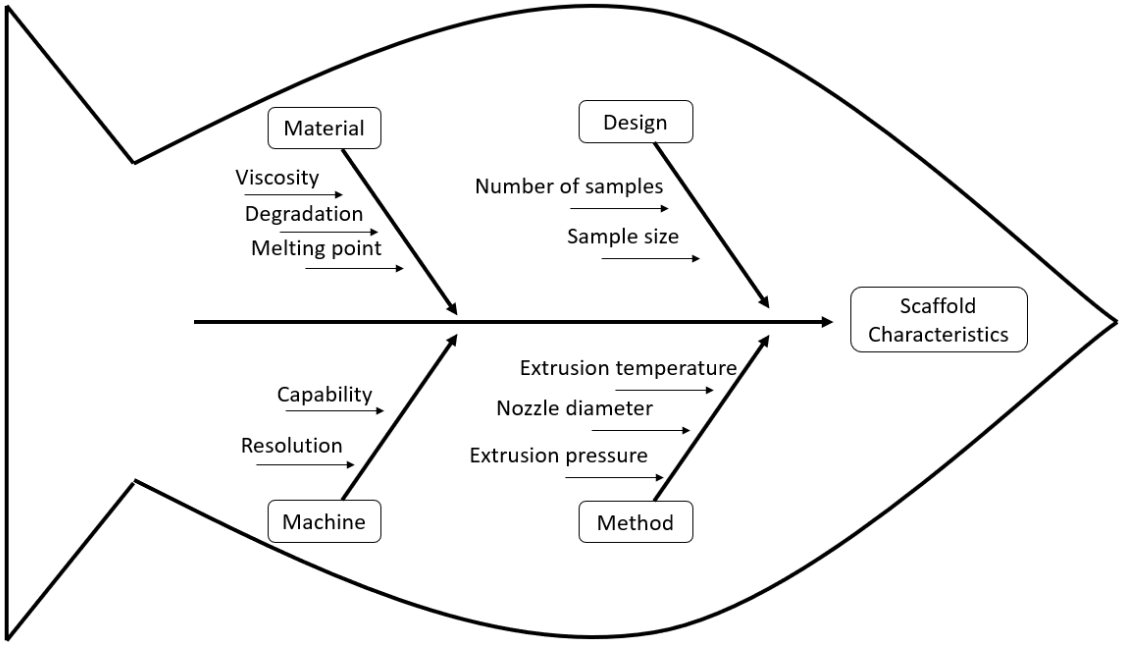

Figure 4-5 Fishbone diagram of parameters that affect the 3D printing process

An initial extrusion temperature of 110 °C was selected since preliminary experiments showed feasibility while printing at an acceptable printing speed (~2.5 mm/s) [69]. This was reduced and increased by 20 °C in a follow-up, systematic approach. The extrusion temperatures of 90, 110 and 130°C were used in combination of different printing speeds and pressures to determine the optimal configuration. Furthermore, a nozzle diameter of 400 µm was chosen for a first iteration, having a relevant size for biological characterization (100-500 µm).

Parameter	Levels
Extrusion Temperature [°C]	90, 110, 130
Pressure range [bar]	6 to 8
Printing speed [mm/s]	1 to 4

Table 4-3 Extrusion parameters range used in this study

4.3.3 Scaffold design and fabrication

Scaffolds were manufacture using the 3D-Bioplotter and the previously defined parameters. Porous scaffolds were defined with 50% porosity and 400 µm pore size, printed with continuous strand in an orthogonal shape. Three different global geometries were used: (a) 5 × 5 × 5 mm^3 cube, (b) cylinder of Ø = 10 mm with 15 mm height (Figure 4-6), and (c) well of Ø = 5 mm with a base of height 1.2 mm and border of 0.4 mm (Figure 4-7).

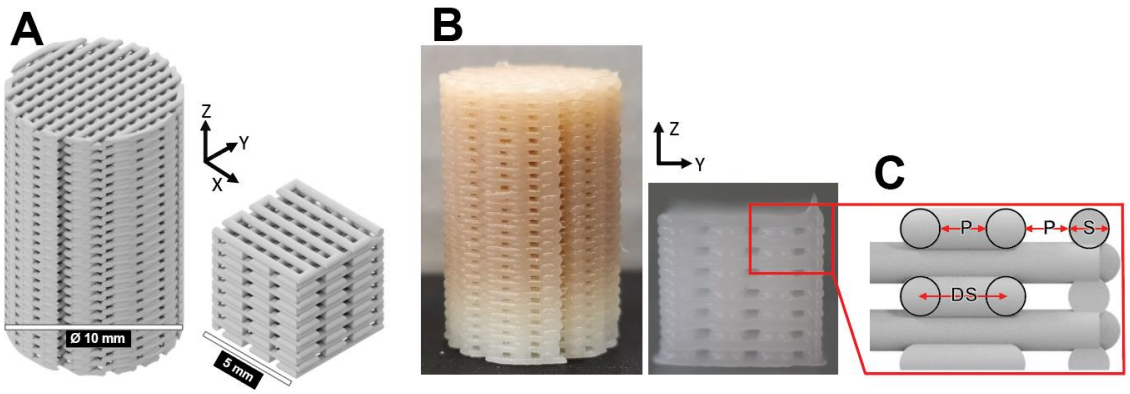

Figure 4-6 (A) CAD model for mechanical and biological performance from left to right respectively and (B) final samples with (C) a correspondingly magnification of ROI in the CAD model showing: pore size (P), strut size (S) and distance between the center of the struts (DS)

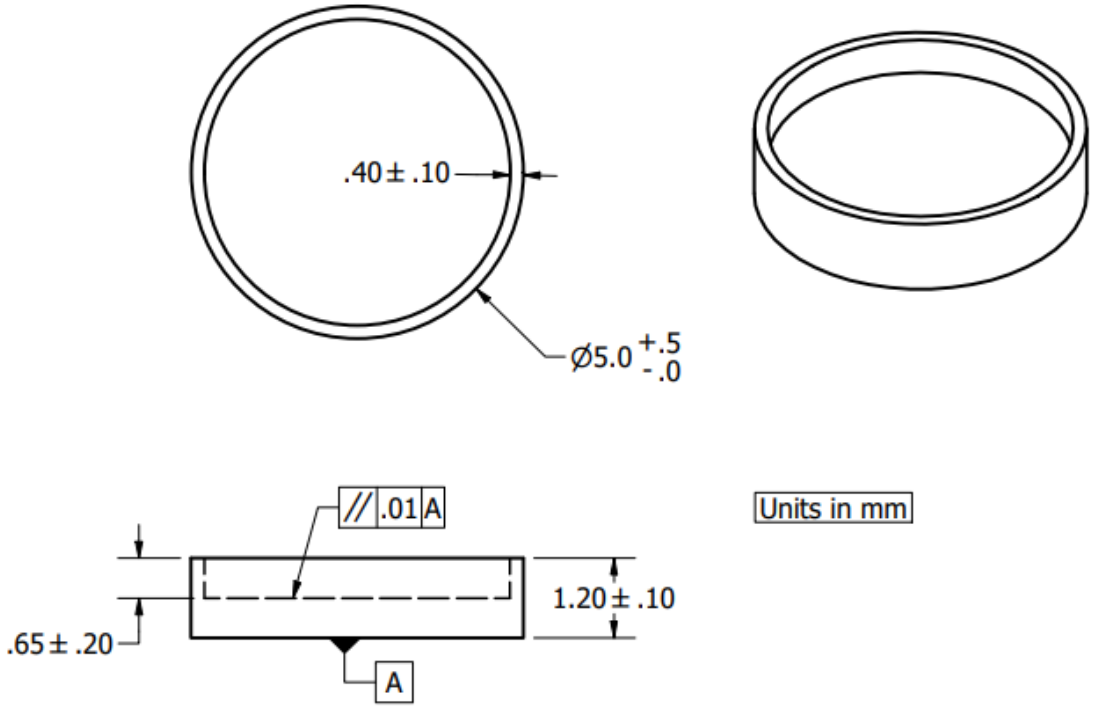

Figure 4-7 Cell Wells design for biological characterization

Samples of relevant size (>1000mm^3) were designed to demonstrate the ability to print "finite-sized" structures following the mechanical standard for compressive test ASTM D695-15 [70]. The structures were designed in a cylindrical shape with diameter (D) 10 mm and 15mm height (h), having a sufficient aspect ratio (h/D) of 1.5 to enable compression testing without having to deal with complications in results related to end-effect and related artifacts.

On the other hand, cubic geometries were standardized geometries for the biological characterization based on methods published previously by researchers at UAI [40]. Furthermore, for a faster and simpler evaluation (e.g., toxicity) of materials, wells were designed to fit in a 96-well culture, unlike other structures, the wells were designed as a solid structure aimed to evaluate the properties of the material and not with the interaction of the inner architecture.

The high temperature cartridge was fully filled with material and maintained in the HT Head at the desired temperature for 30 minutes before printing This allowed the material to stabilize and to decant in the syringe, decreasing the percentage of bubbles. After more than 2000 mm^3 of material was extruded (usually after 2 cylinders or 20 cubes) the cartridge was opened and more

material was deposited, reducing the risk of running out of material at the tip of the nozzle due to the adhesion of the material to the wall of the syringe.

A camera attached to the dispensing head captured a picture after each layer. The capture happens always at the same distance with the sample and places the structure at the center. For big samples, multiples pictures are taken but the program automatically merges them saving just one picture per layer in a folder. This folder has the name of the project and details the time and date in which was printed. The pictures are later analyzed. (See Chapter 5 for details)

Table 4-4 show the chosen parameters for a print process, where the aimed strut size corresponds the designed strut, equals to the needle size, The distance between the strands correspond to the distance between the center of the struts and is calculated by adding the pore size and the strut size for a pore size equals to the strut one. Finally, layer height is calculated as the 80% of the strut size as recommended by the distributor [68]. Table 4-5 summarizes the design parameters for each geometry.

Table 4-4 scaffolds parameters for a print process

Scaffold property	Specification
Aimed strut size [mm]	0.4
Distance between strands [mm]	0.8
Layer height [mm]	0.32

Table 4-5 Summary of the scaffolds specification for the different geometries

Cylinders		Cubes		Wells	
Diameter	10 [mm]	Width	5 [mm]	Diameter	XX [mm]
Height	15 [mm]	Height	5 [mm]	Height	XX [mm]
Structure	Porous	Structure	Porous	Structure	Solid

4.4 Results and discussion

4.4.1 Parameter screening and selection

A first evaluation was realized to determine how to address the search for the optimal printing parameters. Lines were extruded at 110 °C with a nozzle of 0.4 mm diameter at different pressures

and speed. The attached camera recorded a picture of each line after printing and the diameter of the strut was measured using a custom-written python script (Methodology explained in Chapter 5).

Figure 4-8 shows the correlation between the extrusion pressure, printing speed and the strut diameter. The printing speed corresponds to the speed at which the head moves in the table while printing and is set up as a parameter, meanwhile, the flow speed is a result of the viscosity, needle size and pressure applied between others. Ideally both, the printing speed and flow speed should be similar to extrude a homogeneous strut equals to the needle size. Color lines represent the different evaluated pressures, meanwhile, the grey a prior estimation. Dots are values recorded changing the speed and measuring the generated strut width. It can be seen that increasing the pressure at a certain speed the strut diameter increases, as expected. As well, increasing the speed at a certain pressure makes the strut thinner as the same amount of extrude material is being deposited in a larger zone. This phenomenon is the expected for this type of material. Furthermore, can be correlated with the rheology results explained on Chapter 5. The difference between the estimation and the experimental values can be due to the extra fan set up, as the fans where not always pointing to the heated needle and thus, the temperature increase over the used in the estimation.

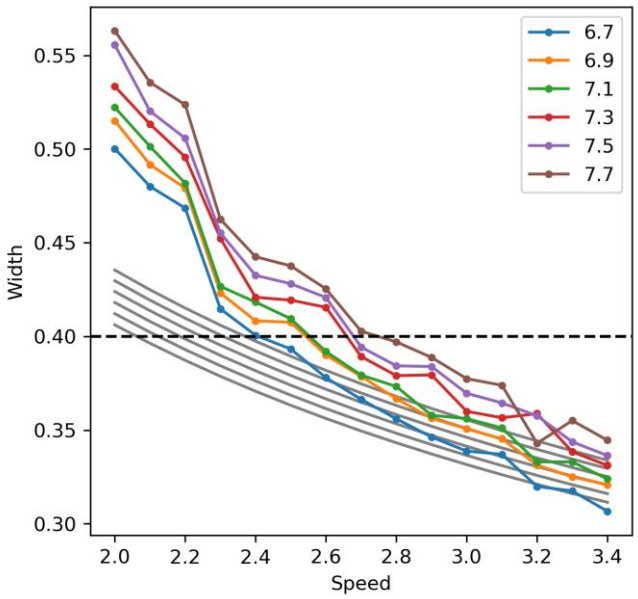

Figure 4-8 Correlation between the pressure, printing speed and generated strut diameter. Where Width refers to the strut diameter in mm, speed to the printing speed in mm/s and the legend to the use pressure in bar. Colors dots represent the adquires combinations,

dash line to the desire combination for a strut diameter equals to the needle size of 0.4mm. Black lines represent a forecast on this result that is explained in Chapter 6.

For all the materials the extrusion was feasible, nevertheless, the optimal printing configuration was defined at the beginning of each printing to have a continuous process and avoiding re-heating of the material and degradation of the material. Contrary to what expected, PCL-BG composites presented a similar optimal configuration, composites with bigger particles usually show higher viscosity and thus longer printing times at the same pressure. Later rheological results showed how the alignment of the particles at the used flow rate (shear thinning behavior) makes the viscosity to be like the pure PCL condition. Table 4-6 summarizes the range of used parameters for each extrusion temperature, the applied pressure was the maximum available from the in-house pressure system, this was similar for all conditions and was decreased just after necessarily.

Temperature [°C]	Speed [mm/s]	Pressure [bar]
90	1 to 1.5	7 to 7.5
110	2 to 3	7 to 7.5
130	3 to 3.7	7 to 7.5

Table 4-6 Summarize of used parameters for different temperatures

4.4.2 Scaffold fabrication

Samples without BG were printed following the previously explained methodology. With the preliminary experiments, a series of initial parameters were defined. Nevertheless, these vary along the fabrication of the structures due to multiple reasons. It is essential to address these variations to decrease the discrepancy along the process for more homogeneous and better-defined structures. The method how these variations were dealt with are described below.

Temperature is dominant factor for high-temperature 3D-printing. The process uses temperature to melt the objective material, decreasing the viscosity, and allowing the extrusion of it. It is important to use the adequate temperature for a nice flow, higher temperatures could mean faster printing process but also a quicker degradation of the material or to the increase of variability in the process. In addition, once the hot liquid material is deposited on the print bed, it will continue to flow until it reaches a more stable phase, as its temperature decreases. Higher printing temperatures will cause this phenomenon to increase and therefore the desired shape will have a

greater alteration than a lower temperature extrusion, producing a different strut size than the one designed, compromising the fidelity of the structure.

Moreover, some materials exhibit a freezing temperature lower than its melting point, being this the case of PCL, a preliminary DSC at 20°C/min showed that the melting point in around ~60 [°C] but the freezing point is around ~40 [°C]. External cooling system decrease the temperature even faster, meaning that the freezing point could be even lower. This behavior that demands a fast decreasing of the temperature to avoid the dispersion of the material once deposited. This performance is exhibited in [71] where the printed struts cannot bear the external forces (gravity) and they diffuse because of the low cooling rate, getting the struts closer and losing the defined strut thickness and, consequently, the pore size.

Furthermore, the temperature problem increases when trying to print a finite-sized 3D scaffold, a single layer will eventually spread until it reached a certain temperature to withstand his shape. 3D scaffolds present multiple layers printed one upon the other. Lower layers may be able to withstand their own weight, but they will need to withstand upper layers. Moreover, the extruded layer will arrive with high temperature and by conduction will increase the temperature of the layer beneath it. This problem can be solved by increasing the time between the layers, being long enough for the layer to reach a stable temperature. Nevertheless, this would mean significantly high printing times and solving just the multi-layer problem but not the single layer diffusion. A common technique is to decrease the large printing times is to print several samples simultaneously; this allows for a layer to cool down while another, not on top of it, is being extruded. Single strut problem is better explained by the storage and loss modulis of the material, rheological properties that are addressed with detail in Chapter 5.

Commercial printers solve both problems by changing natural convection with a forced convection induced by fans aimed at the extruded material. This quickly reduces the strut temperature, and the shape is not lost. However, if this change is too fast, the layers will not bond together and therefore the properties of the structure will be diminished. This is solved either by decreasing the fan speed or increasing the extrusion temperature allowing a certain level of diffusion (flow of the material) and a proper bonding between layers.

As 3D-Bioplotter lacks an in-built cooling setup for high temperature materials, a custom-made setup was developed to increase the control in the process and to ensure the good fidelity of the

printed samples. The set up consists of two fans placed on opposite positions of the printing bed and pointing to each other, powered by an external energy source and running for the whole printing process, they perform in a parallel sequence at 12 [V]. The airflow was set up at the minimum and was kept constants for all the samples to reduce variability. The radial fans with dimension (Ø 101 x 52 mm) created an airflow direct to the base of the sample and to the critical corners of it. The definition of the critical corners corresponds to the corner that had the lower time to cool down before another layer is being deposited upon it, in other words, the first point where the upper layer touches the last printed segment of the one beneath it.

In this study at least two samples were printed simultaneously, leaving an extra time to ensure that the layer is sufficiently/adequately solidified (or cooled) to support the next layer. Cylinders were printed in the middle of the printing bed with a 20 mm separation. Cubes and wells maintained the same inter-specimen distance but were designed in a centered matrix of 3x3 as the printing time per layer is lower than the cylinder geometry.

The temperature plays an important role when it comes to the adhesion of the first layer to the printed bed, not having a good attachment of the first layer with the surface would mean the displacement of the sample and therefore the end of the printing process. For big geometries or long printing times this could mean a considerable loose of material and time. While the material is being extrude a shear force is apply to the geometry, the material is not always nicely deposited and usually make a horizontal force to the sample, for taller samples this force becomes bigger and therefore a better adhesion is needed.

Commercially 3D printing addresses this problem by heating up the printing bed or using more adherent surfaces. The 3D-Bioplotter is set up with a stainless-steel base, being this not the ideal for low adherent materials like the PCL, relevant size structures with more than 10 layers usually undergo by the shear forces generated and get loose while printing, especially with high aspect ratio samples where the attach surface is way smaller than the height, even more for porous structures where thin struts are the only interface between the sample and the printing bed.

Increasing the bed temperature will usually increase the adhesion with the base, nevertheless, will have a negative impact on the cooling rate of the sample. This was evident in a preliminary study where 20 scaffolds cubes (following the described design) were printed, having as a result just one fully complete and the others affected by the high diffusion.

To increase the adhesion of the printing parts an adherent or a rougher surface is used. In this study a Kaptone surface was placed and attached with the metal fixators. This material reacts to the temperature and improves the bonding with the surface. Additionally, a thin layer of glue was applied before each process to increase the adhesion (of the first layer) of the sample.

Porous scaffold structures present thin struts that act as the only attachment with the printing bed. With the purpose to increase the adhesion surface, a commonly used technique is to force a diminish of the distance between the nozzle and the printing bed for the first layer, this will generate a wider strut but a shorter layer. Wider struts for the first layer will mean an increment of the adhesion area, nevertheless, this will decrease the size of the first pore size. In Chapter 5 this effect and its consequences are explained in more detail.

Heating up the printing bed is another technique to increase the adhesion of the material. Furthermore, it is a mechanism to avoid warping of the sample. Extruded material expands slightly, as it is still hot, but contracts as it cools down. Having different temperatures along the structure, if this shrinkage is big enough the bottom layers will tend to bend, with bending upwards as an easier direction and therefore detaching from the printing bed. Usually, this phenomenon is seen at the corners of long structures that were cooled down too fast (Figure 4-9).

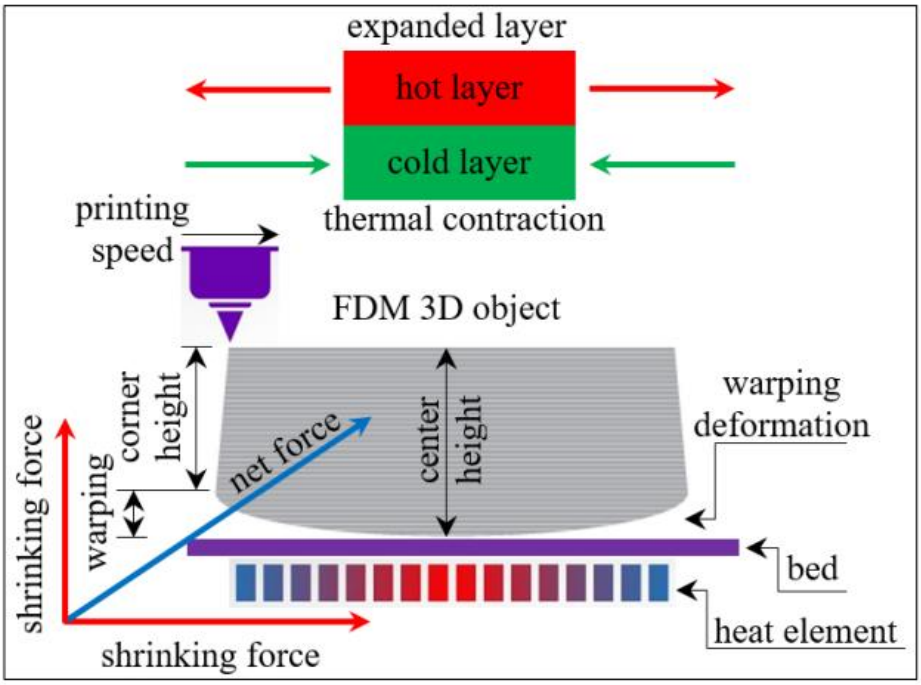

Figure 4-9 Representative sketch of shrinkage of samples while 3D printing [72]

For this study, no bed temperature was used, as the problem was otherwise, the structure usually records more temperate than the optimal one. Nevertheless, a preliminary series was realized were a 40 [°C] printing bed was applied, showing samples that cannot bare his own weight and melt losing the lower porous structure. This was later explained in Chapter 5 where the freezing temperature of PCL was 40 [°C], value lower than the melting point of 60 [°C] for DSC experiments.

Printing parameters were initialized as the one described in the previous section. For each load of cartridge, a low number of layers were printed and the taken image was analyzed on the spot with ImageJ (National Instituted of Health, USA). First, the pixel size was calibrate using the known strut distance, which can also be described as the distance between the border of parallel struts. Second, random struts were measured, and the average was reported. Third, if the strut is bigger or smaller than the desire one (0.4 [mm]) a change on the printing speed was made. These steps were repeated for each layer until the strut match or has an error small enough to be accepted, usually a deviation of 0.01 [mm] from the desire value was allowed.

Once the parameters were tuned for the desired configuration, the printing process could be started. To effectively ensure that the printing parameters were still within an optimal range, the struts were measured in random layers. In case the value slightly diverged from the designed value, a change was made. For big errors on the printing process, the extrusion was stopped, and the specimen saved for future experiments.

Once all these difficulties were assessed the process behaved as a regular 3D printing. The fail rate was kept low, and the printed structures had a defined structure similar to the theoretical design. For all the samples, day, orientation, position, and time in which was printed was saved. All this information was used to correlate in case an unexpected behavior.

The inferences of this chapter are going to be explained continuously.

4.4.3 Inferences

- Initial parameters screening can be done by lines before printing, these gives enough information prior printing to have a reference of speed, temperature, and pressure to be used. As expected, the increase of pressure increases the printed strut size, as well, the decrease of speed increases the strut size.

- The PCL samples printed at high temperature requires an external fan set up to decrease the printing times and increase the quality of the printed part. The fan set up effectively decrease the temperature of the sample, increasing the success rate.
- Another recommended technique is to print several samples at a time, this will give more time for the cool down without scarifying the total printing time. Nevertheless, an error would mean the loss of both samples.
- Contrarily as recommended for standard 3D printing, heating up the printing bed reduce the number of success prints. Small samples do not present shrinkage on the corner and thus the heated printing bed will just increase the adhesion, factor that is address by the addition of glue to it.

The scaffolds fabricated in this set of experiments used experimentally set up parameters, aiming for the greater possible similarity with the design. Samples were later evaluated; this is detail in the next chapter. Furthermore, the ink was rheological evaluated in aim to understand better the development at the tip of the nozzle and how the printing parameters affect the result part.

4.5 Chapter Summary

The experimental approach and procedure employed to print scaffolds using PCL-BG on a 3D-Bioplotter is describes in this chapter. A set of preliminary experiments were performed to determine a feasible range of process parameters, extrusion temperature, nozzle diameter, printing speed and extrusion pressure. Scaffold were printed under different conditions to determine the ideal set up, being two fans for a fast cooling of the sample. Scaffolds achieve a good quality, and the printing process was finished without mayor complications.

CHAPTER 5: SCAFFOLD CHARACTERIZATION

This chapter details the scaffold characterization and the process to generate a method to verify print quality. Section 5.3 describes the experimental methodology for all the different used approach. Section 5.4 the results given by these methods and finally the Section 5.5 the inferences of the chapter.

5.1 Introduction

This chapter addresses specific aim 1 and 2 defines in Section 3.1 of CHAPTER 3: by a new methodology to characterize scaffolds. The used scaffolds are the one described in the previous chapter and the characterization is based on the literature and new applied approach to TE.

5.2 Materials

Previously printed samples were used along this Chapter. Scaffolds were store in a dry compartment protected to the sun and the characterization was realize between a month.

5.3 Experimental methodology

5.3.1 Microarchitectural properties (code, magnifier glass, SEM)

For TE and to have a proper cell growth is essential to generate structures with an interconnected-porous matrix that allow the flow of nutrients and the remove of waste. This will allow the cells to attach to the inner architecture and develop. Currently, invasive techniques are being used to ensure/check the inner quality of the printed structures. Usually, a horizontal cut is performed to the sample and Scanning Electron Microscopy (SEM) capture an image from a transversal section of the inner geometry. These techniques allow to represent partially the group of samples but cannot be perform for each one of them as they produce invasive changes on the samples. Moreover, other techniques include Micro Computed tomography (micro-CT) that is used to digitalize the volume of the structure, generating the possibility to discover the whole inner structure without affecting the overall geometry. Nevertheless, this technique is highly expensive and time consuming, reducing the possibility to scan all the printed structures. Furthermore, have been shown that this long exposure affects the material properties of the PCL.

To ensure the inner architecture and the quality of the printing process for each sample, a custom code was developed to measure a series of characteristics using the pictures acquired with the 3D-Bioplotter while printing. These images represent each layer of the printed samples in a superior

view, showing printed inner structure in a cross-sectional view. The custom macro was first developed in 2019 in ImageJ (National Institute of Health, USA), being able to measure the strut and pore size for each layer. Figure 5-1 show the process of the code, where a ROI is selected from a superior image and later the code automatically recognizes the pore size. In 2021 the intern Miguel Pardo, under supervision, translates this software into a more optimal and versatile platform. The new software was developed in Python where the multiples images can be analyzed at a faster rate and allowing the postprocess can be done in the same language.

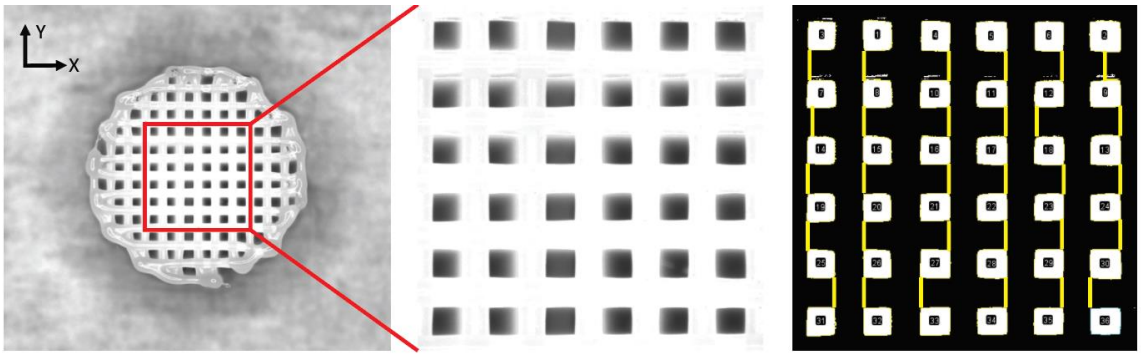

Figure 5-1 Left to right, captured image with ROI showing the pores of interest converted, zoom of the image that later by a threshold transform to the right image. The lines represent the measured orthogonal distances between two adjacent pores.

All the cross-section images are saved and grouped per sample, material, and printed temperature. The software handles this aggrupation to define the parameters used for each series of images. Once is run, an image is open and a Region of Interest is selected by the user, this will indicate in which zone the measurement wants to be done. Having all the samples being printed using the same design, the ROI remains the constant for all the pictures. The picture suffers a thresholding and a morphology transformation to close small holes due to light distortion. The black and white picture represent in black the printed strut and in white the pores of the inner structure for each layer.

For each sample, all the layer information is stored. First, the software defines an invalid pore if there is no pore and (an error in the printing process fills it with material) or if recognize an alteration in that position as a string. This usually can happen near the end of the printed layer where some material might not be properly deposited and is carry around by the HT Head until falls from it generating a string on top of the sample.

An array stores the information for each pore, these as well, are recognized and the position is saved in a two-dimensional array, representing the grid generated by the image. The software measures a series of values defined continuously.

- Strut size: the distance between two adjacent pores, the diameter of the extrude material. Can be considered the most important parameter as is the one that is directly influence by the relation of the flow and the printing speed.
- Pore size: defined by two adjacent struts, depends on the strut size. This value is crucial for cell culture.
- Area: The area of the pore surrounded by struts.
- Perimeter: The perimeter of the pore that represent the outer shape of the pore.

Figure 5-2 represent the initial algorithm of the code, with a strict criteria to define invalid and valid pores for the posterior analysis. Green are correct pores, and the other colors are invalid pores. Red represents a split pore, meaning that the pore is divided in two areas or more, orange to a low circularity value (later explained) and purple to a to small pore that did not fulfill the

minimum required area. All the invalid pores were not taken in consideration for future analysis and grouped and presented as invalid pores.

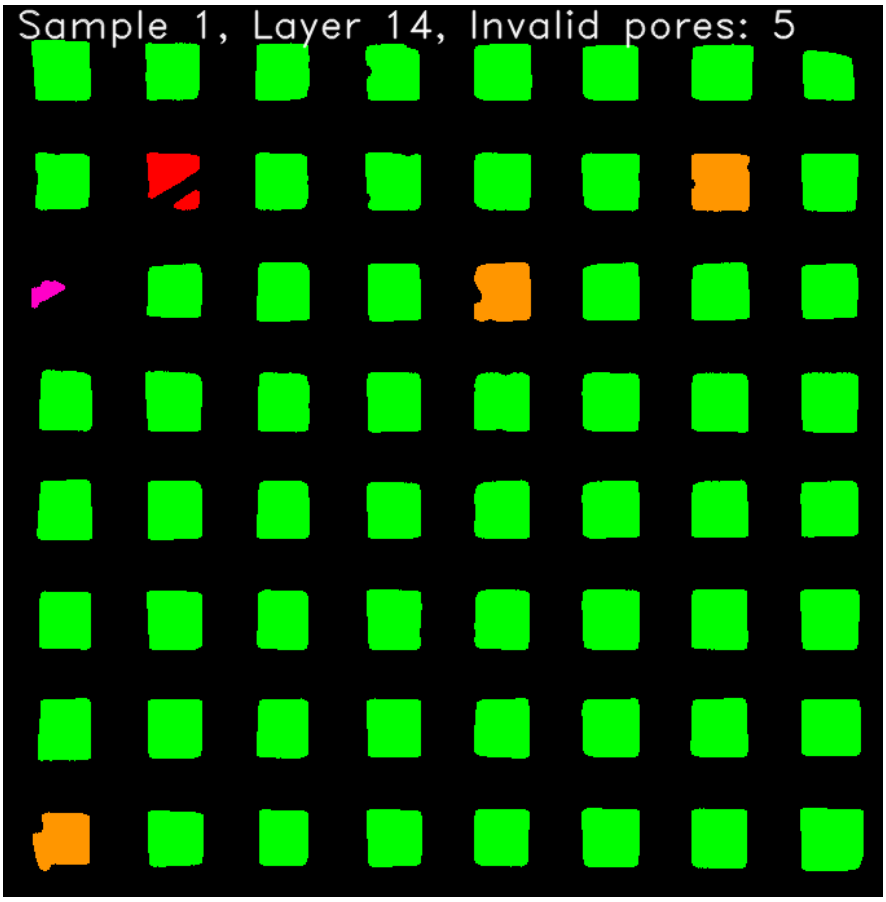

Figure 5-2 Automatic recognition of invalid pores. Where green are correct pores, and the other colors as invalid pores. Red represents a split pore, orange to a low circularity value and purple to a to small pore.

With all this information is possible to follow trends along the samples at its inner structure. A later code recovers this data, analyze, and graph the information. These are present as singular value, average or frequency, grouped versus the material, layer or extrusion temperature. Moreover, the combination of some lead to other factors of interest. The circularity of a pore can be calculated by Equation 5-1.

$$Circularity = (4\pi * Area)/Perimeter^2 \qquad \text{Equation 5-1}$$

This define how similar is the pore to a circle, Figure 5-3 represent the different shapes and the values that these have, with the desire geometry (square) being 0.785. Finally, the percentage of invalid pores is also reported for the different combinations.

Since the in-built camera position was such that, it only enabled imaging of the x-y plane, in situ layer-by-layer strut height could not be measured. However mean strut height was inferred after printing each specimen by measuring the specimen height and dividing it by the number of printed struts. Finally, Figure 5-4 summarizes the code algorithm.

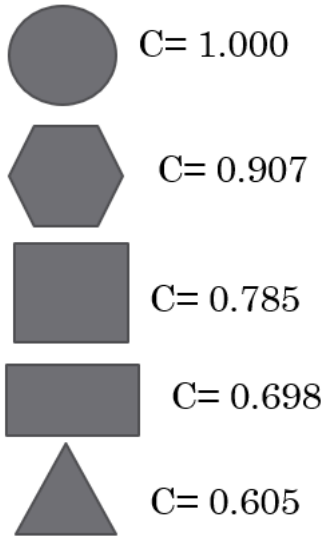

Figure 5-3 With C as circularity, the image shows the circularity value for the different shapes following Equation 5-1

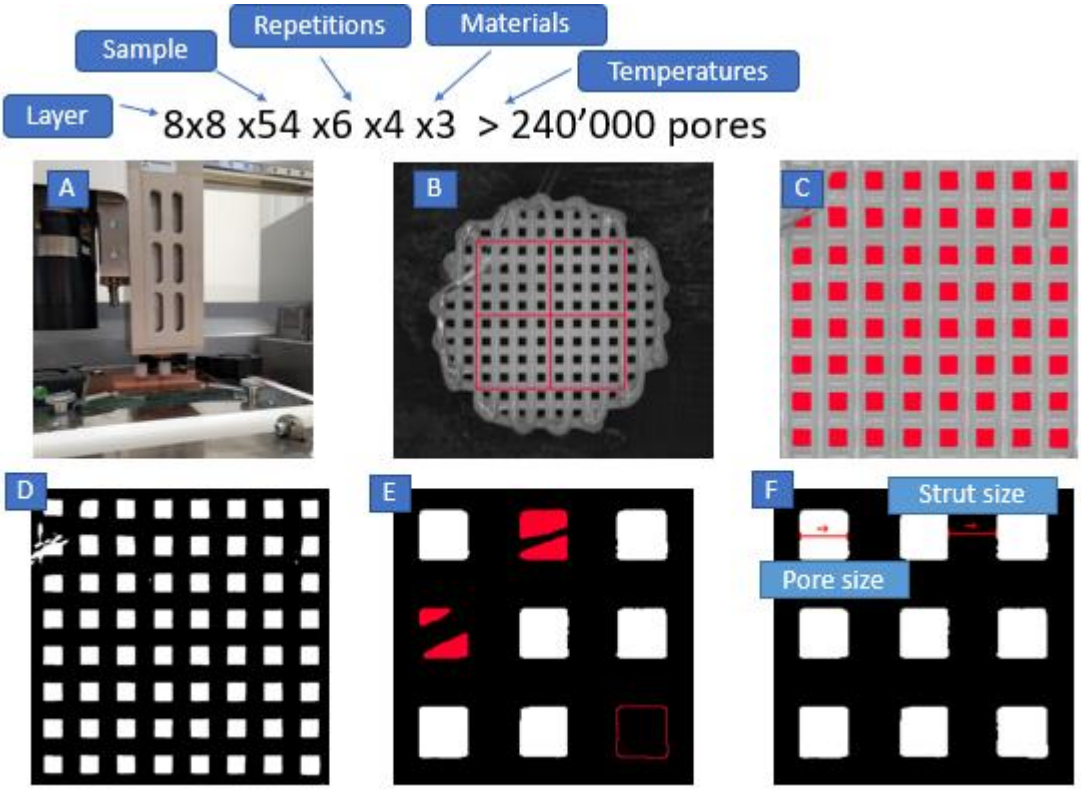

Figure 5-4 The algorithm process for the code analyzer, where A correspond to the bioplotter printing with the attach camera on the left (black cylinder), (B) the generated image with the ROI for pores to consider, (C) an automatic recognition of the pores by a threshold and (D) the result of the threshold in binary, where the white spots represent the pores. (E) shows in red the invalid pores and (F) the different made measurements, where Pore size is the distance between two struts and strut size the distance between pores. Finally, on top, an aporximation of the pores analyzed, with 8x8 matrix per layer, and 54 layer per sample, 6 samples per material, with 4 different methods and 3 materials, sum a total of more than 240´000 analyzed pores.

To ensure that the code is working properly and to compare the results with the literature methods, a magnifier glass was used to capture a picture to the upper and bottom layer of each sample. These were measured manually and with the software.

Moreover, a series of selected samples were attached to an aluminum sample holder and sputter-coated with a platinum layer of 2–4 nm (Leica ACE200, Leica Microsystems, Weitzlar, Germany). Specimens were sliced with a razor to obtain cross-sections (x-y plane) for SEM analysis. The SEM images were obtained with a scanning electron microscope (FEI Nova NanoSEM 230, USA)

in high vacuum mode, and analyzed for printed quality and surface morphology. Both secondary electrons (ETD) as well as back-scatter electrons were used for imaging. In addition, a chemical analysis was performed with an energy dispersive X-ray spectroscopy (EDX; Oxford X-Max SDD detector) to verify the presence of the main elements of the bioactive glass in the printed specimen.

5.3.2 Overall characterization (microCT, Porosity)

To assess the overall geometry and the quality of the printing process. The scaffolds were subject to a series of experiment to determine overall dimensions, porosity, and general structure.

The external dimensions of the samples were measured with a calibrated digital caliper (+-0.02 mm), height (h) and diameter (d) were measure and the average and standard deviation was used. Height was measure 9 times following a 45° rotation after each measurement, as well, Diameter was measure in three different positions: base of the sample (layer 2-4), midpoint (layer 20-24), and top part (50-52). For each position three values were recorded and the average of all of them was used. The overall volume was calculated following the Equation 5-2.

$$Overall\ Volume = h * \pi * d^2/4 \qquad \text{Equation 5-2}$$

The porosity of the scaffolds was determined based on Archimedes' principle. This principle allows to measure the volume of a structure by knowing the dry and submerged weight of it. Figure 5-5 summarize the method, were:

The volume (overall dimensions) of the specimen is measured, weighed in a normal scale, and then submerged in a liquid with known density. Once the specimen is submerged, the volume of it, displace the same volume of liquid, generating a buoyant force into the sample by the liquid that wants to come back to its original position, producing a force that tries to elevate the sample. To measure the force applied to the sample, the wet weight is subtracted from the dry weight.

To know how much the volume is of the displaced liquid, it is important to know that this force correspond to the weight of the displace liquid. Knowing the density of the liquid, it is possible to divide this force by the density to know the volume of the displaced liquid. Therefore, the volume of the part is equal to the displace liquid by the Archimedes principle. Then this volume is divided

by the overall volume of the sample to have the solid ratio of the sample. Nevertheless, the porosity is defined as the void volume of the sample divided by the overall volume, consequently the solid ratio is subtracted from the overall volume to calculate the porosity of the sample.

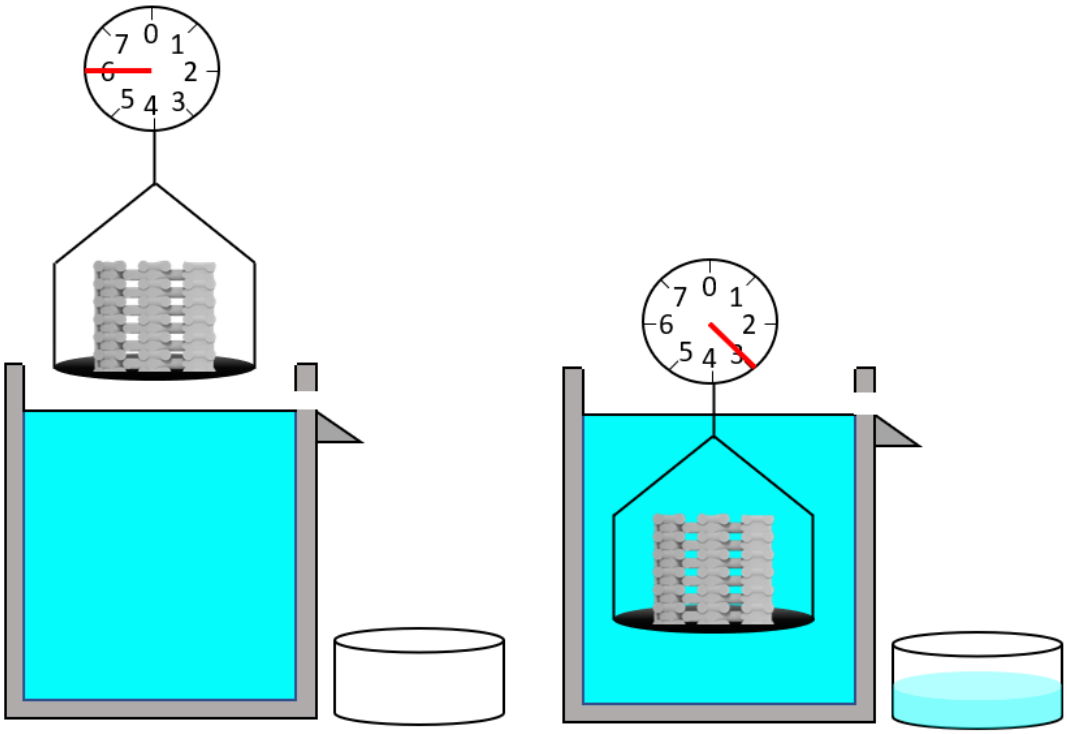

Figure 5-5 Method based in Archimedes' principle to measure a volume by the displace liquid

The porosity was acquired using the previous define profess using a fluid with known density; in this case 70% ethanol solution [73]. A digital balance (Mettler Toledo AT400, USA) recorded the weight of each dry samples, and with a buoyant basket the weight under liquid to get the experimental porosity by the Equation 5-3.

$$Porosity = 1 - (P/T)/(V_{total} * \rho_{ethanol}) \qquad \text{Equation 5-3}$$

Where P the dry weight, T the weight submerged in the liquid, V_{total} the overall volume of the sample and $\rho_{ethanol}$ the density of the liquid.

Micro-CT scans were conducted to verify that the distribution of BG was homogeneous throughout the printing process. Images were acquired in a (EasyTom Micro, Rx Solutions, France), with a voltage of 40 kV and current of 600 µA, frame rate of 4 fps and average of 3. Each

scan of 360◦ took 20 min to achieve a resolution of 4 μm. First, the software RX Solutions preprocessed the images to generate a volumetric dataset that is exported in layers along the z axis. These images were then analyzed in Avizo Fire 9.7.0 (Thermo Fisher Scientific, USA). One sample per condition was captured and analyzed, placed in a metal endcap to avoid undesired rotation of the specimen while scanning.

5.3.3 Scaffold mechanical properties

Printed scaffold specimens were tested in compression in a Z010 universal testing machine (Zwickroell, Germany) with 10 kN load cell. Specimens were placed in metal endcaps to reduce end-effects. Testing was carried out under a displacement control protocol with a crosshead displacement rate of 1.00 mm/min. Specimen deformation was measured with displacement transducers on either side of the specimen. The test was carried out according to ASTM D695-15 [70]. Apparent Young's modulus (E-mod) was calculated by linear regression of the nominal stress-strain data from the linear portion of the curve, generally between 0 and 2% strain. The yield stress and strain were acquired using the offset method, displacing the linear segment by 1% [74] along the x axis. The y- and x-coordinate values of the intersecting point on the nominal stress-strain curve were used to determine the offset yield stress and strain respectively.

A custom-written python code was realized to optimize the data analyze of the wide range of mechanical analysis. The code reads in the raw data from the test having as an input the force and displacement of the experiment. Then, the apparent Stress is calculated by Equation 5-4. and Strain by Equation 5-5. Both the area and the height are represented with the experimental data that is defined as another input. The software labels each stress-strain curve by the parameters of fabrication, this information is used later for comparison of the different groups. The code automatically finds the elastic modulus by derive the stress-strain curve and find the values that represent the linear sector with the same slope. Then this linear regression is extrapolated, and the graph is displaced to start from the origin deleting the toe region. Moreover, the linear regression is displacing a 1% following [74] along the x axis and the intercept is recognize as the yield point, both yield stress and yield strain are saved.

$$\sigma = F/A \qquad \text{Equation 5-4}$$

$$\varepsilon = dL/L_0 \qquad \text{Equation 5-5}$$

Where σ is the stress, calculated by the force (F) divided by the area (A) of the sample, and the strain (ε) is calculated dividing the measured displacing (ΔL) by the initial length (L_0).

For all the points a local regression is done to homogenize the x axis with a step of 0.0001. For each group of variables, the data is merge, showing the average and 95% confidence interval. The custom code can be found in Annexes. Figure 5-6 shows the automatic recognition of the linear segment and then the erase of the toe region and the start at the origin, furthermore, the slope is displaced in the x axis and the code report the interception as the yield point.

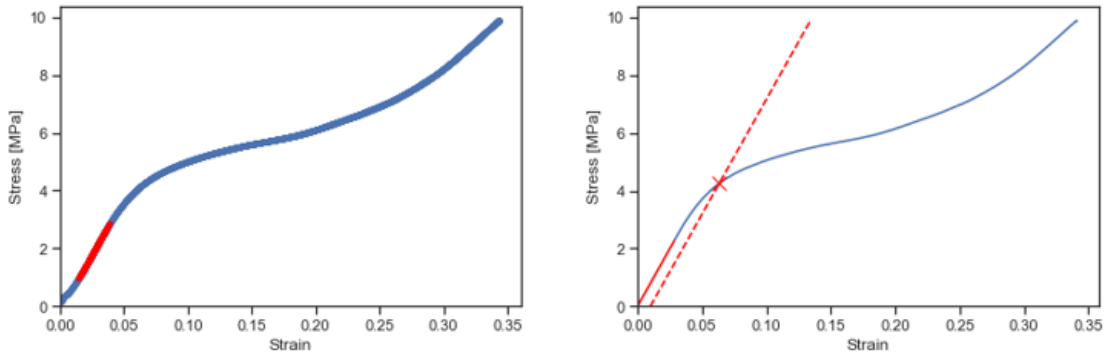

Figure 5-6 Automatic recognition of the linear segment and then the erase of the toe region and the start at the origin, furthermore, the slope is displaced in the x axis and the code report the interception as the yield point

5.3.4 Scaffold biological assessment

A heterogenic population of Human gingival mesenchymal stem cells (hGMSCs) were used [75], [76], which were acquired by previously reported methods with the approval of the Institutional Review Board of the University [77]–[80]. Primary cell cultures were kept in Dulbecco's Modified Eagle Medium (DMEM) supplemented with 10% Fetal bovine serum (FBS) and antibiotics (penicillin – streptomycin), in an incubator at 37 ◦C with 5% CO2 and 95% humidity. For biological assessment, PCL and PCL - 20% BG scaffolds were sterilized by ethanol 70% overnight, then, scaffolds were rinsed with sterile PBS 1× and left for 1 h in supplemented DMEM. Cell seeding was performed using agarose molds by previously reported methods [80], [81]. After reaching confluence, hGMSCs of passage 6 were trypsinized and counted in an automated cell counter Luna-II (Logos Biosystems, South Korea). For all experiments, 1 × 105 hGMSCs in 50 µl of supplemented DMEM were used to seed each scaffold inside the mold (n = 3) in a 24- well tissue culture plate. Together with 50 µl of supplemented DMEM without cells (n = 3 in scaffolds

under the same conditions), as well as 50 µl of cells seeded directly on the tissue culture plastic as negative and positive controls, respectively.

Cell adhesion efficiency Cell adhesion efficiency was evaluated by previously reported methods [80]. Briefly, 3 h after cell seeding, tissue culture plates were filled with supplemented DMEM and kept at standard conditions overnight. The next day, after removing the agarose molds, the scaffolds were transferred to a new 24-well tissue culture plate coated with agarose and rinsed with sterile PBS 1× to remove non-adherent cells [82]. Then, 1 ml of supplemented DMEM were added to each well, following by 200 µl of the reagent CellTiter 96® AQueous One Solution Cell Proliferation Assay (MTS, Promega) added to each well (and the controls) for 2 h at 37 ◦C. 200 µl of each supernatant was used to measure the optical density (OD) at 490 nm in a plate reader (Biotek 800 TS, USA). Cell adhesion efficiency is expressed in relation to the control (cells in well) [83].

Cell proliferation was evaluated based on the previous sections and reported methods [84]. The next day after cell seeding, the agarose molds were removed and the scaffolds were transferred to a new 48-well tissue culture and kept in standard cell culture conditions for up to 14 days, culture media was replaced every 2–3 days. For cell proliferation measurement in each time-point (3, 7 and 14 days), 500 µl of supplemented DMEM were added to each well (and the controls), following by 100 µl of the MTS for 2 h at 37 ◦C. 200 µl of each supernatant was used to measure the optical density (OD) at 490 nm

5.4 Results and discussion

5.4.1 Visual characterization (code, magnifier glass, SEM)

The inner structure was assessed by different measurements realized with the python and ImageJ code. To measure the pore size distribution on the inner structure of the scaffold with a non-destructive technique, images of each printed layer were analyzed, as delineated in Figure 5-4. The mean pore sizes — 0.37 mm (SD = 0.03), 0.38 mm (SD = 0.07) and 0.37 mm (SD = 0.04) for pure PCL, PCL-10 wt.% BG and PCL-20 wt.% BG respectively — were all less than the designed value of 0.4 mm. (Figure 5-7 A). There was a small but statistically significant negative correlation between the pore size and printed layer ($p < 0.0001$), (Figure 5-7 B). Thus, although the pore sizes for the first printed layer, as revealed by the intercept values of the linear regressions (PCL: 0.39 mm; PCL-10%BG 0.4 mm; PCL-20%BG 0.41 mm), were much closer to the designed value of

0.4 mm, there was a systematic decrease in pore size with each subsequent printed layer, which resulted in a smaller overall mean value compared to the designed pore size, indicating that differences between designed and experimental pore sizes may be due to a systematic bias rather than random error.

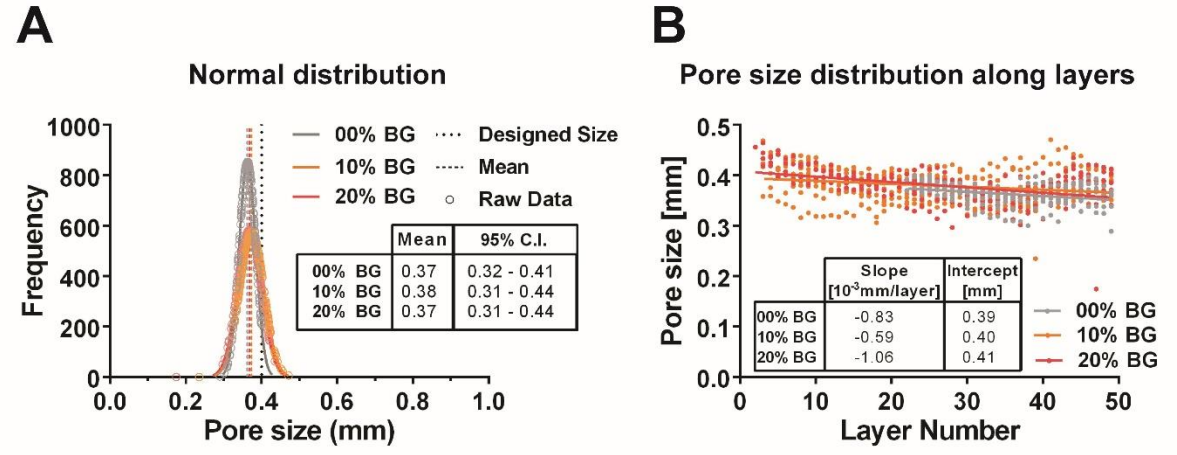

Figure 5-7 The fabricated scaffolds presented normal pore size distribution. (A) Normal distribution of pores along the scaffolds with the corresponding frequency for each recorder value. Raw data points correspond to the average value per layer (nlayer =30 pores; nspecimen = 1470 pores). Inserted table shows the mean value and 95% confidence interval (C.I.) for each compound. (B) Distribution of the averages pore size values per layer along the scaffold, linear interpolation showed as a line and inserted table the intercept with y-axis and the statistically significant slope for each condition.

Figure 5-8 shows the distribution for 0% BG samples. Scaffolds as with BG present a negative vias, in this case a no clear difference between the different compounding methods was found, neither with the printing temperature. Future work needs to address this evaluation with better statistical tools aiming for a better understanding of the relation layer-pore size.

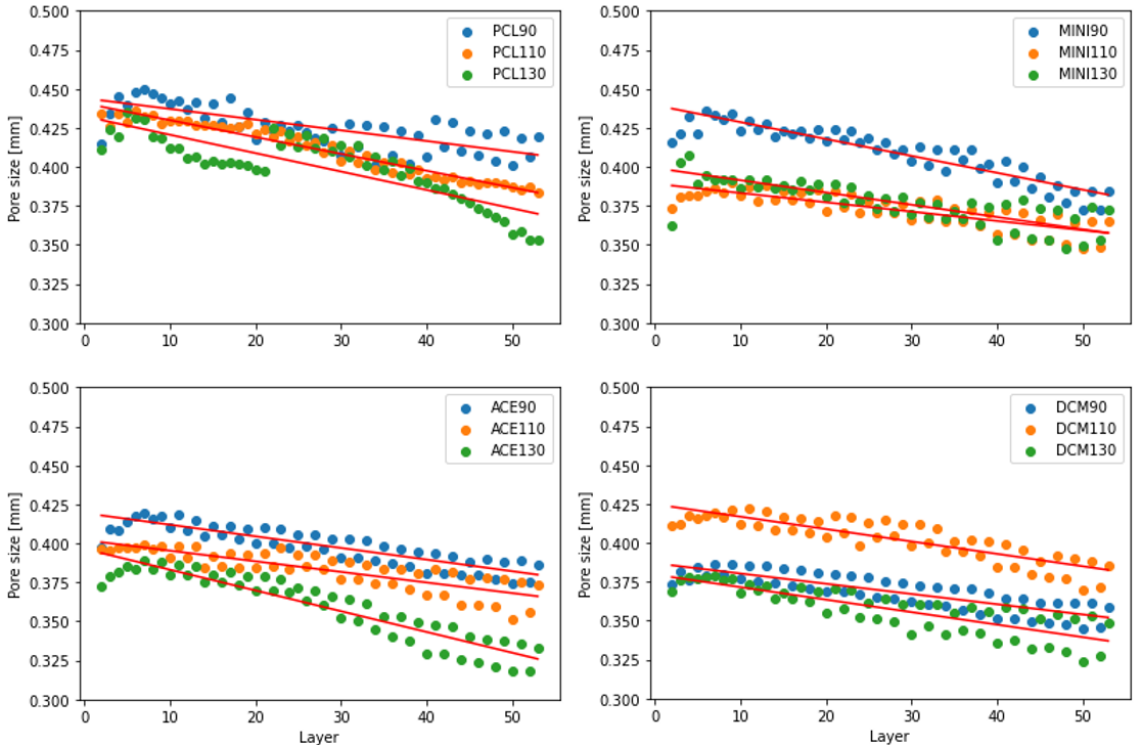

Figure 5-8 The fabricated scaffold presents a negative vias for the different compound methods and printing temperature.

Furthermore, Figure 5-9 show the frequency of the acquires values. The code grouped the repetitions for each method and temperature and showed then in a normal distribution. In the figure can be appreciated how some samples present a high frequency, meaning a low variability in the printing process, values of 3000 pores with the same length are shown. This provide information to understand which method is less controlled and have more fluctuation, as well, if the average of it is not close to the desire pore size. In this case, a change of the printing parameters is needed. For the methods with low frequency a more assisted 3D printing process is required where minor changes on the parameters will be needed over time.

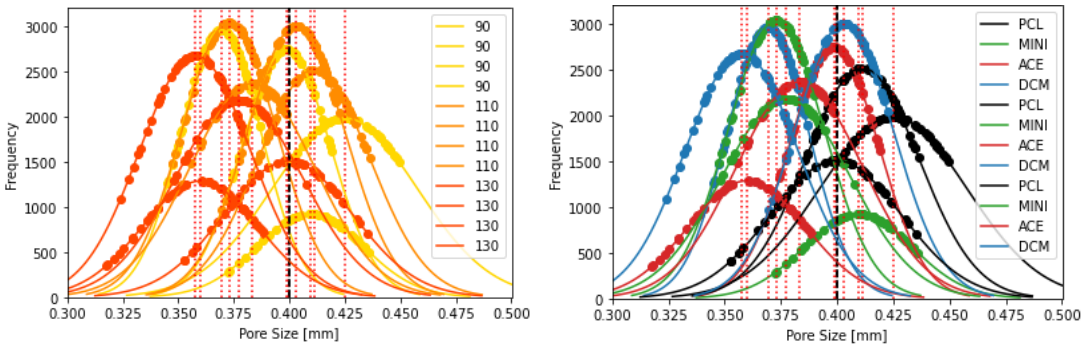

Figure 5-9 Custom-made code showing the pore size measurement and the frequency of the value of the different compounding methods and printed temperature in a normal distribution. Dash line represent the average for each curve and the black dash line the desire value of 0.400 [mm]. Graph of the left represent the temperatures and the right the compounding method. Both have the same values but different labels/legend.

To assess the fidelity of the fabrication process to achieve the desired geometry, SEM micrographs were obtained, which showed homogeneous distribution of struts and shaped geometry (Figure 5-10). Furthermore, Figure 5-10 C show the microporosity of the scaffolds where the white dots represent the homogeneous distributed BG along the strut. Nevertheless, the cross section of the filament show how in some sectors agglomeration of BG can be evidence.

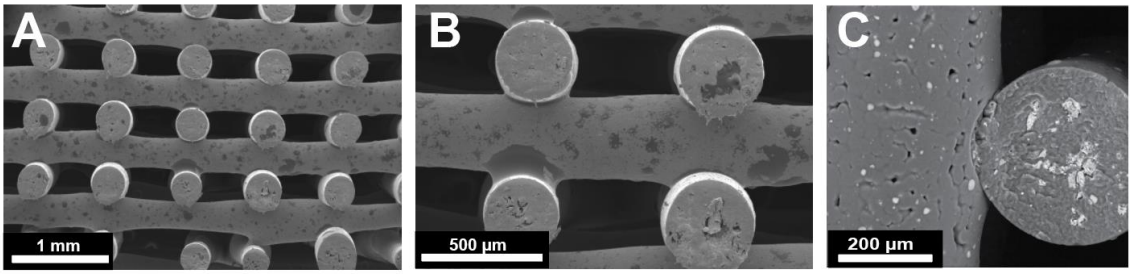

Figure 5-10 The fabricated scaffolds presented optimal microarchitectural properties and a homogeneous distribution of BG particles. (A-C) SEM micrographs of representative scaffolds. (B) Magnification of (A) that shows the space between struts of a 0% BG sample. (C) Magnification of a segment of a 20% BG sample that shows the junction between each strut and the BG distribution.

The effect of deformation of the first layer due to the printed bed can be evidence with magnifier glass. Pictures were taken both on top and bottom part of each sample and measurement were realized. Both, manual measurement, and the python code were used to measure the different

distance of certain samples. Figure 5-11 A correspond to a diagram that represent how the first layer is over deformed by the printing bed, with Figure 5-11 B an acquired picture of the bottom of a sample can be evidence the flat shape of the base and bigger size of struts over pores. Moreover, the code was run on several sample and Figure 5-11 C show the information for PCL-DCM. Being the crosses the measured pores in the magnifier glass pictures, can be appreciated how to first layer have a big deviation with the third layer, nevertheless, the last layer match with the acquired top picture. Usually in the literature the magnifier glass pores are used and average to represent the whole sample pore size. Now with this information this can be put on doubt where is represented how the first layer is considerable deform and not represent the inner bias of the sample.

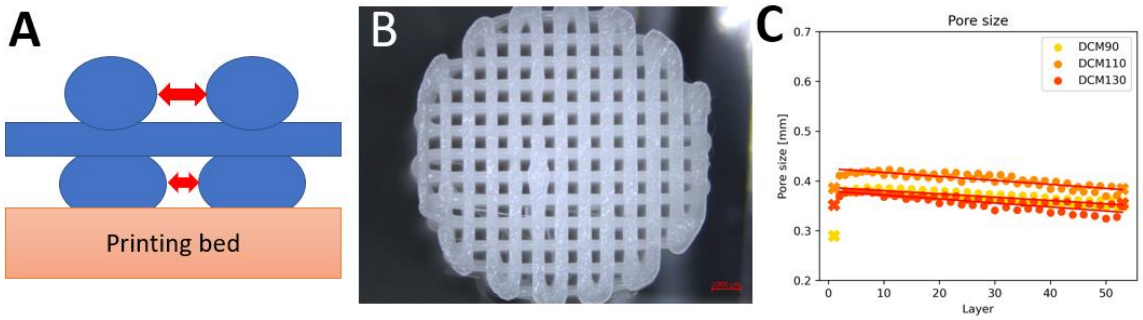

Figure 5-11 First layer analysis with (A) the model of the first layers, (B) a magnifier glass picture of the first layer and (C) a graph showing the pore size distribution for the different layers, with the crosses the values from top and bottom layer and the dots the one of the inner architecture.

The same pore size can have different geometry. As mentioned before, the printed struts once deposited can flow and lose their shape if the cooling system is not the adequate. Nevertheless, a strong cooling system can be too fast avoiding both layers to bind and thus reducing the mechanical properties of the sample. An equilibrium between both needs to be found and apply to the sample. The python scripts allow to measure a parameter related with the dispersion of the strut, the circularity, this parameter is based on the relation between the area and the perimeter of the sample. Having low circularity mean a sharper structure with a better define pore. Scaffolds are compared with a circularity of 0.785 that correspond to a square. The samples exhibit a value close to the desire one and far away from other geometries as a circle (Figure 5-12), however, a small trend can be evidence when looking to the detail of the pore. Figure 5-12 show how the initial pores show a squared shape but as the number of layers increase, they converge into a

plateau at a circularity of 0.810. This effect is evidence at the first 10 layers were the circularity evidence a change on the geometry of the pore. The influence of the fans can be directly correlate with this phenomenon, having the cooling system pointing to the base of the sample, the first 10 layers suffer a stronger influence by the fans which is reduce and homogenize from the 10th layer. A closer view to the layers on the platoon can be evidence that the borders of the square are the one that have a rounded shape rather than sharp edges. This effect is beneficial for the sample as this point is where the layers bond together and an increase of volume means more interaction between both struts. Figure 5-13 shows an image where a red line represents the temperature influence, corners lose they sharpness and become more circular by the poor temperature control. This effect increase with higher temperatures, printing at a higher temperature gives more time to the material to flow as the fan setup remains constant for the different printing temperatures.

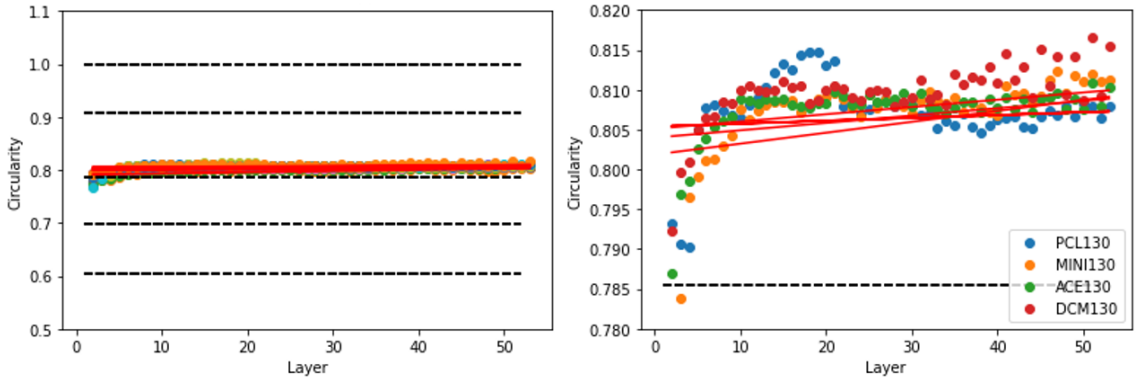

Figure 5-12 Left graph represent the circularity of the samples for the different compounding methods, having a value near the desire one (0.785). The right one shows a closer range of interest where a clear slope can be evidence for the first layers to a later platoon. Representative information corresponds to a print temperature of 130 °C where the effect is strong.

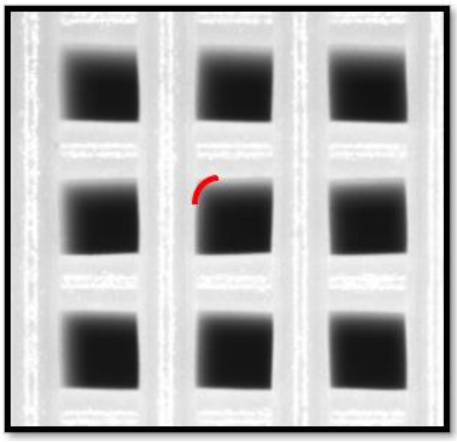

Figure 5-13 Representation of circular pores, the effect is minimum but can be accountable.

The printed scaffolds exhibit low percentage of printed errors. For each compounding method and temperature, the number of invalid pores was measured and the percentage of those with respect to the total analyze pores was reported. Figure 5-14 show the percentage of invalid pores for each material and printed temperature, displaying that there is not a clear trend between the printed temperatures. Nevertheless, different compounding materials exhibit different reaction to the printed temperature with mechanical compounding (MiniLab) the one with highest deviation. Both, PCL, and PCL-ACE present a similar deviation but with different reaction to the temperature. Finally, PCL-DCM correspond to the technique with the less deviation in terms of invalid pores. The actual code has a strict set up with respect to invalid pores, this is one of the reasons for the high percentage of invalid pores. Minor changes in the minimum circularity required to be a pore considerable change the number of valid pores. This change was made in order to analyze and improve the printing process in a way that not squared pores are not the pores that we are aiming for and thus they are invalid.

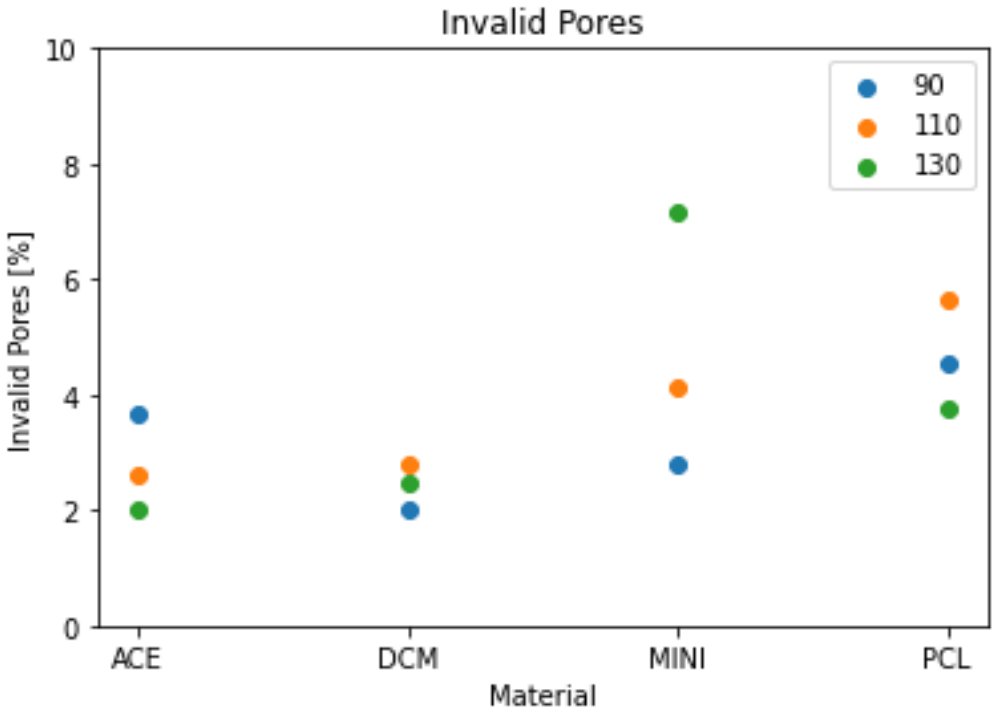

Figure 5-14 Invalid pores for the different compounding methods and extrusion temperatures.

5.4.2 Overall characterization

Scaffolds porosity was assessed by Archimedes method. The overall porosity was close to their designed porosity of 50% (PCL: $\bar{x}$ =46.94%, SD = 1.61; PCL-10 wt. %BG: $\bar{x}$ = 48.29%, SD = 5.95; and PCL-20 wt. % BG: $\bar{x}$ =50.87%, SD = 2.45. Figure 5-15). One-way ANOVA revealed no statistically significant differences between the three inks, nor with the theoretical value (50%).

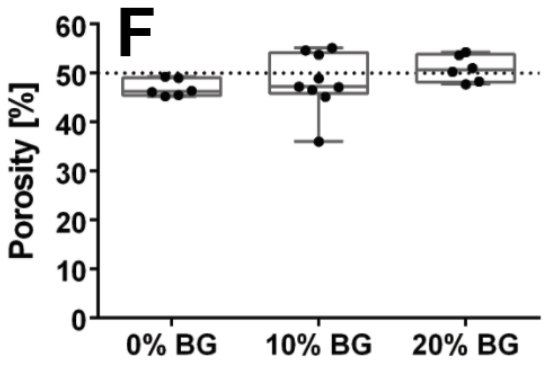

Figure 5-15 Porosity measurement of all the samples: boxes enclose the first and third quartile and whiskers shows the extreme values, and the dots represent all measured values. The dotted line represents the designed porosity.

For scaffolds without BG an additional comparison was realized, the custom code used the strut diameter to extrapolate the inner porosity of each layer. Figure 5-16 compare the average porosity generated by the pictures for each layer with the experimental acquired porosity. A dash line represents a perfect match between both values, which show a small mismatch with the actual correlation. This gap is due to a series of factors. First, the code approximates the volume and sub estimates the material on the intersection of adjacent layers, reducing the total measured material. Second, the code skips the first and second printed layer as the contrast with the background (printing bed) is low generating a considerable error. These layers, specially the first one, are flattens with respect to the others, having these a lower porosity value. Third, the code measures the inner structure of the sample, avoiding the extra material deposited on the border due to the continuous strand configuration. The circumference of the scaffold accumulates extra material generated by printing errors and the loose of certain pores on the border.

Nevertheless, with all this misalignment still possible to correlate this error and predict how much is going to be the porosity of the sample, avoiding extra experiments that induce the transformation of the sample. Moreover, this allows to have a measurement of the inner porosity by layer, a crucial value for samples with different inner porosity as gradient scaffolds.

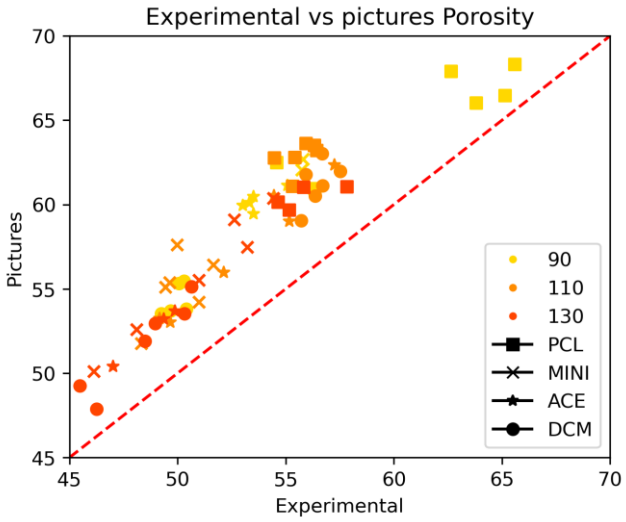

Figure 5-16 comparison between experimental porosity and pictures acquire one. Dash line represent a perfect match.

Previous work have also compare the relation between the design porosity and the experimental one, A previous investigation of 3D printed samples with a commercial 3D printed and how the variation of porosity and pore size affect the mechanical behavior of the samples, showed that

small pore size induce a higher challenge to control the porosity, having this a bigger deviation with the design one. Vallejos *et al.* [40] used the same process following Archimedes method, where designed porosities have considerable difference with the designed one for small pores, on the other hand, big pores present a similar porosity with the design (Figure 5-17 B).

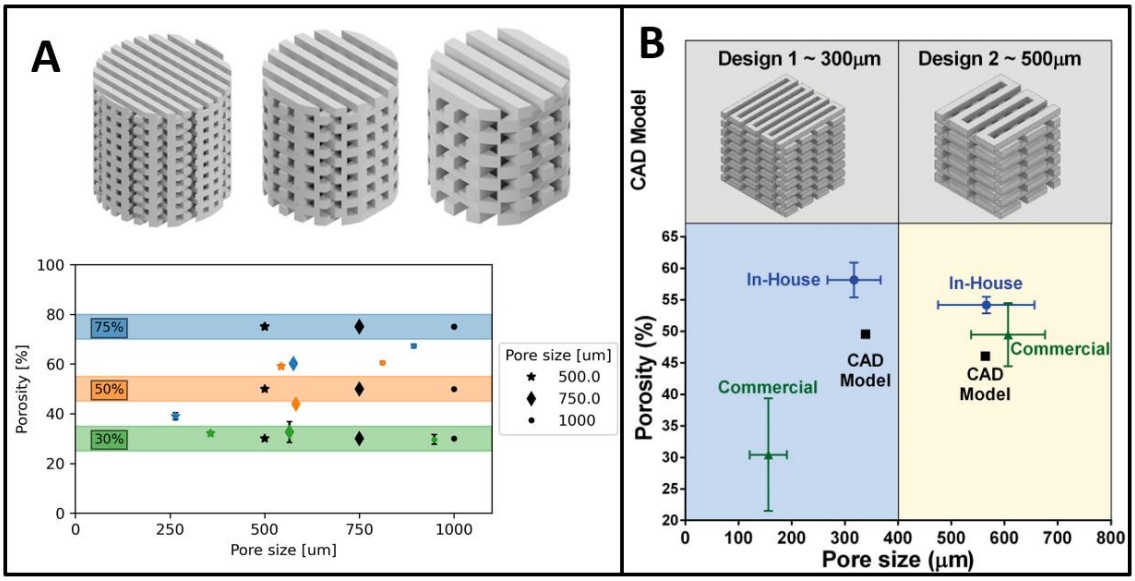

Figure 5-17 (A) shows CAD representative models and the pore size-porosity relation for the printed samples. As well, (B) shows the pore size and the relation of pore size and porosity with the CAD model [40]**.**

Micro-CT was used to both analyze the overall microarchitecture, as well as the BG particles distribution. The scan confirms previous results where the inner structure is close to the theoretical model of the scaffolds with a well-defined shape and regular structure. Moreover, the BG distribution is homogeneously distributed along the whole sample, showing some minor agglomerations of the material (Figure 5-18).

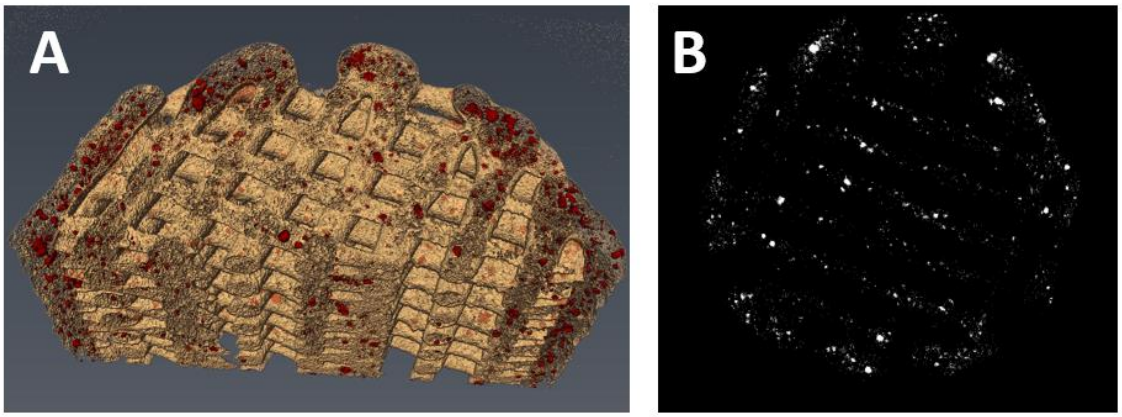

Figure 5-18 (A) micro-CT image of a representative PCL – 20% BG scaffold [See supplemental materials for an animated video (MicroCT.mpg) of the micro-CT scan]. (B) Micro-CT image that shows the distribution of BG particles on a layer as white dots.

Finally, a clear example for the importance of a control temperature set up is Figure 5-19, where the same printed sample was expose just for one side to a fan that control the sample temperature. The figure shows a clear difference in quality for both faces, having a homogeneous shape the one with the fan set up.

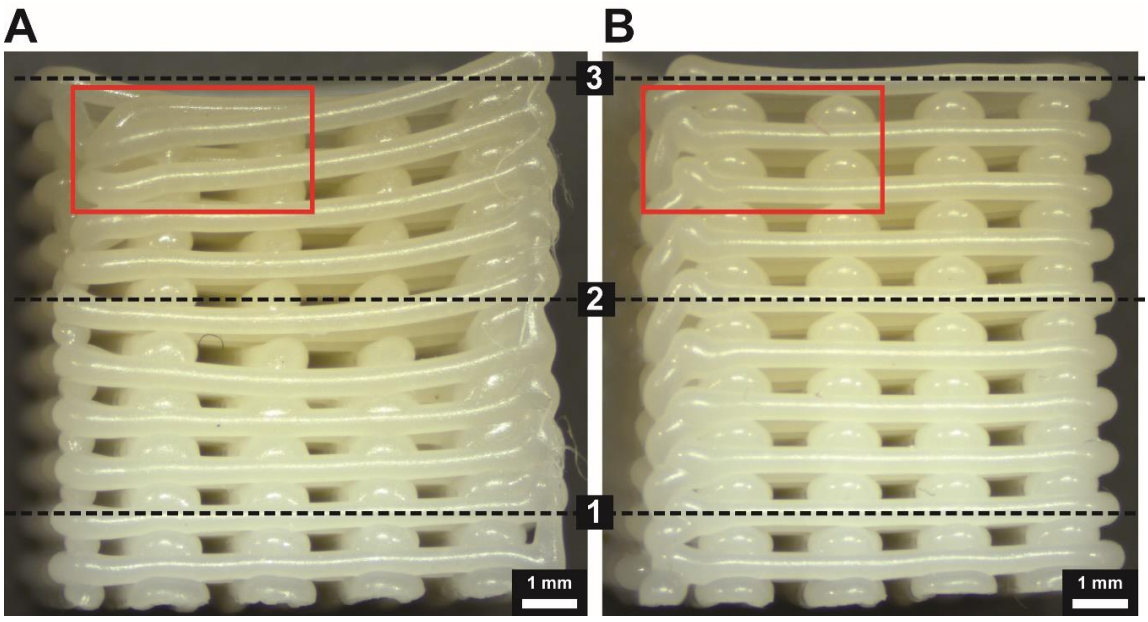

Figure 5-19 Printed scaffold with forced convection for better temperature diffusion (A) Printed scaffold face without forced convection and (B) with forced convection. Dotted lines represent average height of indicated layers and ROI the principal failure. Both images correspond to the same scaffold but opposite faces.

5.4.3 Scaffold mechanical properties

To test effects of the addition of BG to the scaffolds in their mechanical properties, compression testing was performed (Figure 5-20 A-B). The addition of BG decreased the stiffness, strength, and deformation energy in a proportional way (Figure 5-20 C), presenting a statistically significant lower Elastic Modulus than the PCL specimens (Figure 5-20 D), while the 20% BG scaffold also presented a significantly lower Yield Stress (Figure 5-20 E).

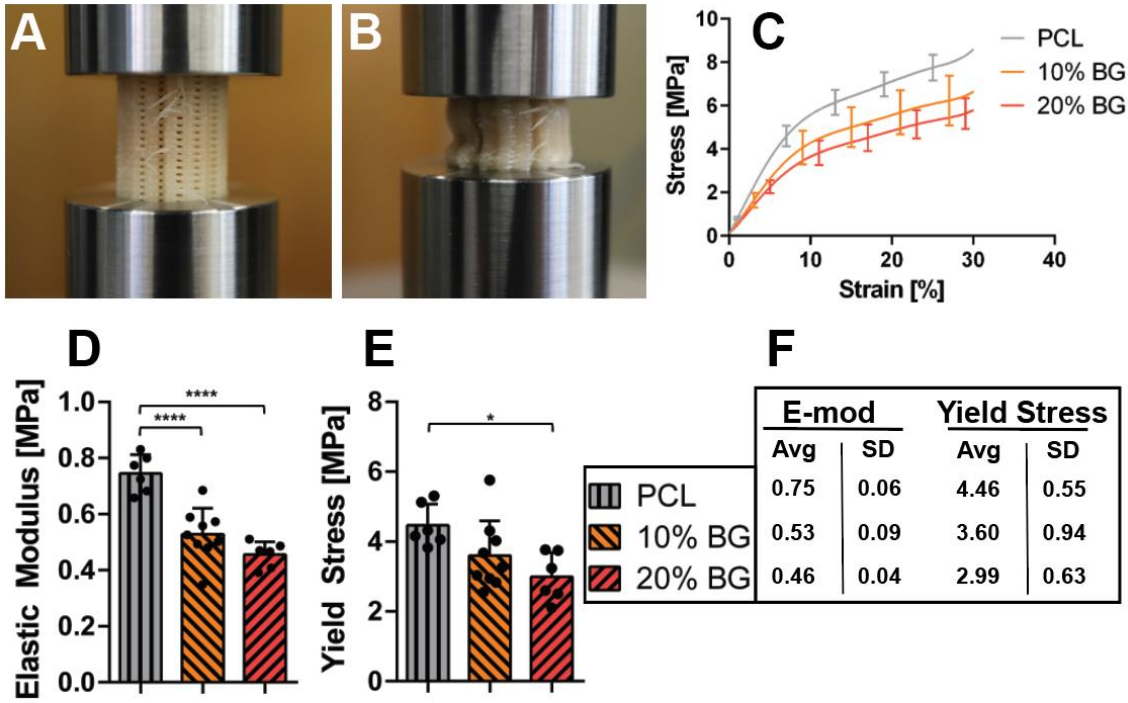

Figure 5-20 The PCL – BG scaffolds show lower mechanical properties than the control. (A) Representative image of a composite scaffold of 20% BG before compressive testing. (B) Representative image of a composite scaffold of 20% BG after compressive testing. (C) Stress-Strain curve for the scaffolds, error bars represent the standard deviation. (D) Elastic Modulus of the scaffolds. (E) Yield Stress of the scaffolds. In (D-E), bars represent the mean with the SD in all cases, brackets represent statistical significance in a post-hoc Tukey test after a one-way ANOVA (* = p < 0.05, ** = p < 0.01, *** = p < 0.001, **** = p < 0.0001). Table (F) shows the average (Avg) and SD for the dots of the experimental values of (D) and (E).

The effect of the compounding method and the printing temperature did not show a clear trend. PCL samples have a similar mechanical behavior showing not a clear relation with respect to the

compounding nor the printed temperature. Figure 5-21 show the average for each condition with a 95% confidence interval.

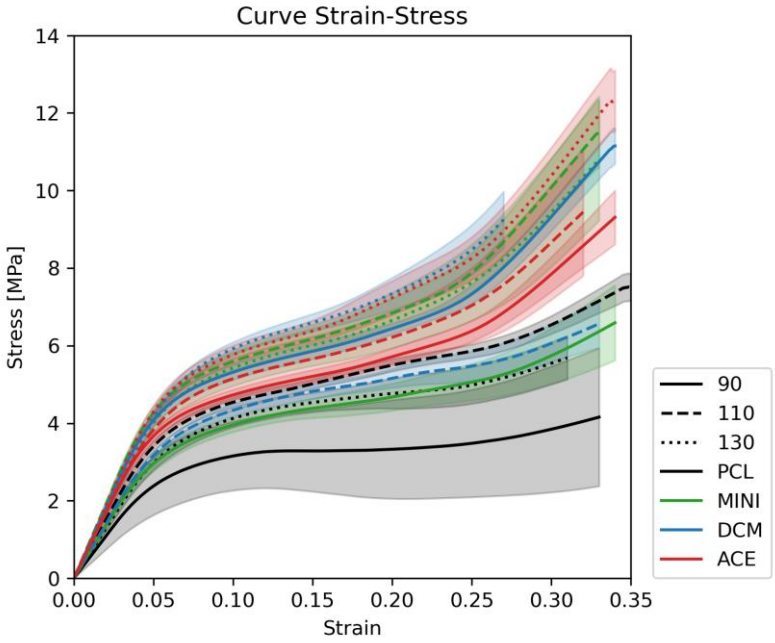

Figure 5-21 Strain-Stress curve for the average of the different compounding methods. Colors represent method and type of line the printed temperature. Color bands the 95% confidential interval.

On the other hand, yield strain shows a consistent value for all tests. As expected, yield strain is driven by the geometry and not the material, however, the yield stress change with respect to the material procedure. Figure 5-22 represent the yield point of all the mechanical test with a cross.

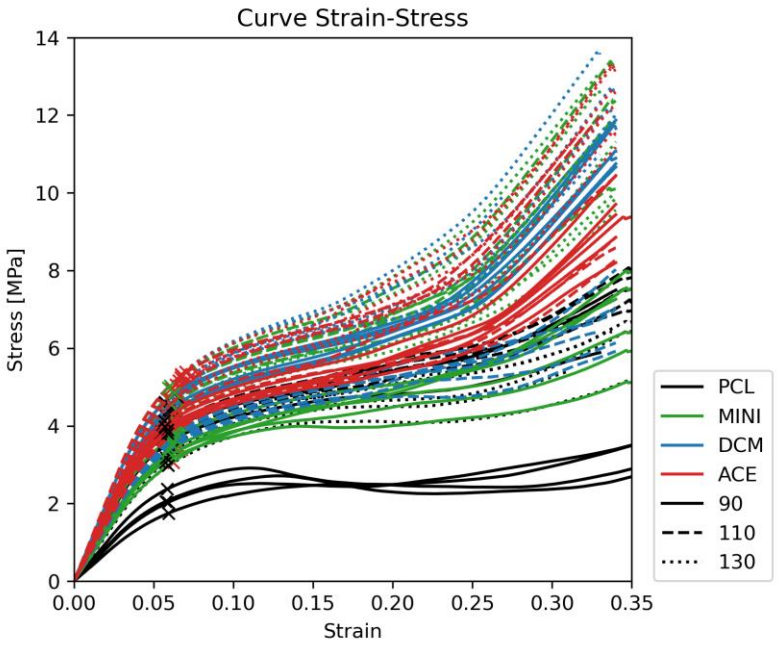

Figure 5-22 Strain-Stress curve showing the yield point for each sample. Colors represent the used method and lines the print temperature. Crosses shows the yield point.

Figure 5-21 is grouped by material generating Figure 5-23 where can be evidence that different materials follow a different response to the printed temperature. This is also evident when graphing the apparent elastic modulus versus porosity, where is evidence that an additional process is needed as the porosity is the mayor driver for the apparent elastic modulus. Figure 5-24 show this clear trend as is described in the literature, were a bigger porosity means a lowers elastic modulus.

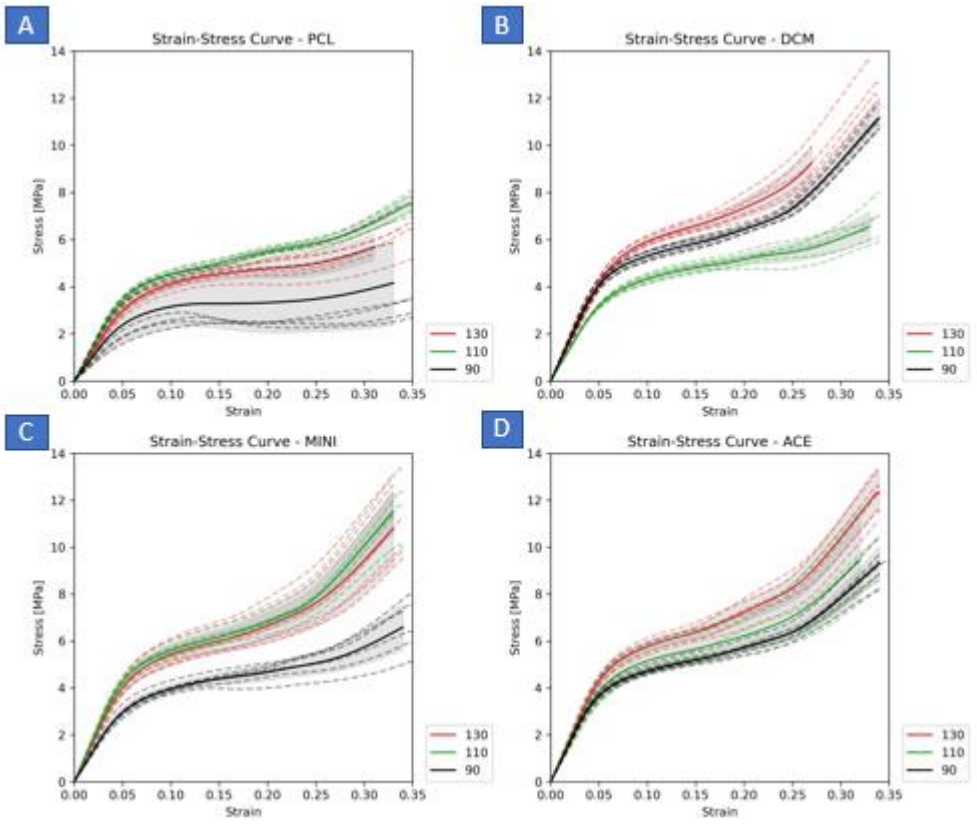

Figure 5-23 Strain-Stress curve grouped for the different method. Straight line represents the average and dashed line each repetition. The color bands a 95% confidential interval. Colors show the print temperature.

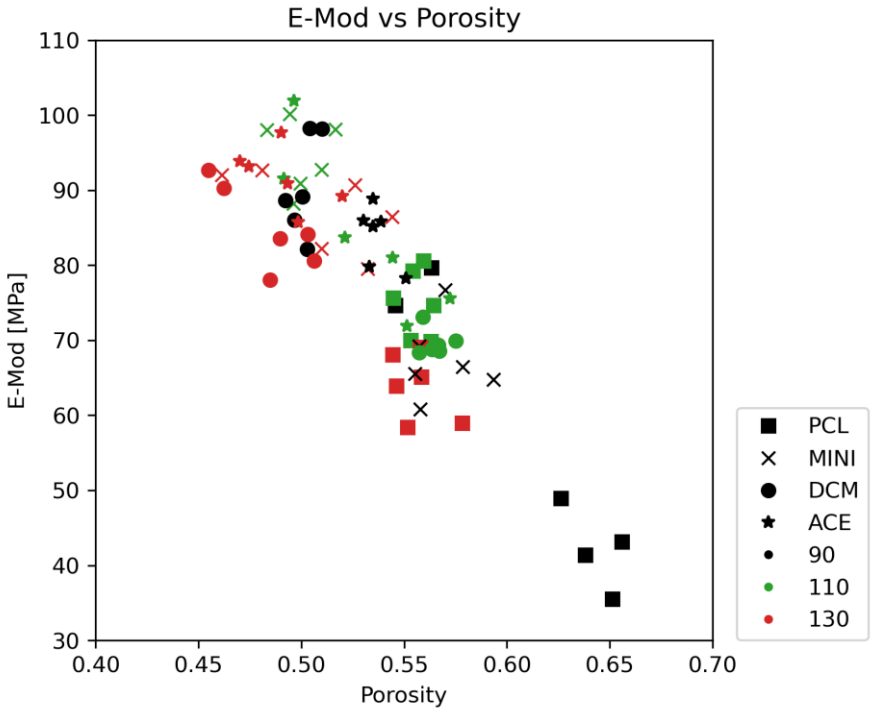

Figure 5-24 Relation between the porosity and the elastic modulus. Symbols show the different methods and the color the print temperature.

5.4.4 Biological testing

To assess the biological properties of a high dose of BG in the PCL scaffolds, both the PCL control and the PCL – 20% BG scaffolds were used to measure both cell adhesion efficiency and cell proliferation with hGMSCs. The results show that cell adhesion efficiency is similar between both groups, with an average value close to 40% of the control (mean value of 37.56% for the PCL scaffold with SD = 12.44, and mean value of 40.51% for the PCL - 20% BG scaffold with SD = 18.02) (Figure 5-25 A). Regarding cell proliferation, after 7 days in culture conditions, the PCL – 20% BG scaffold showed a significant increase in comparison with the control, however, after 14 days in culture conditions, it showed a significant decrease in comparison with the control (Figure 5-25 B).

For future work is needed to increase the number of repetitions per group as to capture a SEM of the samples to glimpse the phenomenon on day 14. An initial guest corresponds to the differentiation of the cells and thus the reduce proliferation. In any case more tests are needed, and different procedure will be do have a better understanding of cells and BG.

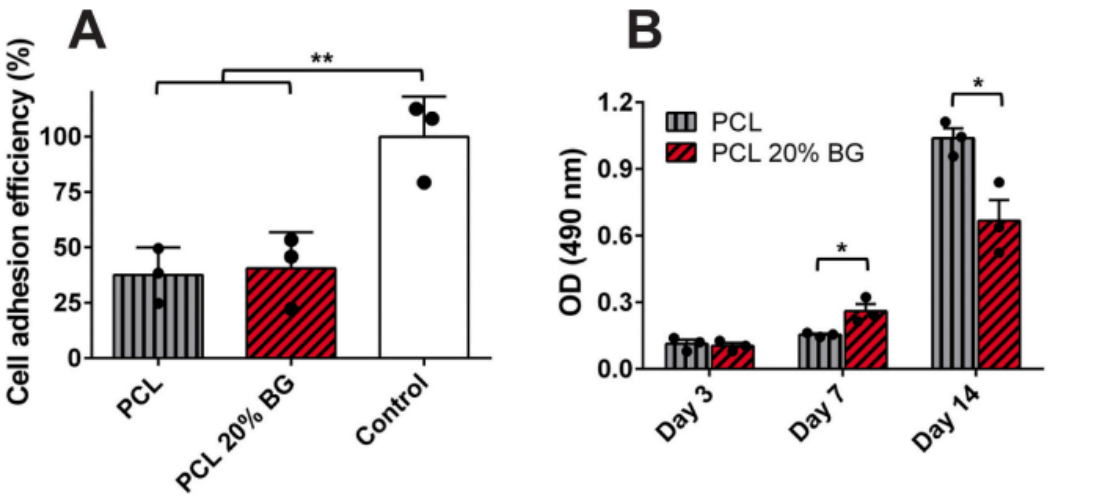

C

	Cell. Adh. Eff (%)	
	Avg	SD
PCL	37.56	10.15
20% BG	40.51	10.30
Control	100.00	14.72

D

	OD (490 nm)					
	Day 3		Day 7		Day 14	
	Avg	SD	Avg	SD	Avg	SD
PCL	0.11	0.03	0.15	0.01	1.04	0.06
20% BG	0.10	0.02	0.26	0.05	0.67	0.13

Figure 5-25 PCL 20% BG scaffolds influence cell proliferation, while showing similar cell adhesion efficiency with their PCL controls. (A) Cell adhesion efficiency experiment between PCL and PCL 20% BG scaffolds. (B) Cell proliferation between the same conditions after 3, 7 and 14 days. Bars represent the mean with the SD in all cases. In (A), brackets represent statistical significance in a post-hoc Tukey test after a one-way ANOVA, in (B), brackets represent statistical significance in a t-test for each day (* = p < 0.05, ** = p < 0.01, *** = p < 0.001, **** = p < 0.0001). Tables (C) and (D) represent the average (Avg) and SD for the values in (A) and (B).

5.4.5 Inferences

- The additional fan set up fulfill the requirements for high temperature extrusion. With a notable difference between the regular 3D printing and the one with force convection. Reducing the printing time, the cost associated and increasing the quality of the print sample. The fan set up have a low cost of <50 € and does not require a software to be used. This is specially important for relevant size structures.
- The use of an insitu code provide additional information to take fast and precise actions while printing. The reiterative measurements of print strut provide a guide for small adjudgments while printing in order to keep and improve the desire shape. Furthermore, in case of a big failure, the pictures will confirm that the printing process needs to be stop and no additional time or material is wasted.

- The custom-made code gives additional information to understand the inner geometry of the scaffold, analyzing enough information to provide numbers to classify the different print structures. The code will help others to understand better their print process and annex the pore size, porosity, and circularity to other scaffolds properties like mechanical performance or biological behavior.
- The custom-made code revels that the approach of upper- and lower-layers pores is not representative of the inner architecture. This is a common approach in literature to represent the pore size of the geometries. The code will provide a new tool to address this issue in a proper way.
- Inner architecture presents a negative bias of pore size due to a series of factors. One of the reasons could be the presence of accumulate heat or the gathering of small errors during the deposition of layers.
- The circularity also shows a similar phenomenon, where the use of an external fan setup defines the interaction between layers. This needs to be addressed in further investigation but a clear trend is shown between the sharpness of the pore and the speed of colling of the layer.
- Porosity was achieved for BG samples. For the case of different compounding methods, a bigger distribution was found as the change of temperatures were a challenge factor. These, mostly in an acceptable range, were successfully predicted by the code, which calculate the inner porosity of the sample based on the acquires pictures. Avoiding a posterior experiment and the possibility on affecting the properties of the scaffold.
- Mechanical characterization suggests that the addition of BG to the scaffolds reduce their mechanical properties, this is attributed to the poor binding between the matrix material and the big BG particles, another considered option is that the DCM acts as a plasticize reducing the mechanical behavior of the material. A better statistical analysis needs to be realized to fully understand this phenomenon and the relation between the mechanical properties and the other measures factor. A prior analysis shows the direct relation between the Elastic Modulus and the porosity. For the different compounds a series of factors take into action and thus a proper conclusion cannot be taken with the actual analysis.
- Biological characterization showed that the presence of BG has a positive impact on the first week but a negative on the second one. This could be to a series of reasons like, start of differentiation of cells, agglomeration of toxic residues, the use of DCM between others. In any case, a bigger study needs to be realized in order to represent in a proper way the scaffolds in a biological environment.
- The code let us know that the literature follows a wrong procedure
- The samples have a negative bias of pore size
- The BG is homogeneously distributed along the sample, but agglomerated in sectors
- The porosity is the one desired
- BG decrease the mechanical properties as not expected
- Different compounding methods does not show a significant change in mechanical properties, are more driven by porosity
- Biological results show how the BG is positive at the first week but negative at the second, a bigger experiment is needed.

The good achieve quality was due to the complete understanding of the printing process and their needs, this was accomplished by preliminary studies in rheology. The next chapter will detail the methods and results of this process and how to annex the 3D printing and the rheological characterization.

5.5 Chapter Summary

Scaffolds were assessed with different methodologies. A less invasive technique was applied compared with the literature. The custom-made python script effectively represents the inner structure of the scaffold by a non-invasive method. The comparation with the literature method showed that exposed layers fail to represent the inner structure of a printed scaffold. Additionally, microCT also verify the integrity of the scaffolds and their inner structure, showing good inner quality and homogeneous BG distribution along the sample. Porosity characterization shows a close value to the designed one for BG samples, on the other hand, no BG samples showed a bigger distribution. The custom-made code effectively predicts the experimental porosity using as an input the bioplotter images. The samples were also characterized by their mechanical properties by a compression test. Results suggest that the addition of BG particles decrease the mechanical properties. For the method comparation a deeper work needs to be done to fully understand the results. Finally biological results show how the BG have a better performance on the first week but decrease with respect to the control on the second week.

CHAPTER 6: RHEOLOGICAL ANALYSIS

This chapter discusses the materials and methods used to study the rheological behavior of the compounds and the extrusion temperatures using during the scaffold fabrication (SCAFFOLD FABRICATION). The experimental methodology (Section 5.4) details the rheological tests carried out, followed by the results and inferences discussed in Section 5.5.

5.1 Introduction

This chapter addresses the specific aim 3 defined in Section 3.2 of CHAPTER 3:. The main goal of this study is to determine the rheological characteristics of the compounds at different shear rates and shear stresses over time. The properties will be used to correlate the rheological properties with the process parameters used in the 3D printing.

The Chapter first gives a virtuous explanation about rheology and the different ways to measure it, then the methods used in this study are presented along with the strategic used to connect the rheology with the 3D printing. Results are expose and discussed, finishing with a conclusion of the chapter. The understanding of rheology is mostly based in the amazing guide A Basic Introduction to Rheology of Liepsch [85].

5.2 Understanding of Rheology

Rheology is whenever a material flow, change or move, explaining materials flow behavior and deformation. The essential elements of rheology for a material are mainly three [85]:

- Inner structure, link between the molecules of the material, this will flow easier if there is space between its molecules, but if the link is tightly, they will stick together even if the material is deformed.

- Outsides forces, any force apply to the material, these could deform or make it flow and can be execute at different times/speed. E.g., pushed, pulled apart, wiped, or naturally pulled to earth by gravity.

- Ambient conditions, the situation the material is in when it is stressed, being the temperature one of the mayor factors.

The essential property of a material corresponds to the viscosity, which explain the thickened or the internal flow resistance of it. This can be scientifically determined by a two-plates model

(Figure 6-1**Error! Reference source not found.**), where a viscous material is struck between two plates with the lower one still and the upper plate slowly moves along, this will cause a laminar flow, also call shear flow, in the material. This model allows to formulate the two most important variables, shear stress and shear rate. A movement on the upper plate will generate a parallel stress to the liquid surface, a force (F) [N] divided by area (A) [m^2] will generate a stress that define how much energy is applied to the material and is denominated Shear Stress (τ) [Pa] (Equation 6-1). On the other hand, this stress will have a certain speed, the speed (V) [m/s] divided by the distance (H) [m] between the plates describes the Shear Rate ($\dot{\gamma}$) [s^{-1}] (Equation 6-2).

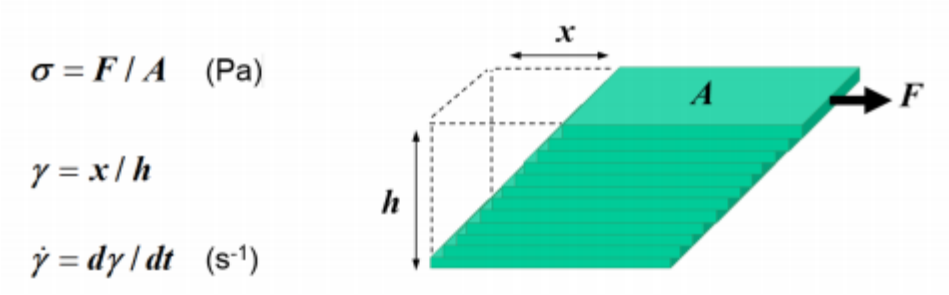

Figure 6-1 Two-plates model for the quantification of shear rate and shear stress for layers of fluid sliding over one another [85]**.**

$$\boldsymbol{\tau = F/A} \qquad \text{Equation 6-1}$$

$$\boldsymbol{\dot{\gamma} = V/H} \qquad \text{Equation 6-2}$$

Having the upper layer, in the model, the maximum velocity, there is a momentum transference between the inner layers of the fluid by interactions and collisions until the lower layer, which velocity is cero (stay still). This resistance that generates a reduction in the fluid velocity and kinetic energy is defined as viscosity (η) [Pa*s], making it the coefficient of proportionality between the shear stress and the shear rate (Equation 6-3).

$$\eta = \tau/\dot{\gamma} \qquad \text{Equation 6-3}$$

There are some liquids that does not shown a relation between the change of shear stress or shear strain, hence, the relation between them is linear and the viscosity is invariable with shear stress

or shear rate, these fluids are denominated Newtonian fluids. Nevertheless, generally fluids are non-Newtonian where the viscosity is varies as function of the applied shear stress or shear rate.

It should be noted that fluid viscosity is affected by pressure and temperature (mainly temperature), as a slight change on temperature has a big impact on the viscosity, e.g., a decrease of 1 °C on the temperature can increase the viscosity a 10% [85]. Additionally, non-Newtonian liquids are subjected to time-dependent structure changes when they flow, making necessary to always take in consideration time and temperature of the experiments when measure viscosity.

To accurately measure these variables, the rheological properties of the samples detailed in this study were assessed by measurements carried out in an Anton Paar MCR 301 rheometer (Austria) (Figure X). The rheometer consists of a servo motor that rotates at a certain speed. This motor moves a geometry that consist of a cylindrical plate-to-plate geometry, following ISO XX. The geometry is composed by a rod which has the upper end attach to the motor and the plate on the lower one. The geometries and its dimensions are presented in Figure 6-2.

Figure 6-2 Anton Paar MCR 301 rheometer at EMPA.

The rheometer applies a current to the motor which transforms it into a torque, continuously, this force rotates the system at a certain measure speed. Moreover, this torque can be translate into a force (F) that acting over the surface area (A) of the plate gives the shear stress (Figure 6-3), on the other hand, the shear rate is defined by the gap (H) between the plates and the velocity of the system, which is determined by the angular velocity (ω), accurately measure by high precision position sensors, and the plate radius, since the velocity is equal to the radius times angular velocity (Equation 6-4) (Figure 6-3). Rheological experiments are driven by these two variables. Experiments either apply a shear stress and measure the shear strain generated, or a certain shear rate is defined, and the shear stress needed to achieve it is measure.

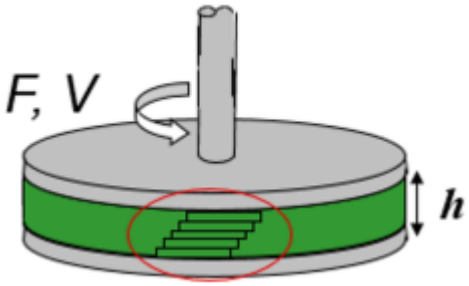

Figure 6-3 Illustration showing a sample loaded between parallel plates and shear profile generated across the gap [85]**.**

$$V = r * \omega \qquad \text{Equation 6-4}$$

Additionally, the rheometer has the ability to change the temperature of the sample by an external temperature control system. This temperature can range from -150 to 1000 °C and is apply by an external environment set up surrounding the sample (Figure 6-4 Model of rheometer with the heating hood **[86]**.Figure 6-4).

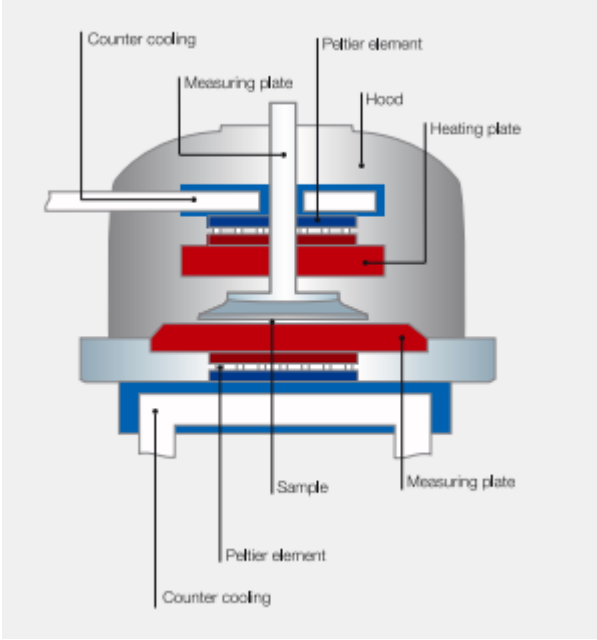

Figure 6-4 Model of rheometer with the heating hood [86]**.**

Finally, rheology experiments are divided mainly into two types, rotational and oscillatory. Rotational experiments focus on the change of viscosity and are principally done for viscoelastic

liquids, on the other hand, viscoelastic solids are subject to oscillatory experiments that describe the elastic and liquid part of the material.

5.2.1 Rotational rheology

A rotational experiment consists in the rotation of a plate that increase the deformation of the sample over time. Usually are driven by an increment of shear rate. This test aim to describe the viscosity of the sample and the behavior of it with respect to the change of shear rate, shear stress, time, or temperature.

The most common type of non-Newtonian behavior is shear thinning, in which the viscosity of the fluid decrease with the increasing of shear. Shear thinning correspond to the micro-structural rearrangement happening at the plane of the applied shear and is common in dispersions, including emulsions and suspensions, as well as polymer solutions (Figure 6-5).

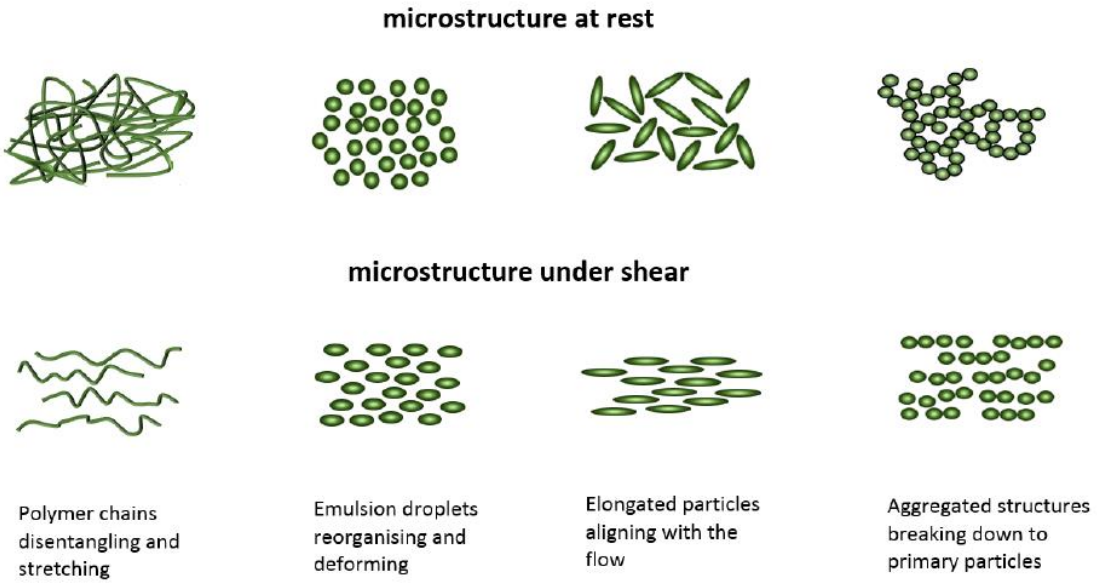

Figure 6-5 Illustration showing different microstructures in response to the application of shear [85]**.**

At low shear the material behaves at rest, maintaining an irregular order resulting from particles and molecular interactions and the restorative effect of Brownian motion [85]. In some materials, mostly very highly shear-thinning fluids, this order needs to be broken by executing a certain stress on the sample, this stress is denominated yield stress and correspond to the critical shear rate or shear stress were a material in rest start to flow. Before this point, the material is defined as a solid, hence with infinite viscosity at rest. Nevertheless, many groups prefer to describe this point as

"apparent yield stress" as at very low shears the sample exhibits a little plateau in viscosity called "zero shear viscosity".

On the other hand, materials without an "apparent yield stress" exhibit this plateau from the shear thinning as the shear rate gets closet to cero (Figure 6-6). The zero-shear viscosity sector effectively describes the viscosity of the sample in low shear rates, this until shear thinning behavior start. At this shear, the sample start to flow until another plateau, described as the infinite shear viscosity plateau, where the viscosity remains constant at very high shear rates.
This behavior occurs as in the shear thinning the irregular structures tends to align and thus, the viscosity decreases consequence of these rearrangements and the increase in free space between dispersed component, then the infinite shear viscosity plateau consists in the maximum degree of orientation that the material can achieve, hence the minimum viscosity.

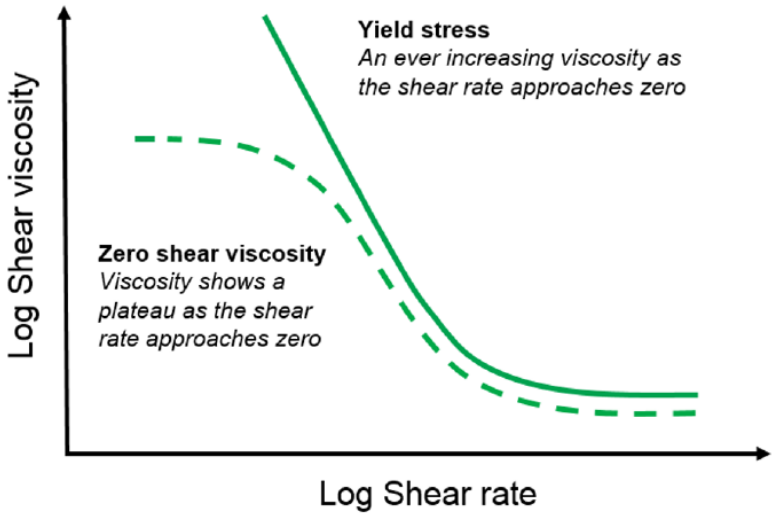

Figure 6-6 Common flow curves for a shear thinning fluids, dash line represent a zero shear viscosity material and continued line a material with an apparent yield stress [85]**.**

Shear thinning can be mathematically described by a power law relationship, therefore, appears like a line in a log-log scale. There are models that can fit these behaviors but will not be discusses in this thesis

On the other hand, shear thickening is a less common behavior that describe the increase of viscosity with the increment of shear. This usually can be found after a critical shear that disrupt the organized flow regime and a so called "hydro-cluster" formation or "jamming" can occur,

increasing the viscosity of the material. Shear thickening can also happen in polymers, high shear rate can open-up and stretch the polymer and expose part of the chain capable of forming intermolecular associations.

Once the shearing force is removed, most materials recover their original viscosity by losing the microstructural rearrangement generated on the shear thinning, making it a reversible process. If this change is time dependent the material is denominated a thixotropy material. Not all shear thinning materials present a thixotropy behavior, but all thixotropy material undergo shear thinning.

A common material that requires a control thixotropy effect correspond to paint, this needs to be strong and stable when it is at rest inside a can but once a shear is apply needs to flow and stick to the wall, finally, the material needs to take an optimal time before it recover its viscosity, if this time is to little, the paint will not fill all the surface, the time needs to be short enough to prevent sagging but letting the paint dissipate and a homogeneous film to be formed.

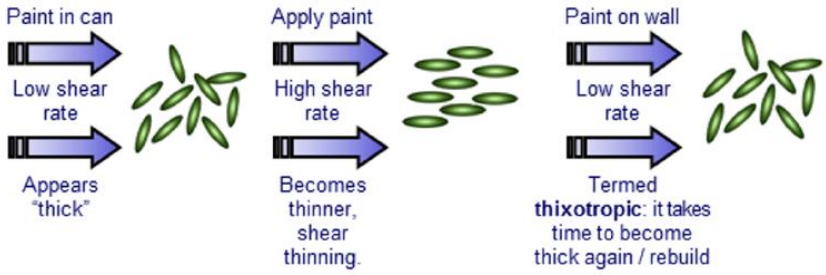

Figure 6-7 Illustration showing a thixotropic material where at rest appears "thick" but flow with a shear, then when the shear is remove, becomes "thick" again with time [85]

5.2.2 Oscillatory rheology

Oscillatory testing is used among others (e.g., creep testing or stress relaxation) to measure the viscoelasticity of a material, this behavior is found in materials somewhere between ideal liquids (viscous) and ideal solid (elastic). The test consists of the oscillation of the upper plate driven by an increment of the shear stress, continuously, the sample will not react immediately, and this delay in the response will be monitored. The most relevant results given by this experiment correspond to the storage modulus (G') and the loss modulus (G"), these represent the elastic and viscous behaviors of the material respectively.

Structure fluids present at rest, the minimum energy state, an equilibrium of the inter-entangled chains of the polymer. If a force or displacement is applied to the state, the equilibrium will be shift and an elastic force will try to restore it to its initial state. This could be represented as a spring that tries to return to his original state after being stretched (Figure 6-8). The same principles of a string can be applied to simple shear deformation. Obeying Hooke's law, the applied stress is proportional to the resultant strain before the elastic limit, this constant of proportionality is the elastic modulus (G) (Equation 6-5). Just as viscosity is a measure of the resistance to flow, the elastic modulus corresponds to the resistance to be deformed (stiffness). Moreover, this change is immediately, meaning there is no time dependence, so when a stress is applied instantly a strain is observed.

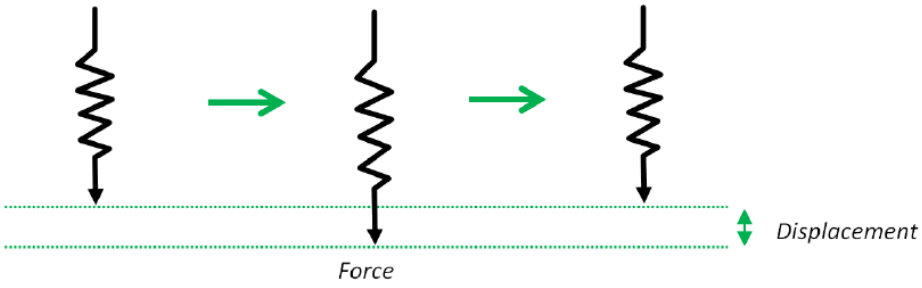

Figure 10 – The response of an ideal solid (spring) to the application and subsequent removal of a strain inducing force

Figure 6-8 The response of an ideal solid (spring) to the application and subsequent removal of a strain inducing force [85]**.**

$$\gamma = \frac{\sigma}{G} \qquad \text{Equation 6-5}$$

On the other hand, viscous behavior can be represented with a dashpot, which follows Newton's law. A dashpot is a mechanical device which resist motion via the viscous friction, this friction is generated when the plunger moves through the viscous Newtonian fluid, generating a permanent strain and dissipating the energy required for the deformation within the fluid (generally as heat). This deformation happens at a constant rate and is given by Equation 6-6 [85].

$$\gamma = \frac{\sigma t}{\eta} \qquad \text{Equation 6-6}$$

Viscoelastic materials present both rheological behaviors, some more elastic and others more viscous. Consequently, it is possible to combine dashpots and springs in such a way that a model describes the real behavior.

Maxwell model correspond to the dashpot and spring connected in series (Figure 6-9), this model represent viscoelastic liquids as the when a stress is applied, at a very short time, the response is predominantly elastic and so on, governed by G, and for long times, the viscous behavior will prevails following η. Joining equations, the strain in Maxwell model can be described with Equation 6-7.

$$\gamma = \sigma\left(\frac{1}{G} + \frac{\sigma t}{\eta}\right) \qquad \text{Equation 6-7}$$

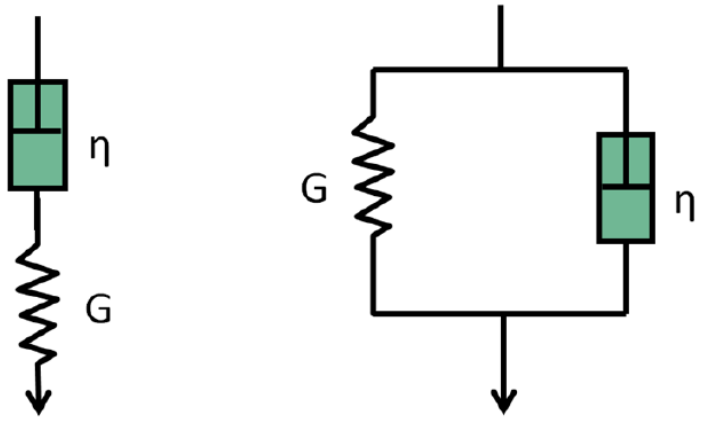

Figure 6-9 Maxwell model in the left, representation of a simple viscoelastic liquid by a dashpot and a string in series. Kelvin-Voigt, on the right, represent a viscoelastic solid with both in parallel [85]**.**

On the other hand, viscoelastic solids are also represented by the dashpot and sprint but in this case, they are connected in parallel, represented by Kelvin-Voigt model in which the strain takes more time to develop as the dashpot retards the effect of the spring making the system a more viscous liquid initially and then elastically over longer time scales. This model presents a retardation time (λ) which correspond to the time that the strain requires to reach 63% of its final asymptotic value and is given by $\frac{\eta}{G}$. Joining equations, the strain in Kelvin-Voigt model can be described with Equation 6-8.

$$\gamma = \frac{\sigma}{G}\left(1 - e^{-t/\lambda}\right)$$ Equation 6-8

Finally, when both models are connected in series the Burges model is generated (Figure 6-10), which best describes the viscoelastic behavior of a system in response to a stress. Moreover, combining both expressions the model can be represented with Equation X.

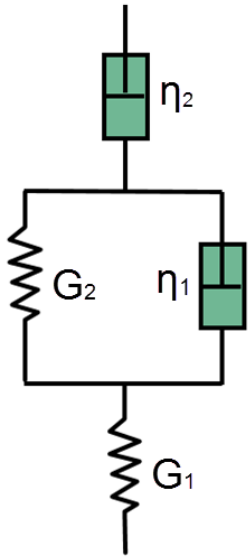

Figure 6-10 Burges model which combines Kelvin-Voigt and Maxwell elements in series [85]**.**

$$\gamma = \sigma\left(\frac{1}{G_1} + \frac{1}{G_2}\left(1 - e^{-\frac{t}{\lambda}}\right) + \frac{t}{\eta_2}\right)$$ Equation 6-9

A rotational experiment, in simple words, is set up by defining a shear rate over time and measure shear stress needed to execute it, with both the viscosity of the material can be calculated. This viscosity generally is affected by the time of the experiment as it is for the shear rate. Having a standard experiment is essential to properly represent all the materials in similar situation. This viscosity is important for 3D printing as is the first guide to use to know how much the material will flow. A low viscosity will mean that the material will flow easily, nevertheless, if the viscosity is too low, the material could be extruded by the shear that exert his own gravity, and thus cannot be printable in a controlled way, for those material a rheological additive need to be add or a bigger needle length should be used to increase the shear at which the material will flow. Knowing the

print speed range of the bioplotter will help to understand in which range the shear rate need to be address. For a certain print speed and a needle diameter, the flow rate can be theoretical calculated. This will help to know in which range the rheological experiments need to be address. As well, to know in which segment the viscosities needs to be compared. For most of materials this viscosity will not be constant in this segment, and thus, a shear thinning could happen. The experiment will provide enough information to avoid those ranges or to use them beneficially.

Oscillatory experiments are those in which the shear stress is defined, and the necessary shear rate is measured. In this case a delay is known and G' and G'' is calculated. These define in which state the material behaves if it is a viscoelastic solid or a viscoelastic liquid, depending on if G'or G'' is bigger respectively. A viscoelastic liquid tends to flow as cannot fully bear their own weight, viscoelastic solid seems more like a "thick" material. For 3D printing is important to have materials that flow, but in a controlled way, as we want them to stop flowing once are deposited into de printing bed, there we want a G' > G'' so the geometry will keep the desire shape. This experiment will give enough information to know if the material can be feasible to print and what happens once is deposited.

These questions will be solved in the next sections after the definition of the used materials and the methods of the rheological analysis.

5.3 Materials

The specifications of PCL-BG composites used in this study are identical to the ones described in Materials in Chapter 4: SCAFFOLD FABRICATION (Table 4-2). Rheological characterization of the different materials was compared at extrusion temperatures – 90°C, 110°C and 130°C – when correspond. The materials were studied under increasing shear rates, shear stresses and temperature to assess flow parameters such as viscosity, storage modulus (G') and loss modulus (G") over time.

5.4 Methods

For rheology properties an Anton Paar MCR 301 rheometer (Austria) was used (Figure 6-11), for all the experiments a parallel plate configuration was used with diameter 25mm and 0.5mm gap between the plates.

Temperature was controlled by the equipment chiller, moreover, for all the experiments a hood was disposed to reduce the interaction between the environment and the experiment, following the model in Figure 6-4.

Rheology experiments were set up depositing enough material (>245 mm^3) on the disposable plate on the desire temperature. Once the material is melted by reaching the desire temperature, the upper plate is drop until a 0.55 mm gap is reached. Then, the excess material is removed, and the experiment take place.

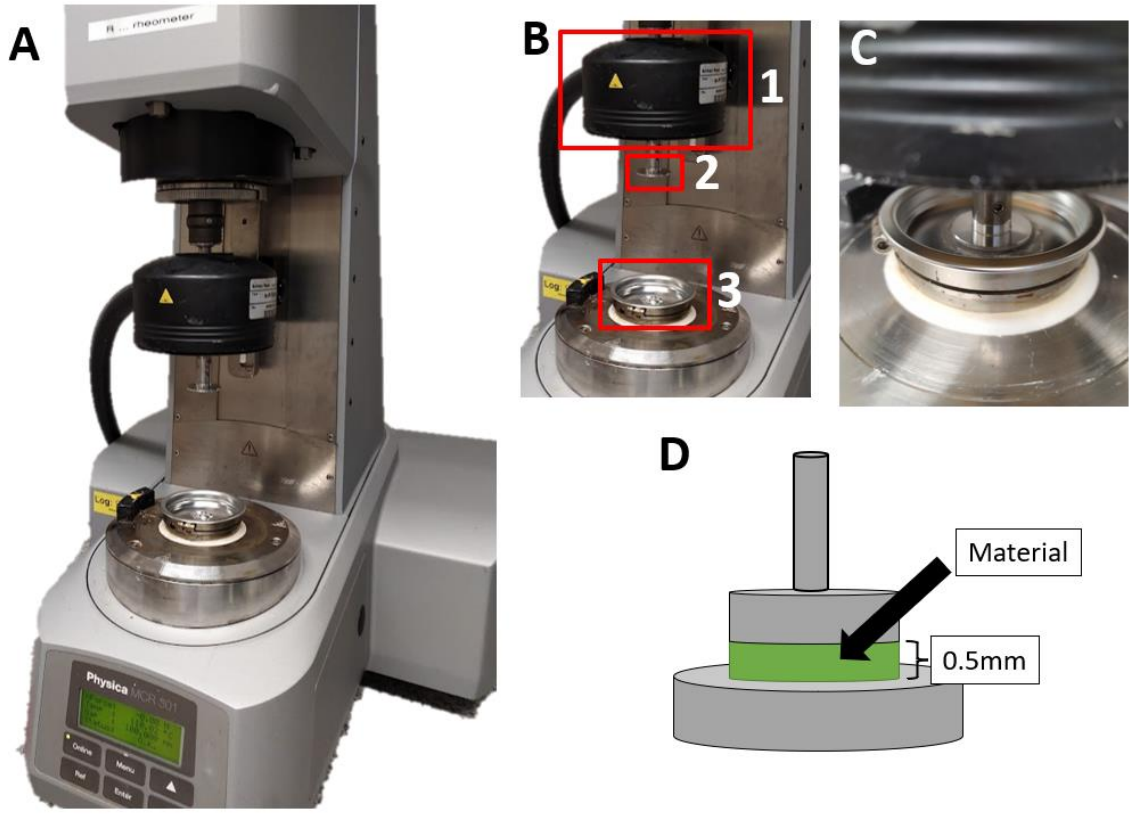

Figure 6-11 Anton Paar MCR 301 rheometer. (A) rheometer in its initial position with (B) pointing out the rheometer parts with (1) as the hood, (2) cylindrical plate and (3) disposable base plate. (C) experimental distance set-up with a gap of 0.5mm previously to lower the hood. (D) sketch of a rheological experiment indicating the components.

5.4.1 Shear strain rate sensibility study

Viscosity is the resistant of the liquid to flow, to measure this resistant and how it varies in different situations. The rheometer has the ability to apply different shear strain rates into a material and measure the shear stress needed to reach these values. The scalar that describes the relation between both is define as the viscosity.

The viscosity of the composites used in this study were assessed by varying the shear strain rates from 10^{-3} to 10^{3} [1/s] at a defined temperature. The used temperatures correspond to the aim printing temperatures.

5.4.2 Shear stress sensibility study

Once the material exits the nozzle, what is going to define if the material will keep the printed shape or will undergo his own weight and lose the shape, correspond to the loss and storage modulus proportion. These defines which part will govern the behavior and how the result will be.

Storage and loss modulus has been widely studied for low temperature material [87], these are crucial to have an adequate printing process. Having a loss modulus bigger than the storage modulus will significate the dilution of the printed material. On the other hand, high temperature printing does not take that much into account these variables as a G" > G' is commonly found on melted materials. Nevertheless, these variables need to be considering and being measure as they introduce how is going to be the behavior of the printing process and what else needs to be considered.

Melted materials usually cannot bare they own height and thus are not able to keep his shape against gravity. This situation corresponds to a G" > G', where the viscous-liquid part is bigger than the elastic, and thus the material flow by the stress generated by his own weight.

The difference between G´and G´´ is measure by oscillatory experiments, a shear stress sweep from 10^{1} to $2*10^{4}$ [Pa] at 1 [Hz] is used to effectively determinate the G' and G" curves for each shear stress and the consider temperature. LVE zones are defined, and the damping factor is calculated for each experiment.

Moreover, for all viscous-elastic liquids the time scale for the elastic response can be determinate. This scale will define how much time the material will keep his shape before the liquid part dominates and the material starts to flow. To determinate this value, an oscillatory test was carried out inside the LVE zone of the different materials, for that, a percentage of deformation (amplitude) inside all LVE regions was used for the whole experiment meanwhile the frequency varied.

5.4.3 Temperature analysis

Being temperature the mayor influence on the rheological properties, different temperatures sweeps were applied to determinate the behavior of the material at different temperatures and forces for an adequate printing process.

To determinate the relation between the viscosity and the temperature, a preliminary rotational experiment was done to determine the zero-shear viscosity plateau and ensure that the viscosity of the sample will not be affected by the shear rate and just the temperature.

The experiment was realized at 110 [°C] with a shear rate sweep from 0.1 to 100 [1/s]. Results shown a zero-shear viscosity plateau in the range of 0.1 to 30 1/s (Showed in results). From this experiment, an ideal shear rate corresponds to 10 [1/s], which is not that big that induce shear thinning, neither that small for the error of the machine being considerable.

Temperature profile was done at a shear rate of 10 [1/s], taking time in consideration, the test was carried with enough time to ensure that the sample is in each desire temperature. The test considers a temperature sweep from 70 [°C] to 150 [°C] in an interval of 1 [h], to ensure that the test does not affect the sample and that the temperature control was the correct, another sweep of 1 [h] was realize just after the test, from 150 [°C] to 70 [°C] in 1 [h]. If both curves match means that the temperature control is effectively register the correspond temperature and that the sample is not being affected by the shear strain rate having the viscosity still on the zero-shear viscosity plateau. Additionally, a 1-hour test was run as well (30 minutes each sweep) for comparison purposes.

On the other hand, an oscillatory experiment was executed on the sample to determinate the variation of G´and G´´ in changes of temperature. The sample was heated to 90 [°C] and the temperature linearly decreased to 20 [°C] with a constant shear stress of 10 [Pa], value on the

LVE. The transition temperature from a viscous-elastic liquid to a viscous-elastic solid was reported, this temperature is defined when the sample present a G´ = G´´, in other words, a loss modulus equal to 1.

5.4.4 Calculation during 3D-Bioplotting

Viscosity is the resistant of the liquid to flow, details how is going to be the flow behavior and how much force will be needed to make the material flow in a certain configuration. In 3D printing a known viscosity is essential to have a feasible amount of force needed to effectively extrude a material through the nozzle.

Rheological experiments on this work aim to describe the rheological properties of the compounds to improve the 3D printing process and look forward to predicting it by improving the understanding of it.

The Bioplotter 3D-printing flow behavior can de predicted, using the information provided by [87]–[89], a series of relations can be define to correlate the print speed with the viscosity of the material for a certain pressure. This using the rheological data and the known data of our system [69].

$$\tau = \eta * \gamma \qquad \text{Equation 6-10}$$

$$\tau * r^{-1} * 2L = \Delta P = 7.3 * 10^{5} \qquad \text{Equation 6-11}$$

$$\gamma = 4Q * \pi^{-1} * r^{-3} \qquad \text{Equation 6-12}$$

$$Q = \pi * r^{2} * v \qquad \text{Equation 6-13}$$

$$\gamma = 4v * r^{-1} \qquad \text{Equation 6-14}$$

$$v = \Delta P * r^{2} * (8L * \eta)^{-1} \qquad \text{Equation 6-15}$$

$$v = 561{,}5385 * \eta^{-1} \qquad \text{Equation 6-16}$$

Where τ is the shear stress, η the viscosity, $\dot{\gamma}$ the shear strain rate, ΔP the pressure applied at the nozzle, r is the radial position from the center to the edge of the nozzle, and L the nozzle length. Using the parameters of our 3D printer, ($\Delta P = 7.3 * 10^{5}\ Pa$; $r = r_{max} = 200 * 10^{-6} m$; and $L = 6.5 * 10^{-3} m$) [87]. This equation works for a strut the same size as the nozzle diameter, in case the desire strut is not the same as the nozzle size, the relation will be invalid.

Using Equation 6-16, the temperature-viscosity results can be described in a temperature-speed relation, using the desire 3D printing configuration. Nevertheless, there is a condition that need to be fulfil, for the speed to correspond to the flow extruded, the shear rate applied on the nozzle needs to be on the zero-shear viscosity plateau.

The speed-temperature profile gives a guide of which speed expect at the Bioplotter, this by the rheological experiments using little amount of material (~250 [mm^3]) and before using the Bioplotter. Having more information for a more effectively design of the experiments.

On the other hand, having a nice flow is important, but as well what happens once the material leave the nozzle, is essential that the material preserves the shape once is deposited. It is known that when a high temperature material, with low viscosity, decrease its temperature, the viscosity does otherwise, it increases. As well does the relation between G' and G", they come closer until a point (before the freezing temperature) where G' = G", this equilibrium point is where the strut starts to behave more a solid rather than a liquid, thus, the printed geometry can keep his shape.

A big difference between the proportion of the G" and G' means the need to decreasing faster the temperature, requiring an external system for it as the natural convection is not enough.

Then, Equation 6-11 is used to correlate the shear stress of the experiment with the one at the tip of the nozzle, knowing how is going to be the behavior of the flow inside the nozzle. Once the material is deposited, the relation that govern is on the LVE sector, which describe how is going to be this relation without external forces.

5.5 Results and discussion

5.5.1 Viscosity analysis results

Zero shear viscosity plateau is not always the desire behavior, for high viscous liquids, a shear thinning is needed in order to effectively print the material at a reasonable speed. High viscosity samples could have speeds lower than 1 [mm/min] meaning that the printing process could easily take hours for big samples. Shear thinning behavior makes the viscosity decrease at a big rate with a low change on the shear strain rate, a minus change on shear stress (induce by the pressure) will make the sample flow way easier. On the other hand, samples with shear thinning will present an

aligned structure once deposited [87], controlling the molecular structure of the sample in another level for non-thixotropic materials. However, for thixotropic materials, the viscosity will increase once leaves the nozzle, easing the strut to keep the desire shape.

A rotational test was carried out to measure the relation between the shear rate and viscosity, an increment of shear rate from 0.1 to 100 [1/s] was used and the printing range was determinate with Equation 6-11. Figure 6-12 show how for all temperatures the shear thinning behavior start just after the printing range, with it on the zero-shear viscosity plateau, and thus predicting a constant printing flow and allowing the correct use of Equation 6-16 to approximate the printing speed.

For this set up, the shear thinning was not on the printing range, the Bioplotter configuration was on the maximum pressure and thus, no more shear rate can be achieved. However, the shear strain rate can be increase by changing the needle size, and hence, print on the shear thinning behavior.

Figure 6-12 algo show how the different temperatures affect the viscosity of the compound, high temperature as 130 [°C] present the lowest viscosity on the range of 150-180 [Pa*s], meanwhile 110 [°C] present almost a 50% of increments with a range of 220-250 [Pa*s], finally, the lowest temperature 90 [°C] behave with the highest viscosity of 400-440, a 166% increment with respect to the high temperature viscosity. Color bands represent a 95% of confidential interval for each compounding method.

Moreover, in each individual temperature the compounds perform with different viscosity, similar trend is exhibit for 110 and 130 [°C] where both PCL-Ace and PCL-Mini present the lowest viscosity, meanwhile, PCL and PCL-DCM exhibit a higher local viscosity for each temperature respectively. Nevertheless, this trend in not exhibit on 90 [°C] where PCL-Ace present the lowest viscosity and all the other compounding methods a higher one.

Additionally, shear thinning behavior seems to correlate with the decrease of viscosity, higher viscosity samples (90 [°C]) present a shear thinning behavior at lower shear strain rates (~30) [1/s], meanwhile, 110 [°C] exhibit it at ~40 [1/s], a higher shear strain rate. Moreover, the experiment fails to achieve the required shear strain rate to determinate the shear thinning for 130 [°C].

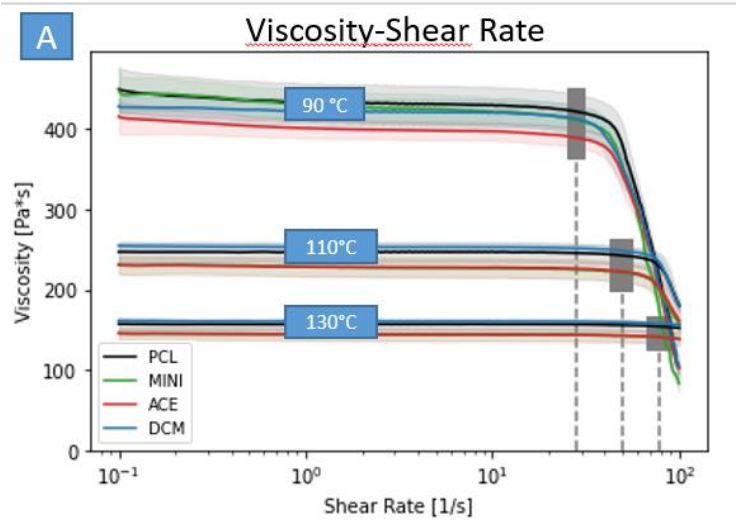

Figure 6-12 Shear rate sweep for different methods and temperature. Grey areas determine the printing range for the current configuration. Color areas represent a 95% confidential interval.

To understand if the rheological properties of the PCL-BG compound and if is compatible with the setting used in the 3D-Bioplotter, the variation of viscosity was assessed by a shear strain rate sweep. PCL + 20% BG exhibited the highest viscosity of all the three inks throughout the range of shear rates tested (Figure 6-13). Pure PCL exhibited slightly lower viscosity than PCL + 10% BG at shear rates between 10^{-3} – 10^{1} [1/s]. However, although the composite inks began exhibiting shear thinning behavior between 10^{-1} – 10^{0} [1/s], viscosity response of pure PCL remained more-or-less constant revealing neither shear thinning nor, more importantly, shear thickening behavior in the range tested.

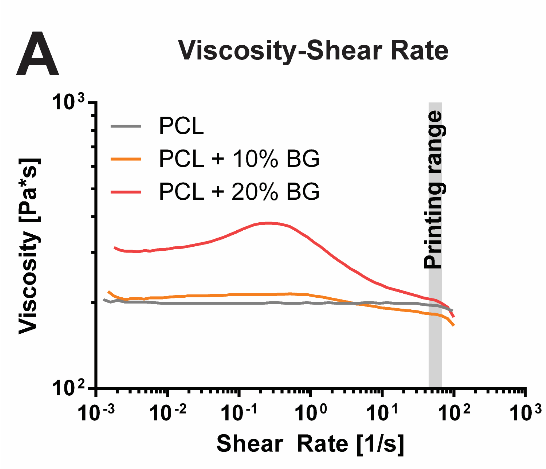

Figure 6-13 PCL – BG composite material rheological properties. (A) Rotational rheological measurements for the different compositions of BG at 110°C. Note: The grey area shows the printing ranges for the current configuration.

5.5.2 Storage and loss modulus analysis results

To understand if the rheological properties of the inks are compatible with the settings used in the 3D-Bioplotter, we also assessed the variation of storage modulus (G') and loss modulus (G'') at various values of shear stress and shear rates at different temperatures.

G' and G'' are reported as the Loss Factor (G''/G'), Figure 6-14 show the results for the different compounding methods and print temperatures. For all the combinations the loss factor remains over 1, meaning that G'' is bigger than G', for 90 [°C] the difference corresponds to 5-6 times bigger in the LME, meanwhile that for 130 [°C] is about 15 times bigger, meaning that higher temperatures present a more viscose-liquid behavior rather than low temperatures with less flow of the material. For the printing range, these values are even bigger, indicating that the material will flow even easily. Nevertheless, this positive values also suggest that the material will spread at this temperature as the G'' is bigger than G'. A temperature study will analyze what happens when the strut start to cool down and the rheological properties of the ink start to change.

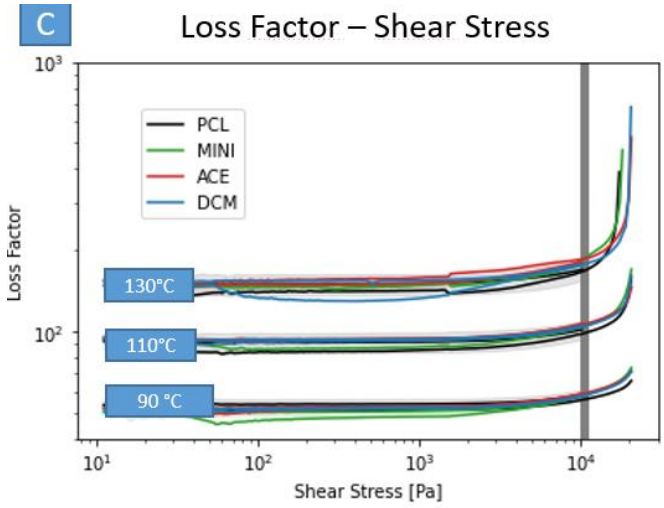

Figure 6-14 PCL rheological properties. Oscillatory rheological measurements (frequency = 1) for the different methods. Grey areas determine the printing range for the current configuration.

Both the loss modulus (G") and the storage modulus (G') was assessed for PCL-BG composited, showing higher values with increasing percentage of BG (Figure 6-15). In all three cases, the loss modulus was greater than the storage modulus (G" > G'), moreover, this difference increases with the percentage of BG. Furthermore, LVE region exhibit a different behavior for the compounds, both PCL-BG composites present a clear end of the LVE region around a shear stress of 10^3 [Pa], meanwhile, PCL composite remain constant on the experimental range.

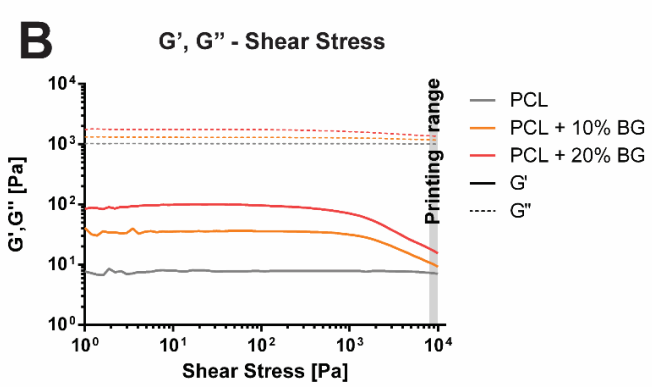

Figure 6-15 PCL – BG composite material rheological properties. (B) oscillatory (frequency = 1 Hz) rheological measurements for the different compositions of BG at 110°C. Note: The grey area shows the printing ranges for the current configuration.

5.5.3 Temperature results

Being the temperature the variable that mostly drives the viscosity behavior, it is essential to characterize the relation between both for a proper understanding. Under a constant shear strain rate in the zero-shear viscosity plateau, a temperature sweep was executed. The test was performed in a time scale enough for the sample to reach the objective temperature defined to the machine, to accurately record the exact viscosity for each temperature. This was later confirmed by running the same test backwards as soon the first was finished. Having math between both temperature-viscosity relations would mean that the time scale is big enough to match the design set up with the experimental one.

Figure 6-16 show the results of the 2 hours test, were both curves match, meaning is an accurate experiment. On the other hand, a 1-hour test was run as well (30 minutes each sweep). This delay corresponds to the time that takes the sample for receiving the temperature defined by the rheometer. Viscosity behavior can be related with the temperature. Figure 6-16 already shows the transformation from viscosity to speed (printing speed) using Equation 6-16. This relation provides enough information to address properly different material using rheological information for new temperatures and pressures. In this case, the starts show the comparation with the experimental data, where the lines represent the found relation. The minor difference between the prediction and the experimental acquisition is attributed to the fan set up that affect the nozzle temperature in some moments.

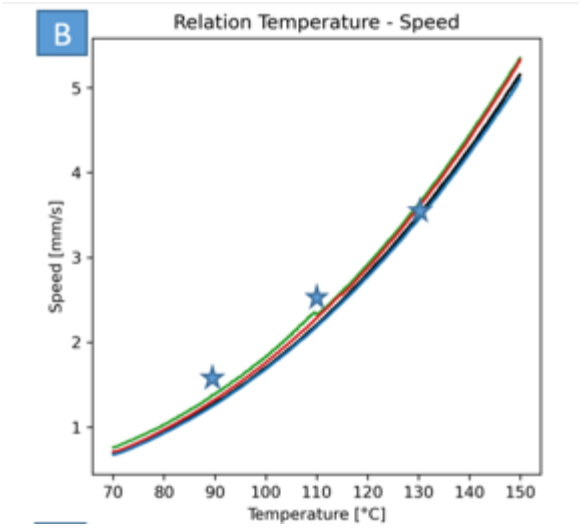

Figure 6-16 Temperature viscosity relation. Temperature sweep at zero shear viscosity plateau in a rotational configuration. Colors lines represent the different methods and stars the used speed for the different extrusion temperatures.

Moreover, oscillatory experiments were run as well to understand the behavior of the phases of the viscous-elastic material. To accurately measure in which point there is going to be a transition temperature, and which is going to be the viscosity at that point. Another oscillatory test was performed, the shear stress was kept constant at 10 [Pa] and the temperature decrease from 90 [°C] to 20 [°C]. A loss modulus (G"/G') of 1 (G' = G") determine the solidification temperature, Figure 6-17 show these points with an "x" for each material and the inserted table the respectively values. The viscosity on this point is reported as well.

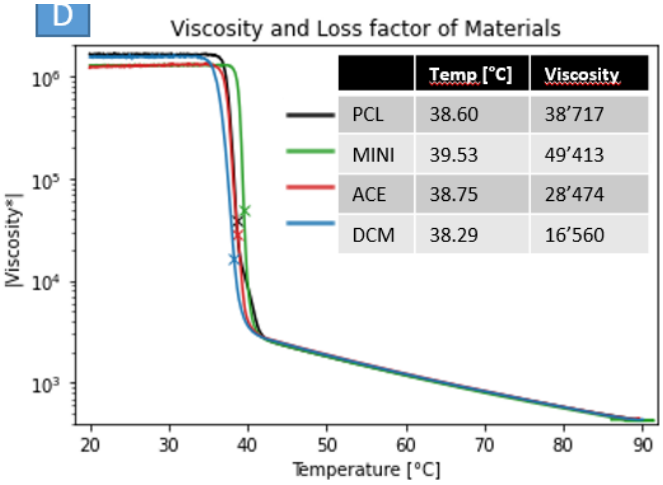

Figure 6-17 PCL rheological properties. oscillatory measurements of negative temperature sweep at constant shear rate. Grey areas determine the printing range for the current configuration.

5.5.4 Calculation during 3D-Bioplotters results

Given that 3D-Printing with DIW depends on the extrusion of a viscous material in a controlled pattern, it is relevant to measure the rheological properties of the ink [90]. This also becomes pertinent when printing with bioactive glasses [91]. Additionally, when manufacturing composites materials, some additional factors need to be considered, such as the use of an appropriate solvent to mix the components, as well as the distribution of any particles within the matrix. Hence, the variation of the viscosity, the storage and loss modulus (G' and G") was used to determine the initial parameters for the 3D printing process.

First, higher viscosity will lead to the need of greater printing pressures. Secondly, G" > G' leads to a variation of the optimum pressure with respect to the printed time and, most importantly, to the state of the ink once printed. Having G" > G' implies that the material will continue to flow once deposited on the structure, requiring an external mechanism to quickly cool the printed melt after leaving the nozzle to reach a state where G' ≥ G", thus preserving the printed shape.

Thus, a rheological characterization of the ink becomes relevant because it guarantees that key settings for DIW, such as pressure, are within the printing range for the desired ink properties, it allows to identify the range of process parameters instigating shear thinning behavior of the ink when printing, while avoiding the shear thickening behavior. Additionally, given that BG particles

affect these properties along different concentrations, future studies can parametrically assess the rheological properties of the inks to allow for the printing of scaffolds with high resolution without loss of repeatability.

Other studies have also considered the rheological properties of biomaterials to be used in 3D printing by similar assessments to the ones used in this study, by employing either pure [92] or composite materials with bioactive glasses or other ceramics [93], [94], as well as studying the use of solvents for material mixing and particle distribution [95]. However, these studies have used pastes with no defined microarchitecture, or structures with low height/width aspect ratios, [92], [94]. The assessment of the rheological properties of the ink when fabricating large samples, as the ones used in this study, is a key feature, given that the correct control of the rheological properties of the inks will guarantee that such structures do not collapse during the ink writing process when adding several layers in the vertical direction. Furthermore, it will allow for external factors to be considered when printing, such as forced convection to rapidly decrease the temperature of the inks after deposition.

After a preliminary evaluation of the rheological properties and printability over a range of temperatures above the melting point of PCL/PCL-BG, we settled on a printing temperature of 110°C for this initial, feasibility study. In principle, the advantage of printing at lower temperatures lies in the quick solidification of the printed filament, thus resulting in a smaller deviation from designed micro-architectural parameters. On the other hand, the ink is much more viscous, requiring much higher pressures to enable smooth flow of the ink through the nozzle, while maintaining a homogeneous composite mixture. Often, this can lead to a failure in printing midway through the process and result in wastage of the ink. If the temperature is too high, the flow of the ink through the nozzle is much smoother and printing could theoretically occur at lower pressures. However, the printed filament will then continue to "spread" rather than solidify quickly and may not maintain design dimensions, resulting in loss of fidelity [96]. While this can be mitigated to an extent better cooling procedures or longer wait times between each successive printed layer, this option is equally sub-optimal.

A more systematic study to quantify the effect of varying temperatures on the printing parameters show that the variation of temperature has a direct influence on the viscosity of the sample, and thus, the speed needed for an optimal printing process. This relation was describe defining a capillary system, where the force applied by the machine can be correlated with the speed at which

the material flow though the nozzle in a certain configuration. Using the data presented on the previous sections and Equation 6-16 a relationship can be made between the rheological experiments and the initial parameters for the 3D-printing process. Figure 6-16 shows the optimal printing speed for each temperature and composites. There is not a clear difference on the optimal printing speed for the different compound, as was expected with the minor difference in viscosity for each local temperature. Moreover, the experimental values are placed on Figure 6-16 to demonstrate the accuracy of the prediction, showing low error due to experimental factors as degradation of the material, and reduce nozzle objective temperature by the air flow generated by the fan set up.

To ensure that this curve is accurate enough, experimental data was used (Figure 6-18), showing that the curves are relatively close to the optimal speed values, this difference is attributed to the cooling system that decrease the temperature of the nozzle tip. Nonetheless, this phenomenon represents when multiple structure is being printed and the air flow of the fans cannot reach the nozzle for a stable time, leaving the nozzle at the configured temperature.

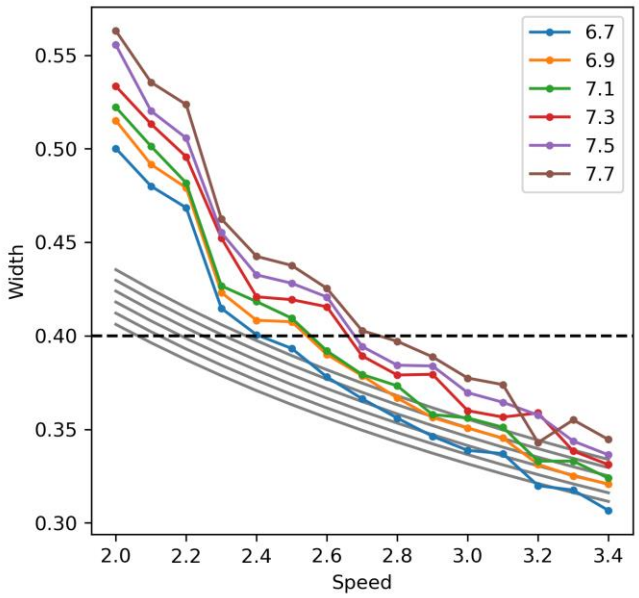

Figure 6-18 Verification of the formula. Values (dots) represent the width (diameter) measurement of 3D-printed lines of 10 cm length at different configuration of printing speed [mm/s] and pressure [bar]. Colors represent the different used pressure, grey lines show the theoretical value using Equation 6-16 for the different pressures, being top 7.7 [bar] and the bottom one 6.7 [bar]. Dashed line represents the nozzle diameter and the intersect with the lines the optimal configuration for 3D-printing were nozzle diameter equals strut diameter.

5.5.5 Inferences

- The different compounding methods show a variation in the viscosity. This trend seems to be independent of the temperature as PCL-ACE and PCL-Mini present a low viscosity for 90 and 110 °C in the shear rate sensibility study. Nevertheless, this trend seems to be mixed for 130 °C. The difference between the different compounding methods is quite small but the 95% confidential show that the do not merge in the LVE zone. The results are mixed once the shear thinning behavior start. However, this could be because of the low sensibility of the machine at these ranges or the high increment of shear rate over time.
- Higher viscosities present a shear thinning behavior at lower shear strain rates. This happens for all methods, including the samples with BG, where a high viscosity presents a shear thinning behavior at low shear rate.
- For the viscosity graphs can be evidence that the printing area correspond to the zero-shear viscosity plateau, meaning that the printing process will be regular and high variations will not be expected.
- The oscillatory experiments show that the printing range is on the LVE region for the storage and loss modulus, suggesting the same behavior as with the viscosity, a regular 3D printing process that do not considerable change over time.
- The loss modulus shows that G'' is way bigger than G', meaning that an external system will be needed to cool down the sample before start to spread.
- The rheological data can be used to predict the speed needed for 3D printing; this is quite important as the material needed to set up a new ink will be considerable reduce. The correlation was compared with experimental data showing a low error, induce by the fan set up that reduce the temperature of the needle and thus increase the viscosity of the ink.

5.6 Chapter Summary

This Chapter describes the methodology and results to understand better the used ink for scaffold fabrication. First an extensive section to understand rheology and the fundamentals was presented. Then the material and methods were explained in order to show the process that was done. Rotational and oscillatory experiments were made to address the rheological properties by viscosity, G' and G'', furthermore, amplitude, frequency and temperature were addresses as well. These were analyzed and bring to one step further to be correlated with the behavior of the bioplotter extrusion. The ink analysis show that the different temperatures present a zero-shear stress plateau where the bioplotter extrude. The shear thinning behavior of the different inks cannot be achieve with the current configuration. A formula was described to correlate the viscosity of the material with the printing speed. Furthermore, this information was used along a temperature profile to correlate the temperature with an estimate of the printing speed. Experimental data reveals that the predicts values are close to the forecast.

CHAPTER 6: CONCLUSIONS AND FUTURE WORK

6.1 Conclusions

The principal contribution of the current thesis corresponds to a methodology to generate accurate scaffolds by diverse methods and a tool to numerically measure the quality of the samples. The accurately fabricated scaffolds were achieved by an external fan set up that effectively reduce the temperature of the struts to avoid the spread of the material. This additional system increases the fidelity of the sample as the material keeps the position and shape as was deposited. To increase even more the accuracy of the printing process with respect to the design. The custom-made code gives in situ information of the dimensions of the printed strut. Knowing if the printer is over extruding or if any undesired details is being produce. Allowing to a fast variation of the printing parameters and thus an improvement of the printed shape. Furthermore, the custom-made code then analyses the whole series of images and gives enough information to understand in detail the inner architecture of the sample. Furthermore, the rheological methodology improves the actual try and error system for a new material, with the rheological information it is possible to know a reference pressure and printing speed in order to start near the actual experimental value. This considerable reduce the amount of material needed to set up a new material as increase the quality of the samples and thus the reproducibility of them.

These effectively methods give a guide on how to approach a new material and how to effectively characterize a printed scaffold. These results can be correlated with the mechanical and biological behaviors of the samples. In this case, these are just used to prove the reproducibility of the samples and the fidelity of the printing process. A future work aims to annex the different chapters to have a better understanding of the process and how to improve it even more.

The main fin outs in this thesis for the scaffold's characterization, correspond to the mechanical and biological characterization. With different compound not showing a clear trend in mechanical behavior and needed for a deeper statistical analysis but showing how the addition of BG decrease the mechanical properties. Nevertheless, was reported that this could be because of the addition of DCM or the wrong biding between the BG and the matrix material.

Biological characterization shows how the BG is beneficial at the first week, but the proliferation starts to decrease on the second one. This could be for a series of reasons, but a future work needs to be done to increase the number of repetitions and thus the veracity of the experiment.

Rheological analysis effectively predicts the extrusion speed with a two-hour experiment using a low quantity of material. This opens a door to reduce the amount of material needed to analysis the feasibility of printing, and the time for the set-up process.

This thesis delivered a series of options to take in consideration when 3D printing, a series of experiments where not presented in this thesis (e.g., DSC, EDS, TGA, XRD, static testing under micro-CT, among others) these are aimed to be presented in a further work with more time for the writing and the proper analysis of them. As well, the interaction between all the presented experiments is not properly shown, the statistics is basic and thus a deeper work is needed for a mayor contribution. Further work section reveals a series of point that want to be addresses in the near future.

6.2 Future Work

The present work gives a guideline to follow for new materials. Nevertheless, this guideline can be improved, and the factors presented could be properly certify with their variations and conditions. A series of additional experiments are listed that we found to be relevant for future experiments.

6.2.1 Deeper statistical analysis

Currently the statistics presented in this thesis is not as strong as we desire, the time and effort for it was not presented. And thus, a series of relations and factors were not analyzed, a list of them are presented:

- Pore size and mechanical properties
- Pore size and biological behavior
- Mechanical properties and G’ and G’’
- Mechanical properties and the freezing temperature
- Mechanical properties and porosity
- Porosity and biological behavior

These are the relations that can be analyzed with the present information and are listed for a future work.

6.2.2 New materials and combination of them

Having a guide of how to produce and evaluate scaffolds, new material will not present the same threat as before. For that, one of the future works will be try different new materials and the combination of them.

6.2.3 Digital volume correlation

Static testing under the micro-CT produces a series of volumes that show the local deformation of the sample. This information wants to be used to generate a digital volume correlation and understand which part of the scaffolds present the bigger strains. The idea behind this evaluation is to annex the local strain with the biological behavior for better performance.

6.2.4 Robust biological experiment

Currently, the biological experiments have the minimum size of samples. A better experiment was done in the previous months and the analysis of it is needed. The wells were used for testing the material with a high number of repetitions, but more cubes need to be tested as well, in order to evaluate the biological performance in a relevant size structure. Trying to have a better understanding of the biological performance and the inner architecture of the scaffold.

REFERENCES

[1] D. Varghese, M. Deshpande, T. Xu, P. Kesari, S. Ohri, T. Boland, and U. Kingdom, "Advances in tissue engineering : Cell printing," no. February, pp. 470–472, 2005.

[2] R. Langer and J. P. Vacanti, "Tissue engineering," *Science*, vol. 260, no. 5110, pp. 920–926, May 1993.

[3] B. Palsson, J. A. Hubbell, R. Plonsey, and J. Bronzino, Eds., "Tissue engineering," *Asia-Pacific Journal of Chemical Engineering*, vol. 6, no. 6. 2003.

[4] U. S. D. of H. and H. Services, "OPTN/SRTR 2012 Annual Data Report," 2014.

[5] T. Billiet, M. Vandenhaute, J. Schelfhout, S. Van Vlierberghe, and P. Dubruel, "A review of trends and limitations in hydrogel-rapid prototyping for tissue engineering," *Biomaterials*, vol. 33, no. 26, pp. 6020–6041, 2012.

[6] R. K. Malcolm, S. D. Mccullagh, A. D. Woolfson, S. P. Gorman, D. S. Jones, and J. Cuddy, "Controlled release of a model antibacterial drug from a novel self-lubricating silicone biomaterial," vol. 97, pp. 313–320, 2004.

[7] N. E. Fedorovich, J. Alblas, W. E. Hennink, W. J. A. Dhert, and F. O. Cumhur, "Organ printing : the future of bone regeneration ?," vol. 29, no. 12, pp. 601–606, 2011.

[8] J. Lee, M. J. Cuddihy, and N. A. Kotov, "Three-dimensional cell culture matrices: State of the art," *Tissue Eng. - Part B Rev.*, vol. 14, no. 1, pp. 61–86, 2008.

[9] L. E. Freed and F. Guilak, "Engineering functional tissues," in *Principles of Tissue Engineering*, 3rd ed., R. Lanza, R. Langer, and J. Vacanti, Eds. 2007, pp. 137–153.

[10] E. Carletti, A. Motta, and C. Migliaresi, "Scaffolds for Tissue Engineering and 3D Cell Culture," *3D Cell Cult. Methods Protoc. Methods Mol. Biol.*, vol. 695, no. 2, pp. 1–15, 2011.

[11] R. Langer, "Perspectives and challenges in tissue engineering and regenerative medicine," *Adv. Mater.*, vol. 21, no. 32–33, pp. 3235–3236, 2009.

[12] ASTM, *Dictionary of Engineering Science and Technology, 10th Edition*. 2005.

[13] B. C. Isenberg and J. Y. Wong, "Building structure into engineered tissues," *Rev. Lit. Arts Am.*, vol. 9, no. 12, pp. 54–60, 2006.

[14] F. Berthiaume, T. J. Maguire, and M. L. Yarmush, "Tissue engineering and regenerative medicine: History, progress, and challenges," *Annu. Rev. Chem. Biomol. Eng.*, vol. 2, pp. 403–430, 2011.

[15] M. B. Murphy and A. G. Mikos, "Polymer scaffold fabrication," in *Principles of Tissue Engineering*, 3rd ed., R. Lanza, R. Langer, and J. Vacanti, Eds. 2007, pp. 309–321.

[16] S. Yang, K. F. Leong, Z. Du, and C. K. Chua, “The design of scaffolds for use in tissue engineering. Part II. Rapid prototyping techniques,” *Tissue Eng.*, vol. 8, no. 1, pp. 1–11, 2002.

[17] O. A. Abdelaal and S. M. Darwish, “Fabrication of Tissue Engineering Scaffolds Using Rapid Prototyping Techniques,” *Int. J. Ind. Manuf. Eng.*, vol. 5, no. 11, pp. 2310–2310, 2011.

[18] W.-J. Li and J. A. Cooper, “Fibrous Scaffolds for Tissue Engineering,” 2011.

[19] S. Priyanka, “Characterization of 3D-Bioplotting of e-Polycaprolactone for Tissue Engineering Applications,” 2014.

[20] D. W. Hutmacher, “Scaffold design and fabrication technologies for engineering tissues - State of the art and future perspectives,” *J. Biomater. Sci. Polym. Ed.*, vol. 12, no. 1, pp. 107–124, 2001.

[21] J. M. Pachence, M. P. Bohrer, and J. Kohn, “Biodegradable Polymers,” in *Principles of Tissue Engineering*, 3rd ed., R. Lanza, R. Langer, and J. Vacanti, Eds. 2007, pp. 323–339.

[22] G. P. Duffy, T. M. McFadden, E. M. Byrne, S. L. Gil, E. Farrell, and F. J. O’Brien, “Towards In vitro vascularisation of collagen-GAG scaffolds,” *Eur. Cells Mater.*, vol. 21, no. January 2011, pp. 15–30, 2011.

[23] B. Stevens, Y. Yang, A. Mohandas, B. Stucker, and K. T. Nguyen, “A review of materials, fabrication methods, and strategies used to enhance bone regeneration in engineered bone tissues,” *J. Biomed. Mater. Res. - Part B Appl. Biomater.*, vol. 85, no. 2, pp. 573–582, 2008.

[24] R. Dwivedi, S. Kumar, R. Pandey, A. Mahajan, D. Nandana, D. S. Katti, and D. Mehrotra, “Polycaprolactone as biomaterial for bone scaffolds: Review of literature,” *J. Oral Biol. Craniofacial Res.*, vol. 10, no. 1, pp. 381–388, Jan. 2020.

[25] M. Bartnikowski, T. R. Dargaville, S. Ivanovski, and D. W. Hutmacher, “Degradation mechanisms of polycaprolactone in the context of chemistry, geometry and environment,” *Prog. Polym. Sci.*, vol. 96, pp. 1–20, Sep. 2019.

[26] M. Labet and W. Thielemans, “Synthesis of polycaprolactone: a review,” *Chem. Soc. Rev.*, vol. 38, no. 12, p. 3484, 2009.

[27] J. M. Williams, A. Adewunmi, R. M. Schek, C. L. Flanagan, P. H. Krebsbach, S. E. Feinberg, S. J. Hollister, and S. Das, “Bone tissue engineering using polycaprolactone scaffolds fabricated via selective laser sintering,” *Biomaterials*, vol. 26, no. 23, pp. 4817–4827, 2005.

[28] H. Pae, J. Kang, J. Cha, J. Lee, J. Paik, U. Jung, B. Kim, and S. Choi, “3D-printed

polycaprolactone scaffold mixed with β-tricalcium phosphate as a bone regenerative material in rabbit calvarial defects," *J. Biomed. Mater. Res. Part B Appl. Biomater.*, vol. 107, no. 4, pp. 1254–1263, May 2019.

[29] M. A. Woodruff and D. W. Hutmacher, "The return of a forgotten polymer - Polycaprolactone in the 21st century," *Prog. Polym. Sci.*, vol. 35, no. 10, pp. 1217–1256, 2010.

[30] B. Dhandayuthapani, Y. Yoshida, T. Maekawa, and D. S. Kumar, "Polymeric Scaffolds in Tissue Engineering Application: A Review," *Int. J. Polym. Sci.*, vol. 2011, no. ii, pp. 1–19, 2011.

[31] J. R. Jones, D. S. Brauer, L. Hupa, and D. C. Greenspan, "Bioglass and Bioactive Glasses and Their Impact on Healthcare," *Int. J. Appl. Glas. Sci.*, vol. 7, no. 4, pp. 423–434, 2016.

[32] P. S. P. Poh, D. W. Hutmacher, B. M. Holzapfel, A. K. Solanki, M. M. Stevens, and M. A. Woodruff, "In vitro and in vivo bone formation potential of surface calcium phosphate-coated polycaprolactone and polycaprolactone/bioactive glass composite scaffolds," *Acta Biomater.*, vol. 30, pp. 319–333, 2016.

[33] T. S. Karande, J. L. Ong, and C. M. Agrawal, "Diffusion in musculoskeletal tissue engineering scaffolds: Design issues related to porosity, permeability, architecture, and nutrient mixing," *Ann. Biomed. Eng.*, vol. 32, no. 12, pp. 1728–1743, 2004.

[34] Y. Luo, G. Engelmayr, D. T. Auguste, S. Ferreira, J. M. Karp, and I. Introduction, "Three-Dimensional Scaffolds," in *Principles of Tissue Engineering*, 3rd ed., R. Lanza, R. Langer, and J. Vacanti, Eds. 2007, pp. 359–373.

[35] A. Rosengren and L. M. Bjursten, "Pore size in implanted polypropylene filters is critical for tissue organization," *J. Biomed. Mater. Res. - Part A*, vol. 67, no. 3, pp. 918–926, 2003.

[36] J. H. Brauker, V. E. Carr-brendel, L. A. Martinson, J. Crudele, W. D. Johnston, and R. C. Johnson, "Neovascularization of synthetic membranes directed," *Mater. Res.*, vol. 29, pp. 1517–1524, 1995.

[37] W. M. Saltzman, *Cell interactions with polymers*, Second Edi., no. 1. Elsevier Inc., 2006.

[38] S. Yang, K. F. Leong, Z. Du, and C. K. Chua, "The design of scaffolds for use in tissue engineering. Part I. Traditional factors," *Tissue Eng.*, vol. 7, no. 6, pp. 679–689, 2001.

[39] R. Landers, A. Pfister, U. Hübner, H. John, R. Schmelzeisen, and R. Mülhaupt, "Fabrication of soft tissue engineering scaffolds by means of rapid prototyping techniques," *J. Mater. Sci.*, vol. 37, no. 15, pp. 3107–3116, 2002.

[40] R. Vallejos Baier, J. I. Contreras Raggio, C. Toro Arancibia, M. Bustamante, L. Pérez, I. Burda, A. Aiyangar, and J. F. Vivanco, "Structure-function assessment of 3D-printed

porous scaffolds by a low-cost/open source fused filament fabrication printer," *Mater. Sci. Eng. C*, vol. 123, no. March, 2021.

[41] C. Z. Liu and J. T. Czernuszka, "Development of biodegradable scaffolds for tissue engineering: A perspective on emerging technology," *Mater. Sci. Technol.*, vol. 23, no. 4, pp. 379–391, 2007.

[42] W. Y. Yeong, C. K. Chua, K. F. Leong, and M. Chandrasekaran, "Rapid prototyping in tissue engineering: Challenges and potential," *Trends Biotechnol.*, vol. 22, no. 12, pp. 643–652, 2004.

[43] H. Ke and X. B. Chen, "Modeling of the scaffold fabrication process for tissue engineering applications," *Can. Conf. Electr. Comput. Eng.*, vol. 2005, no. May, pp. 1255–1261, 2005.

[44] D. L. Bulter, S. A. Goldsteinm, and F. Guilak, "Functional tissue engineering: The role of biomechanics," *Ann. N. Y. Acad. Sci.*, vol. 122, no. December 2000, pp. 570–5, 2000.

[45] X. Wang, J. S. Nyman, X. Dong, H. Leng, and M. Reyes, "Fundamental Biomechanics in Bone Tissue Engineering," *Synth. Lect. Tissue Eng.*, vol. 2, no. 1, pp. 1–225, Jan. 2010.

[46] P. J. Thurner, B. Erikson, Z. Schriock, J. Langan, J. Scott, M. Zhao, G. E. Fantner, P. Turner, J. H. Kindt, G. Schitter, and P. K. Hansma, "High-speed photography of human trabecular bone during compression," *Mater. Res. Soc. Symp. Proc.*, vol. 874, pp. 97–102, 2005.

[47] S. H. Masood, J. P. Singh, and Y. Morsi, "The design and manufacturing of porous scaffolds for tissue engineering using rapid prototyping," *Int. J. Adv. Manuf. Technol.*, vol. 27, no. 3–4, pp. 415–420, 2005.

[48] C. J. Bettinger, J. T. Borenstein, and R. Langer, "Micro- and nanofabricated scaffolds," in *Principles of Tissue Engineering*, R. Lanza, R. Langer, and J. Vacanti, Eds. 2007, pp. 341–358.

[49] P. V. Grant, C. M. Vaz, P. E. Tomlins, L. Mikhalovska, S. Mikhalovsky, S. James, and P. Vadgama, "Physical characterisation of a polycaprolactone tissue scaffold," *Surf. Chem. Biomed. Environ. Sci.*, pp. 215–228, 2006.

[50] E. Eisenbarth, "Biomaterials for tissue engineering," *Adv. Eng. Mater.*, vol. 9, no. 12, pp. 1051–1060, 2007.

[51] W. J. Li and R. S. Tuan, "Fabrication and application of nanofibrous scaffolds in tissue engineering," *Curr. Protoc. Cell Biol.*, no. SUPPL. 42, pp. 1–12, 2009.

[52] H. Li, Y. S. Wong, F. Wen, K. W. Ng, G. K. L. Ng, S. S. Venkatraman, F. Y. C. Boey, and L. P. Tan, "Human Mesenchymal Stem-Cell Behaviour On Direct Laser Micropatterned Electrospun Scaffolds with Hierarchical Structures," *Macromol. Biosci.*, vol. 13, no. 3, pp.

299–310, 2013.

[53] M. Truscott, G. J. Booysen, and D. J. De Beer, “Rapid prototyping and manufacturing in medical product development,” vol. 21, no. 1, pp. 1573–1575, 2009.

[54] G. Chen, T. Ushida, and T. Tateishi, “Scaffold Design for Tissue Engineering,” *Macromol. Biosci.*, vol. 2, pp. 67–77, 2002.

[55] J. T. Rimell and P. M. Marquis, “Selective laser sintering of ultra high molecular weight polyethylene for clinical applications,” *J. Biomed. Mater. Res.*, vol. 53, no. 4, pp. 414–420, 2000.

[56] I. Gibson, M. M. Savalani, C. X. Lam, R. Olkowski, A. K. Ekaputra, K. C. Tan, and D. W. Hutmacher, “Towards a Medium/High Load-Bearing Scaffold Fabrication System,” *Tsinghua Sci. Technol.*, vol. 14, no. SUPPL. 1, pp. 13–19, 2009.

[57] A. K. Sood, R. K. Ohdar, and S. S. Mahapatra, “Parametric appraisal of mechanical property of fused deposition modelling processed parts,” *Mater. Des.*, vol. 31, no. 1, pp. 287–295, 2010.

[58] I. Zein, D. W. Hutmacher, K. C. Tan, and S. H. Teoh, “Fused deposition modeling of novel scaffold architectures for tissue engineering applications,” *Biomaterials*, vol. 23, no. 4, pp. 1169–1185, 2002.

[59] J. H. Lee, S. A. Park, K. E. Park, J. H. Kim, K. S. Kim, J. Lee, and W. D. Kim, “Fabrication and characterization of 3D scaffold using 3D plotting system,” *Chinese Sci. Bull.*, vol. 55, no. 1, pp. 94–98, 2010.

[60] R. Anitha, S. Arunachalam, and P. Radhakrishnan, “Critical parameters influencing the quality of prototypes in fused deposition modelling,” *J. Mater. Process. Technol.*, vol. 118, no. 1–3, pp. 385–388, 2001.

[61] A. K. Aiyangar, J. Vivanco, A. G. Au, P. A. Anderson, E. L. Smith, and H. L. Ploeg, “Dependence of anisotropy of human lumbar vertebral trabecular bone on quantitative computed tomography-based apparent density,” *J. Biomech. Eng.*, vol. 136, no. 9, 2014.

[62] D. W. Hutmacher, T. Schantz, I. Zein, K. W. Ng, S. H. Teoh, and K. C. Tan, “Mechanical properties and cell cultural response of polycaprolactone scaffolds designed and fabricated via fused deposition modeling,” *J. Biomed. Mater. Res.*, vol. 55, no. 2, pp. 203–216, 2001.

[63] J. Z. Liang, “Characteristics of melt shear viscosity during extrusion of polymers,” *Polym. Test.*, vol. 21, no. 3, pp. 307–311, 2002.

[64] M. E. Hoque, Y. L. Chuan, and I. Pashby, “Extrusion based rapid prototyping technique: An advanced platform for tissue engineering scaffold fabrication,” *Biopolymers*, vol. 97, no. 2, pp. 83–93, 2012.

[65] G. Li, L. Wang, W. Pan, F. Yang, W. Jiang, X. Wu, X. Kong, K. Dai, and Y. Hao, “In vitro and in vivo study of additive manufactured porous Ti6Al4V scaffolds for repairing bone defects,” *Sci. Reports 2016 61*, vol. 6, no. 1, pp. 1–11, Sep. 2016.

[66] D. H. S. Ramkumar and M. Bhattacharya, “Steady shear and dynamic properties of biodegradable polyesters,” *Polym. Eng. Sci.*, vol. 38, no. 9, pp. 1426–1435, 1998.

[67] J. Bejarano, P. Caviedes, and H. Palza, “Sol-gel synthesis and in vitro bioactivity of copper and zinc-doped silicate bioactive glasses and glass-ceramics,” *Biomed. Mater.*, vol. 10, no. 2, p. 25001, 2015.

[68] EnvisionTEC, “Instruction Manual for the 3D-Bioplotter.” 2020.

[69] R. V. Baier, J. I. Contreras Raggio, C. M. Giovanetti, H. Palza, I. Burda, G. Terrasi, B. Weisse, G. S. De Freitas, G. Nyström, J. F. Vivanco, and A. K. Aiyangar, “Shape fidelity, mechanical and biological performance of 3D printed polycaprolactone-bioactive glass composite scaffolds,” *Mater. Sci. Eng. C*, no. November, p. 112540, 2021.

[70] ASTM D695, “ASTM D695 − 15: Standard Test Method for Compressive Properties of Rigid Plastics 1 Standard Test Method for Compressive Properties of Rigid Plastics,” *Am. Soc. Test. Mater.*, no. July, pp. 19428–2959, 2015.

[71] S. Gerdes, A. Mostafavi, S. Ramesh, A. Memic, I. V. Rivero, P. Rao, and A. Tamayol, “Process-Structure-Quality Relationships of Three-Dimensional Printed Poly(Caprolactone)-Hydroxyapatite Scaffolds,” *Tissue Eng. - Part A*, vol. 26, no. 5–6, pp. 279–291, 2020.

[72] M. S. Alsoufi and A. E. Elsayed, “Warping deformation of desktop 3D printed parts manufactured by open source fused deposition modeling (FDM) system,” *Int. J. Mech. Mechatronics Eng.*, vol. 17, no. 4, pp. 7–16, 2017.

[73] S. T. Ho and D. W. Hutmacher, “A comparison of micro CT with other techniques used in the characterization of scaffolds,” *Biomaterials*, vol. 27, no. 8, pp. 1362–1376, 2006.

[74] M. Ashby, H. Shercliff, and D. Cebon, *Materials: engineering, science, processing and design*, vol. 13, no. 3. 2010.

[75] K. M. Fawzy El-Sayed and C. E. Dörfer, “Gingival Mesenchymal Stem/Progenitor Cells: A Unique Tissue Engineering Gem,” *Stem Cells Int.*, vol. 2016, pp. 1–16, 2016.

[76] C. Millan, J. F. Vivanco, I. M. Benjumeda-Wijnhoven, S. Bjelica, and J. F. Santibanez, “Mesenchymal Stem Cells and Calcium Phosphate Bioceramics: Implications in Periodontal Bone Regeneration,” in *Cell Biology and Translational Medicine, Volume 3*, Cham: Springer International Publishing, 2018, pp. 91–112.

[77] Z. T. Birgani, C. A. van Blitterswijk, and P. Habibovic, “Monolithic calcium

phosphate/poly(Lactic acid) composite versus calcium phosphate-coated poly(lactic acid) for support of osteogenic differentiation of human mesenchymal stromal cells," *J. Mater. Sci. Mater. Med.*, vol. 27, no. 3, pp. 1–12, 2016.

[78] C. Brown, C. McKee, S. Bakshi, K. Walker, E. Hakman, S. Halassy, D. Svinarich, R. Dodds, C. K. Govind, and G. R. Chaudhry, "Mesenchymal stem cells: Cell therapy and regeneration potential," *J. Tissue Eng. Regen. Med.*, vol. 13, no. 9, pp. 1738–1755, 2019.

[79] I. Benjumeda Wijnhoven, R. Vallejos, J. F. Santibanez, C. Millán, and J. F. Vivanco, "Analysis of cell-biomaterial interaction through cellular bridge formation in the interface between hGMSCs and CaP bioceramics," *Sci. Rep.*, vol. 10, no. 1, p. 16493, Dec. 2020.

[80] R. Vallejos Baier, J. Contreras, C. Toro, M. Bustamante, L. Pérez, I. Burda, A. Aiyangar, and J. F. Vivanco, "Structure-function assessment of 3D-printed porous scaffolds by a low-cost/open source fused filament fabrication printer," *Mater. Sci. Eng. C*, vol. 184, no. August, p. 111945, 2021.

[81] B. N. Teixeira, P. Aprile, R. H. Mendonça, D. J. Kelly, and R. M. da S. M. Thiré, "Evaluation of bone marrow stem cell response to PLA scaffolds manufactured by 3D printing and coated with polydopamine and type I collagen," *J. Biomed. Mater. Res. - Part B Appl. Biomater.*, vol. 107, no. 1, pp. 37–49, 2018.

[82] I. Izal, P. Aranda, P. Sanz-Ramos, P. Ripalda, G. Mora, F. Granero-Moltó, H. Deplaine, J. L. Gómez-Ribelles, G. G. Ferrer, V. Acosta, I. Ochoa, J. M. García-Aznar, E. J. Andreu, M. Monleón-Pradas, M. Doblaré, and F. Prósper, "Culture of human bone marrow-derived mesenchymal stem cells on of poly(l-lactic acid) scaffolds: potential application for the tissue engineering of cartilage," *Knee Surgery, Sport. Traumatol. Arthrosc.*, vol. 21, no. 8, pp. 1737–1750, Aug. 2013.

[83] T. Serra, J. A. Planell, and M. Navarro, "High-resolution PLA-based composite scaffolds via 3-D printing technology," *Acta Biomater.*, vol. 9, no. 3, pp. 5521–5530, 2013.

[84] Y. S. Cho, S. Choi, S. H. Lee, K. K. Kim, and Y. S. Cho, "Assessments of polycaprolactone/hydroxyapatite composite scaffold with enhanced biomimetic mineralization by exposure to hydroxyapatite via a 3D-printing system and alkaline erosion," *Eur. Polym. J.*, vol. 113, no. May 2018, pp. 340–348, 2019.

[85] D. Liepsch, "A Basic Introduction to Rheology Shear Flow," *J Biomech*, vol. 35, no. 4, pp. 415–435, 2016.

[86] A. Houel, "User Manual Instructions Physica MCR501 Anton Paar," 2006.

[87] A. S. Gladman, D. Kokkinis, A. Neels, P. Tingaut, T. Zimmermann, J. A. Lewis, M. K. Hausmann, R. Libanori, A. R. Studart, and G. Siqueira, "Cellulose Nanocrystal Inks for

3D Printing of Textured Cellular Architectures," *Adv. Funct. Mater.*, vol. 27, no. 12, p. 1604619, 2017.

[88] M. K. Hausmann, P. A. Rühs, G. Siqueira, J. Läuger, R. Libanori, T. Zimmermann, and A. R. Studart, "Dynamics of Cellulose Nanocrystal Alignment during 3D Printing," *ACS Nano*, vol. 12, no. 7, pp. 6926–6937, 2018.

[89] M. Sarker and X. B. Chen, "Modeling the Flow Behavior and Flow Rate of Medium Viscosity Alginate for Scaffold Fabrication With a Three-Dimensional Bioplotter," *J. Manuf. Sci. Eng. Trans. ASME*, vol. 139, no. 8, 2017.

[90] J. A. Lewis, "Direct ink writing of 3D functional materials," *Adv. Funct. Mater.*, vol. 16, no. 17, pp. 2193–2204, 2006.

[91] A. Nommeots-Nomm, P. D. Lee, and J. R. Jones, "Direct ink writing of highly bioactive glasses," *J. Eur. Ceram. Soc.*, vol. 38, no. 3, pp. 837–844, Mar. 2018.

[92] P. Sheshadri and R. A. Shirwaiker, "Characterization of Material–Process–Structure Interactions in the 3D Bioplotting of Polycaprolactone," *3D Print. Addit. Manuf.*, vol. 2, no. 1, pp. 20–31, Mar. 2015.

[93] S. Borhan, S. Hesaraki, A.-A. Behnamghader, and E. Ghasemi, "Rheological evaluations and in vitro studies of injectable bioactive glass–polycaprolactone–sodium alginate composites," *J. Mater. Sci. Mater. Med.*, vol. 27, no. 9, p. 137, Sep. 2016.

[94] S. Gerdes, A. Mostafavi, S. Ramesh, A. Memic, I. V. Rivero, P. Rao, and A. Tamayol, "Process-Structure-Quality Relationships of Three-Dimensional Printed Poly(Caprolactone)-Hydroxyapatite Scaffolds," *Tissue Eng. - Part A*, vol. 26, no. 5–6, pp. 279–291, 2020.

[95] N. C. Paxton, J. Ren, M. J. Ainsworth, A. K. Solanki, J. R. Jones, M. C. Allenby, M. M. Stevens, and M. A. Woodruff, "Rheological Characterization of Biomaterials Directs Additive Manufacturing of Strontium-Substituted Bioactive Glass/Polycaprolactone Microfibers," *Macromol. Rapid Commun.*, vol. 40, no. 11, pp. 1–6, 2019.

[96] A. Schwab, R. Levato, M. D'Este, S. Piluso, D. Eglin, and J. Malda, "Printability and Shape Fidelity of Bioinks in 3D Bioprinting," *Chem. Rev.*, vol. 120, no. 19, pp. 11028–11055, 2020.

ANNEXED

-MicroCT Videos

-Timelapses videos

-Papers